The mid-Cretaceous greenhouse climate and marine stable oxygen isotope: insights from general circulation model experiments

by

Jing Zhou

A dissertation submitted in partial fulfillment
of the requirements for the degree of
Doctor of Philosophy
(Earth and Environmental Sciences)
in The University of Michigan
2012

Doctoral Committee:

Associate Professor Christopher J. Poulsen, Chair
Professor Mary Anne Carroll
Professor Kyger C. Lohmann
Associate Professor Ingrid L. Hendy
Assistant Professor Nathan D. Sheldon

To my family and friends

Acknowledgements

First and foremost, I am grateful to my thesis advisor, Dr. Christopher J. Poulsen. I appreciate all his contributions of time and ideas to promote my professional and personal development. The enthusiasm and patience he has for enlightening and encouraging students was motivational for me. I feel so lucky to be his student.

I would like to thank my thesis committee, including Drs. Mary Anne Carroll, Ingrid Hendy, Kyger C. Lohmann and Nathan D. Sheldon, for their time, suggestion, questions and criticisms. I am also thankful to Ingrid for her advice as a woman scientist. I thank my collaborators including Drs. Christine Shields, Nan Rosenbloom, Bruce Briegleb, David Pollard and Tim White for suggestion and discussions. Thanks to Christine and David also for their help in setting up numerical simulations and post-processing model output. I acknowledge Michael Messina for his instrumental support in Unix Systems and Janine Taylor for her support in Window systems.

The members of Dr. Poulsen's group have contributed immensely to my time at Michigan. The group is a source of support, friendships and fun. I especially thank Shih-yu Lee for her kind advice both personally and professionally. Special thanks also to Daniel Horton for accompanying me in the whole Ph.D. journey.

I gratefully acknowledge the financial support that made this thesis possible. I was funded by a National Science Foundation grant (0433440 and 0310032) to Drs. C.J. Poulsen, D. Pollard, and T. White, a Barbour Scholarship and a One-Term Dissertation

Fellowship from the Rackham Graduate School of University of Michigan and a Turner Grant from my department.

Lastly, I would like to thank my family for their love, encouragement and support. To my boyfriend, Yang Chen, I am indebted to him for his infinite love, patience and friendship.

Table of Contents

Dedication…….....ii
Acknowledgements…...……iii
List of Figures……vii
List of Tables……...xi
Abstract……...…….....xii
Chapter
I Introduction……...…….……...1
1.1 Mid-Cretaceous greenhouse climate inferred by proxies ……....4
1.1.1 Terrestrial evidence for mid-Cretaceous polar warmth……...4
1.1.2 Marine stable oxygen isotope evidence for mid-Cretaceous warmth…….5
1.1.3 Marine stable oxygen isotope evidence for mid-Cretaceous short-term glaciation……7
1.2 Proposed mechanisms for mid-Cretaceous climate change……...7
1.2.1 The greenhouse climate with extreme polar warmth…….7
1.2.2 The mid-Cretaceous thermal maximum and short-term glaciations...9
1.3 Outline of this dissertation…….……..10
II Vegetation-climate interactions in the warm mid-Cretaceous…….……..13
Abstract…….……13
2.1 Introduction…….…….……14
2.2 Methods…….…….……..16
2.3 Results…….…….……21
2.3.1 Response of vegetation to atmospheric pCO_2…….……..21
2.3.2 Impact of vegetation and atmospheric pCO_2 on mid-Cretaceous climate……28
2.4 Discussion…….……...……43
2.4.1 The role of vegetation feedbacks under high CO_2.....43
2.4.2 Oceanic circulation…….……..46
2.5 Caveats…….……46
2.6 Conclusions……..……47
III Abrupt Arctic warming in a greenhouse climate…….……49
Abstract…….…….……49
3.1 Introduction……..……50
3.2 Methods……..……..……51
3.3 Results…….…….……53
3.3.1 Simulation of mean climate…….……53
3.3.2 Abrupt warming in the 10xDGVM experiment……..……..56
3.4 Discussion……62

IV Simulation of modern and middle Cretaceous marine $\delta^{18}O$ with an ocean-atmosphere GCM……..……...……..66
Abstract……..……66
4.1 Introduction……..……67
4.2 Methods……69
4.3 Results……..……74
4.3.1 Simulation of modern $\delta^{18}O$……..74
4.3.2 Simulation of Cretaceous climate and precipitation $\delta^{18}O_p$……..80
4.3.3 Simulation of Cretaceous surface seawater $\delta^{18}O_w$……..….84
4.3.4 Simulation of Cretaceous subsurface seawater $\delta^{18}O_w$…….87
4.4 Discussion……90
4.4.1 Simulation of Cretaceous surface seawater $\delta^{18}O_w$……..……..90
4.4.2 Implications for oxygen isotope paleo-thermometry……92
4.4.3 Oceanic gateways, continental runoff, and seawater $\delta^{18}O_w$……..96
4.5 Conclusions…….……..…98
V No climate extremes in the mid-Cretaceous……..99
Abstract……..……99
5.1 Introduction……100
5.2 Methods……..……102
5.3 Results……108
5.3.1 Response of seawater temperatures and $\delta^{18}O_{sw}$……..108
5.3.2 Response of the Atlantic carbonate $\delta^{18}O_c$…..……..111
5.4 Discussion……..……114
5.5 Conclusions……118
VI Conclusion……..……120
6.1 Results summary……120
6.2 Contribution and implication……..……...123
6.3 Limitation…...……124
6.4 Recommendations for future research……...……125
References……129

List of Figures

Figure

1-1 Zonal-average annual mean 2m air temperature (ºC) (a); and precipitation (mm day^{-1}) (b) for the modern observation (black), CCSM3 modern experiment (green), and GENMOM modern experiment (red), respectively. ……..……..3

1-2 Proxy-inferred mid-Cretaceous surface temperatures. Grey shading denotes continent and light blue shading denotes ocean. Continental surface temperatures (black dots over gray shading) are estimated from paleo- faunal and floral evidence, and sea-surface temperatures are inferred by marine carbonate oxygen isotope (black dots over light blue shading), TEX_{86} (red dots) and Ma/Ca ratio (green dots) ……...…6

2-1 Zonal-average annual mean continental surface temperature (ºC) (a); and precipitation (mm day^{-1}) (b) for the 1xDGVM (black dash-dot line), 10xBG (black dashed line), 10xDGVM (black solid line) and 16xDGVM (black dotted line) experiments,respectively……
……23

2-2 Global distribution of evergreen trees (a), (d), (g), deciduous trees (b), (e), (h) and grasses (c), (f), (i) (%) for the 1xDGVM, 10xDGVM, and 16xDGVM experiments, respectively..……...….. 25

2-3 Distribution of mid-Cretaceous vegetation inferred from fossil wood, pollen of Elaterate assemblages and coal deposits and comparison with simulated vegetation…...27

2-4 Mean annual surface temperature (ºC) for the 10xDGVM experiment (a); 10xDGVM – 10xBG experiments (b); and 16xDGVM - 10xDGVM experiments (c)..……..……29

2-5 Annual cycles of surface temperature (ºC), latent heat fluxes (W m^{-2}), surface absorbed solar radiation (W m^{-2}), surface reflected solar radiation (W m^{-2}), surface shortwave cloud forcing (W m^{-2}) over the high-latitude forests (a-e), low-latitude forests (f-j) and mid-latitude forests (k-o) for 10xDGVM – 10xBG experiments. ……..30

2-6 Annual mean a) total evapotranspiration over land (mm day^{-1}); b) surface albedo (%); and c) low cloud cover (%) for the 10xDGVM – 10xBG experiments (%)……..32

2-7 Difference between the 16xDGVM and 10xDGVM experiments for the annual mean surface albedo (%) (a); and low cloud cover (%) (b)……..……...36

2-8 Mean annual precipitation (mm day^{-1}) for the 10xDGVM (a); 10xDGVM – 10xBG experiments (b); and 16xDGVM - 10xDGVM experiments (c)…….…...……38

2-9 Zonal-average annual mean meridional streamfunction (10^{10} kg s^{-1}) at 400 mb (a); and wind stress (N m^{-2}) over the Pacific Ocean (b) for the 10xDGVM (black solid line) , 10xBG (grey dashed line) and 10xDGVM – 10xBG experiments (black dashed line), respectively……..……..39

2-10 Annual mean Meridional overturning circulation (Sv) for a) 10xDGVM experiment; and b) 10xBG experiment. ……..……..42

2-11 Model-data comparison for mid-Cretaceous surface temperature….……45

3-1 Map view of mean annual a) surface temperature (color) and sea-ice fraction (dashed contour lines; 10, 40, and 90%) for the 1xDGVM experiment; b) surface temperature (color) and sea ice fraction (dashed contour lines; 10%) for the 10xDGVM experiment, averaged over years 700-750 (before the abrupt Arctic warming); c) surface temperature anomaly between years 900-950 (after the abrupt Arctic warming) and years 700-750...54

3-2 Mean annual global MOC for a) the 1xDGVM experiment; b) the 10xDGVM experiment, averaged over years 700-750; c) the 10xDGVM experiment, averaged over years 1550-1600. ……..55

3-3 Time series for the 10x experiment of a) Arctic (70-90 °N) surface temperature (°C, red) and mid-latitude surface temperature (°C, blue); b) salinity of the North Pacific (psu, red), and oceanic heat transport at 70 °N (PW, blue); c) Arctic (70-90 °N) low-cloud fraction (red), and cloud radiative forcing (Wm^{-2}, blue); d) maximum Northern Hemisphere MOC intensity below 500 m (Sv, red), and oceanic heat transport across 44 °N (PW, blue).……..…..57

3-4 a) Mean annual barotropic stream function (Sv) in the 10x experiment a) averaged over model years 700-750; b) difference (Sv) between model years 900-950 and years 700-750. Positive (negative) values indicate anticyclonic (cyclonic) flow……...59

3-5 Mean annual North Pacific mixed-layer depth in the 10x experiment a) averaged over model years 700-750; b) averaged over model years 900-950……..61

3-6 Detrended time series of 1xDGVM experiment a) Arctic (70-90 °N) surface temperature anomalies (red), and sea ice area anomalies (blue); b) Arctic surface temperature anomalies between years 1580 and 1660……...64

4-1 Mean annual zonal average $\delta^{18}O_p$ (SMOW) of precipitation predicted in our MOD experiment and from IAEA/WMO data (Rozanski et al., 1993)……...…76

4-2 Mean annual $\delta^{18}O_w$ (SMOW) spatial distribution of modern surface seawater predicted in our MOD experiment (a), and interpolated from global gridded empirical

data (LeGrande and Schmidt, 2006) (b).……..……..78

4-3 Mean annual zonal average $\delta^{18}O_w$ (SMOW) of modern surface seawater (A); and modern deep water at 3000 m (B) predicted in our MOD (medium dashed line) and MOD-Bering (short dashed line) experiments and from LeGrande and Schmidt (2006) (solid line). ……....79

4-4 Mean annual zonal average sea-surface temperature in MOD (solid line), K-Flat (medium dashed line) and K-Bathy (short dashed line) experiments. ……..81

4-5 Mean annual zonal average precipitation $\delta^{18}O_p$ (SMOW) in MOD (solid line), K-Flat (medium dashed line) and K-Bathy (short dashed line) experiments. Note that "corrected" Cretaceous $\delta^{18}O$ is shown. ……..……..83

4-6 Mean annual $\delta^{18}O_w$ (SMOW) spatial distribution of Cretaceous surface seawater predicted for the K-Flat experiment (a), and K-Bathy experiment (b). Continental regions are shaded in grey. ……..……..85

4-7 Mean annual zonal average $\delta^{18}O_w$ (SMOW) of surface seawater in MOD (solid line), MOD-Bering (medium dashed line), K-Flat (short dashed line) and K-Bathy (dash-dot line) experiments. ……..86

4-8 Vertical distribution of global mean seawater $\delta^{18}O_w$ (SMOW) in the modern and Cretaceous simulations. ……..……..88

4-9 Mean annual $\delta^{18}O_w$ (SMOW) spatial distribution of Cretaceous seawater in K-Flat experiment at depth of 778 m (A); at depth of 2796 m (B); and at depth of 5268 m (C). 89

4-10 Comparison of temperature estimates using different assumptions about Cretaceous seawater $\delta^{18}O_w$. ……...……..94

4-11 Mean-annual $\delta^{18}O_w$ (SMOW) difference between local and zonal average surface seawater. For each grid cell, the $\delta^{18}O_w$ difference is obtained by subtracting the zonal average $\delta^{18}O_w$ at that latitude from the local $\delta^{18}O_w$……..……..95

5-1 Paleogeography for the 8x experiment (a), and Paleogeography for the HiStand experiment (b).……...……..104

5-2 The changes of salinity fluxes converted from freshwater forcing (precipitation + runoff - evaporation) into the North Atlantic in the SaltNNA – 8x experiments (a); SaltTNA – 8x experiments (b); SaltNCS – SmallCS experiments (c); and SaltTCS - SmallCS experiments (d). ……..……..107

5-3 Mean-annual zonal average sea-surface temperature (SST) (°C) (a), surface seawater $\delta^{18}O_{sw}$ (‰) (b), bathyal seawater temperatures (at 1059 m) (°C) (c) for the 8x, 16x, HiStand, CloseCS and SmallCS GENMOM experiments, and bathyal seawater

temperatures (at 1059 m) (°C) for the SaltNNA, FreshNNA, SaltTNA, SaltNCS and SaltTCS MOM2 experiments (d). ……..……..109

5-4 Mean-annual, zonal-average carbonate $\delta^{18}O_c$ (‰ in PDB) in North and South Atlantic Oceans for the 16x – 8x experiments (a), HiStand – 8x experiments (b), OpenSA – 8x experiments (c), SmallCS – 8x experiments (d), CloseCS – 8x experiments (e), SaltNNA – FreshNNA experiments (f), SaltTNA– 8x experiments (g), and SaltTCS – SmallCS experiments (h). ……..……...……..113

List of Tables

Table

2-1 Bioclimatic parameters for survival and establishment of plant functional type (PFT)……..18

2-2 Mid-Cretaceous CCSM3 experiments and global annual mean surface temperature (SAT) and precipitation……..…….…….……..20

2-3 Global and high-latitude annual mean climatic variables in the 10xBG and 10x DGVM experiments……..33

4-1 Model parameters and global average sea-surface temperature (ºC), precipitation (mm day^{-1}), $\delta^{18}O$ of surface seawater and precipitation (‰) (SMOW)……..…….....73

5-1 List of experiments, simulated global-average seawater temperatures and $\delta^{18}O$ (T_{gl}, °C), North Atlantic Ocean seawater temperature and $\delta^{18}O$ (T_{NA}, °C; δ_{NA}, ‰), and mass flux of the North Atlantic meridional overturning circulation (NAMOC, Sv)……106

5-2. Variations in observed carbonate $\delta^{18}O_c$ (Obv.$\Delta\delta^{18}O_c$) and paleo-latitudes of the sampling locations between Albian and Turonian, and adjusted $\Delta\delta^{18}O_c$ after removing the changes induced by equatorward drift of the sampling sites (Lat-adjust $\Delta\delta^{18}O_c$), and model-estimated $\Delta\delta^{18}O_c$ due to the closure of Caribbean Seaway (CloseCS $\Delta\delta^{18}O_c$)..……..……..115

Abstract

The mid-Cretaceous (~112-89 Ma) was the warmest period in the past 144 my. The relatively abundant terrestrial and marine geological records provide a great opportunity to explore the interactions among ocean, atmosphere, cryosphere and biosphere in a greenhouse climate. Previous climate models have not been successfully reproduced the mid-Cretaceous low meridional thermal gradient and extreme polar warmth as inferred by various proxies. In addition to this model-data discrepancy, the gradual warming through this interval and periodic glaciations as suggested by marine carbonate $\delta^{18}O_c$ are at odds with the coeval decreasing yet high atmospheric pCO_2. This proxy-proxy inconsistence questions the driving role of atmospheric pCO_2 on climate change. These paradoxes imply either our current understanding of greenhouse climate physics or our interpretations of proxy data are flawed. This dissertation integrates numerical climate models and geological proxy records to better constrain the mid-Cretaceous climate change.

Using state-of-the art general circulation models (GCMs), this dissertation investigates 1) mechanisms and consequences of mid-Cretaceous greenhouse climate; and 2) uncertainties of the marine carbonate $\delta^{18}O_c$ interpretation. More specifically, Part I of this dissertation explores the effects of vegetation and high atmospheric pCO_2 on mid-Cretaceous climate using a fully coupled ocean-atmosphere GCM with dynamic global vegetation (CCSM3) (Chapter II and III). Chapter II focuses on the final equilibrium

effects of vegetation and atmospheric pCO_2. This chapter demonstrates that equilibrium mean temperatures, hydrological cycle, atmospheric and oceanic circulations are sensitive to the presence of vegetation and enhanced atmospheric pCO_2. While both vegetation and high atmospheric pCO_2 lead to a substantial warming and reduced meridional thermal gradient, they cannot sustain an Arctic climate as warm as the proxy estimates. Therefore, we suggest that other mechanisms in addition to high atmospheric pCO_2 and vegetation are required to explain the mid-Cretaceous polar warmth. Chapter III analyzes variability of the simulated mid-Cretaceous climate with different pCO_2 levels. We find that Arctic climate variability also changes substantially with increasing atmospheric pCO_2. The intrinsic Arctic variability with 10x pCO_2 leads to an additional warming of ~1.5 °C in the Arctic zone and an intensification of the northern hemisphere meridional overturning circulation by ~50%.

Part II of this dissertation employs a water isotope-enabled ocean-atmosphere GCM (GENMOM) to determine the responses of seawater $\delta^{18}O_{sw}$ and marine carbonate $\delta^{18}O_c$ to paleogeography, atmospheric pCO_2, sea level and freshwater forcing (Chapter IV and V). In Chapter IV, we mainly explore how the distribution of mid-Cretaceous seawater $\delta^{18}O_{sw}$ differs from modern. We find that mid-Cretaceous surface seawater $\delta^{18}O_{sw}$ is depleted by 1.3‰ SMOW at low-to-mid latitudes and up to 2.0‰ SMOW at high latitudes in comparison to modern values. Thus, oxygen isotopic paleothermometry using global mean seawater $\delta^{18}O_{sw}$ or a modern latitudinal distribution might overestimate Cretaceous sea-surface temperatures, especially at mid-to-high latitudes. As a result, the mid-Cretaceous equator-to-pole marine thermal gradient was likely much higher than that reported in previous studies, reconciling the model-data discrepancy.

Based on the findings of Chapter IV, Chapter V examines whether the short- and long-term changes in marine carbonate $\delta^{18}O_c$ through the mid-Cretaceous interval signal global events. Model results suggest that the variations of carbonate $\delta^{18}O_c$ preserved in the mid-Cretaceous marine record reflect regional oceanographic rather than global climate changes. We conclude that the mid-Cretaceous was neither a thermal maximum nor an ice age.

Chapter I

Introduction

The mid-Cretaceous (~112-89 Ma) was the warmest period in the past 144 my. Geological evidence suggests that mid-Cretaceous was about 6-14 °C warmer than modern (Barron, 1983) and the warming was mainly attributed to the high atmospheric pCO2 (Barron and Washington, 1985). Therefore, the mid-Cretaceous has long been considered as a good analogue to the future greenhouse climate induced by the anthropogenic emission of CO2. However, general circulation models (GCMs) have difficulty in reproducing key aspects of the proxy-inferred mid-Cretaceous climate. One problem directly relevant to future prediction is that GCMs are unable to simulate the mid-Cretaceous polar warmth and the corresponding low equator-to-pole temperature gradient as inferred by proxies. The implication of this model-proxy data discrepancy is threefold.

First, the discrepancy between the models and geological data may be due to flaws in climate models stemming from model parameterization. Following this possibility, the reliability of model prediction of future greenhouse climate is questionable. Second, the discrepancy may be caused by uncertainties in mid-Cretaceous boundary conditions (e.g., atmospheric pCO_2, pCH_4, paleogeography) that are required to model the past climate. Third, it is also possible that the interpretation of geological data

is biased by the underlying assumptions. For instance, oxygen isotope paleothermometry requires knowledge of the ambient seawater oxygen isotope concentration ($\delta^{18}O_{sw}$). Because there are no independent proxies of $\delta^{18}O_{sw}$, this value is often assumed to be globally uniform or to have a distribution similar to modern. However, it is not clear that whether these assumptions are justified. In practice, 1‰ offset in seawater $\delta^{18}O_{sw}$ could bias oxygen isotopic paleotemperature by ~4 °C. Recent studies also suggest that uncertainty in paleo-terrestrial temperatures derived from on modern correlations between leaf physiogonomic traits and temperatures may much larger than previously recognized (Little et al., 2010; Peppe et al., 2010, 2011).

This thesis tests the latter two possibilities using state-of-the art coupled ocean-atmosphere GCMs. Specifically, CCSM3 implemented with dynamic global vegetation model is employed to investigate the effects of boundary conditions. GENMOM with water isotope-tracking capability is used to explore the responses of marine seawater and carbonate $\delta^{18}O$ to global and regional forcing and thus provides constrains on the interpretation of marine oxygen isotopes. Both models successfully simulate modern surface temperatures (Fig. 1-1a) and precipitation rates beyond Intertropical Convergence Zone (Fig. 1-1b).

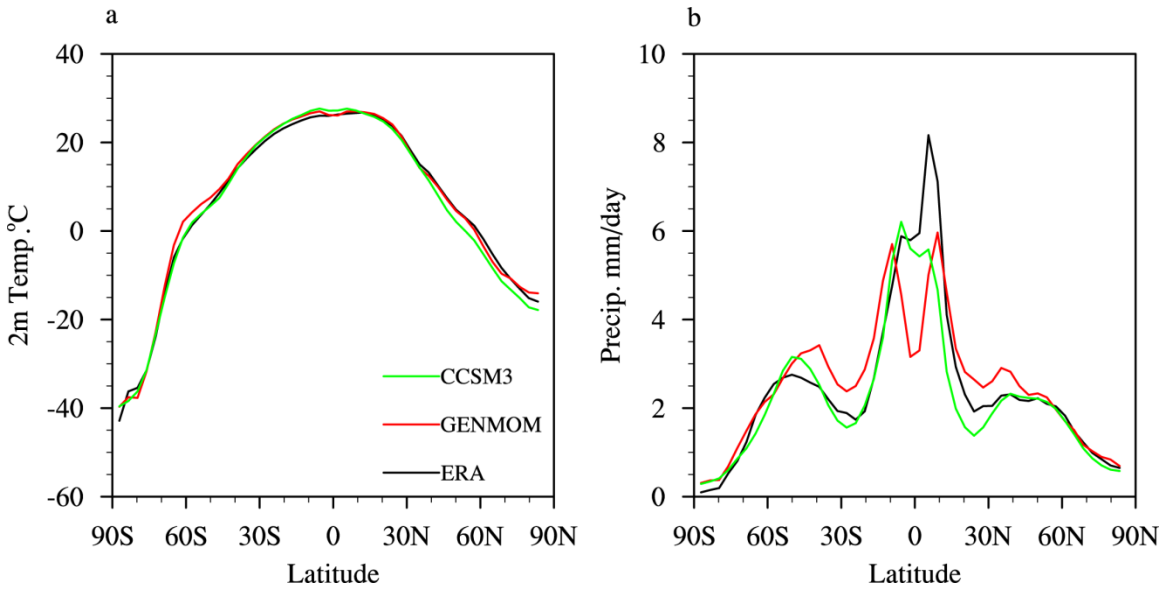

Figure 1-1. Zonal−average annual mean 2m air temperature (ºC) (a); and precipitation (mm day^{-1}) (b) for the modern observation (black), CCSM3 modern experiment (green), and GENMOM modern experiment (red), respectively.

1.1. Mid-Cretaceous greenhouse climate inferred by proxies

The mid-Cretaceous extreme warmth is supported by sedimentological evidence of ice-free polar regions, paleo-floral and faunal evidence of tropical species at high latitudes, leaf-margin analyses of fossil leaves, marine records of oxygen isotope paleothermometry, TEX_{86} and Ma/Ca ratio (Fig. 1-2, see below for references). To clarify, this dissertation is mainly interested in model-data comparison for paleotemperatures. Therefore, while there are proxies for other climatic fields (e.g. soil moisture, precipitation, pCO_2 etc), these are not the focus of this dissertation, largely because these proxies are not as well understood and established. A model-data comparison of mid-Cretaceous terrestrial paleosol $\delta^{18}O$ was previously reported by Poulsen et al. (2007).

1.1.1. Terrestrial evidence for mid-Cretaceous polar warmth

The mid-Cretaceous high-latitude climate was suggested to be warm and balmy. The discovery of vertebrate assemblage from the Canadian Arctic during Turonian-Coniacian suggests that the Arctic climates were much warmer than near freezing. Based on their living relatives (the crocodiles), it further indicates that the coldest monthly temperature was above 5 °C and mean annual temperature exceeded 14 °C (Tarduno et al., 1998). Fossil leaves and fruit of tropical breadfruit tree that survive between ~15-38 °C from western Greenland Cenomanian sediments further support the view of a warm Arctic (Nathorst, 1890). Similarly, the occurrence of tropical flora *Hausmannia* in the Albian Alexander Island suggests that the Antarctic mean annual temperatures was in the range 13-27 °C (Cantrill, 1995). The more quantitative leaf-margin analysis of fossil leaves suggests a slightly cooler polar climate. This quantitative analysis indicates that mean annual temperatures in the Arctic and Antarctica regions were ~7-13 °C during

mid-Cretaceous (Herman and Spicer, 1996; Parrish and Spicer, 1988; Spicer and Parrish, 1986; Spicer et al., 2002, 2008; Spicer and Corfield, 1992).

1.1.2. Marine stable oxygen isotope evidence for mid-Cretaceous warmth

The oxygen isotope composition of marine carbonate ($\delta^{18}O_c$) is the most direct and widely used proxy for mid-Cretaceous climate. The relatively abundant data provide a great opportunity to investigate the spatial and temporal variations of mid-Cretaceous climate.

Consistent with terrestrial proxies, $\delta^{18}O_c$ of planktonic/benthic foraminifera and bulk carbonate suggest that the southern high latitudes (~60 °S) were warmer than 16 °C and up to 32 °C during Turonian (Bice et al., 2003; Clarke and Jenkyns, 1999; Huber et al., 1995). The subtropical North Atlantic estimates were comparable to modern tropical SSTs (Petrizzo et al., 2008; Voigt et al., 2003, 2004). The oxygen isotopic interpretations of tropical climate have changed substantially during the past 10 years. *Prior to* this century, the oxygen isotopic sea-surface paleotemperatures from the tropical Pacific and proto- North Atlantic were thought to be no greater than modern tropical SSTs (Huber et al., 1995; Price et al., 1998; Sellwood et al., 1994; Woo et al., 1992). Consequently, the low-to-high latitude temperature difference was suggested to be no more than 14 °C (Huber et al., 1995). However, the more recent studies with well-preserved "glassy" foraminifera demonstrate that the tropical North Atlantic were much warmer than modern (Bice et al., 2006; Bornemann et al., 2008; Norris et al., 2002; Wilson et al., 2002). This tropical warmth is also supported by the non-isotope proxies including TEX_{86} and Ma/Ca ratio (Bice et al., 2006; Forster et al., 2007; Schouten et al., 2003). As a result, the low-to-high latitude sea-surface temperature difference increases by 50% (7 °C).

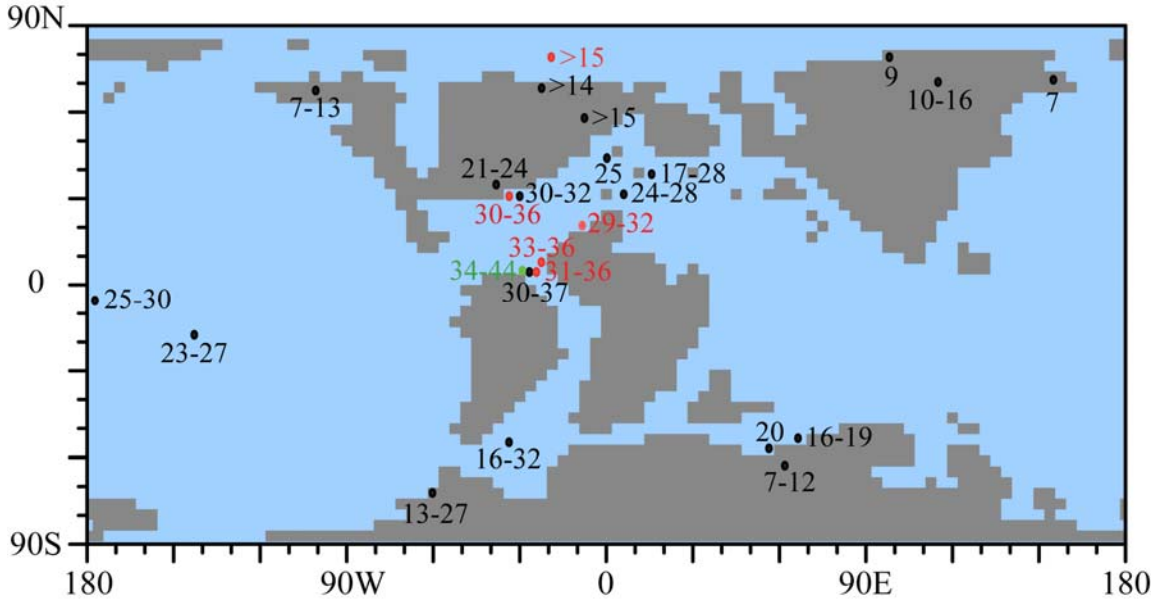

Figure 1-2. Proxy-inferred mid-Cretaceous surface temperatures. Grey shading denotes continent and light blue shading denotes ocean. Continental surface temperatures (black dots over gray shading) are estimated from paleo- faunal and floral evidence, and sea-surface temperatures are inferred by marine carbonate oxygen isotope (black dots over light blue shading), TEX_{86} (red dots) and Ma/Ca ratio (green dots). See text for references.

In addition to the overall warmth, the roughly simultaneous decreases in long-term isotope record from the proto-North Atlantic, European shelf-sea, South Atlantic and Australia suggests that the mid-Cretaceous global warming commenced in the Albian and culminated during the latest Cenomanian-early Turonian (Bice et al., 2003, 2006; Clarke and Jenkyns, 1999; Jenkyns et al., 1994; Huber et al., 1995, 2002; Wilson et al., 2002). The most pronounced warming in the South Atlantic and bathyal subtropical North Atlantic was estimated to be more than 12 °C.

1.1.3. Marine stable oxygen isotope as evidence for mid-Cretaceous short-term glaciation

Despite the estimated extreme polar warmth, short-term (< 1 my) positive excursions in marine carbonate $\delta^{18}O_c$ and their plausible correlation with sequence boundaries have been considered evidence of glaciations during the mid-Cenomanian and mid-Turonian (Bornemann et al., 2008; Galeotti et al., 2009; Miller et al., 2003, 2005; Stoll and Schrag, 2000). Assuming 10 m sea-level fall equivalent to 0.075-0.11‰ $\delta^{18}O_c$ increase, the 0.3-0.7‰ increase in $\delta^{18}O_c$ suggests that the ice volume could be greater than 50% that of the modern Antarctica during the extremely warm mid-Turonian (Bornemann et al., 2008).

1.2. Proposed mechanisms for mid-Cretaceous climate change

1.2.1. The greenhouse climate with extreme polar warmth

Proxy estimates and theoretical calculations suggest that atmospheric pCO_2 was likely above 1000 ppmv and as high as ~5000 ppmv during mid-Cretaceous (Bice and Norris, 2002; Crowley and Berner, 2001). It is widely accepted that the general warmth of mid-Cretaceous was attributed to this high atmospheric pCO_2 (Barron and Washington,

1985). However, simulations of Cretaceous climate using GCMs with high atmospheric CO_2 predict polar temperatures that are too cool to be consistent with reasonable tropical temperatures (Barron et al., 1995; Poulsen et al., 1999, 2004; Spicer et al., 2008). Several possibilities have been proposed to reconcile this model-proxy data mismatch in polar warmth and the corresponding low meridional thermal gradient.

Poulsen et al. (1999) suggest that the assumptions used to interpret oxygen isotopic paleothermometry contribute substantially to the model-data discrepancy. After taking into account the effects of paleo-habitat depth, the oxygen isotopic paleotemperatures are comparable to model simulated values at low latitude. In addition, using adjusted seawater $\delta^{18}O_{sw}$ derived from modern salinity-seawater $\delta^{18}O_{sw}$ relationship and the simulated mid-Cretaceous salinity, the equator-to-polar sea-surface temperature gradient decreases by ~5 °C. Nonetheless, the corrected oxygen isotopic paleotemperatures are still ~ 9 °C warmer than a model prediction with 4x pre-industrial atmospheric pCO_2.

Uncertainties in mid-Cretaceous boundary conditions have also been considered to contribute to the model-data mismatch. Donnadieu et al. (2006) show that the paleogeography evolution from the Early Cretaceous lowstand to mid-to-late Cretaceous highstand induces a warming of ~ 1 °C at low latitudes and > 5 °C at high latitudes in the absence of atmospheric pCO_2 variation. However, the simulation with highstand paleogeography and 4x pre-industrial atmospheric pCO_2 still cannot simulate enough polar warmth. Bice et al. (2006) suggest that high concentration of CH_4 also promoted polar warming.

Climate mechanisms including enhanced poleward heat transport via

strengthening of atmospheric or oceanic circulation (e.g. Covey and Barron, 1988; Farrel, 1990; Korty et al., 2008), increased local radiative forcing through high-latitude cloud feedbacks (e.g. Abbot and Tziperman, 2008; Kump and Pollard, 2008; Sloan and Pollard, 1998), and high-latitude forests (Deconto et al., 2000; Otto-Bliesner and Upchurch, 1997; Upchurch et al., 1998) have also largely reduce the discrepancy.

However, most of these previous studies were conducted with conceptual models or uncoupled ocean/atmosphere GCMs, which neglected realistic ocean-atmosphere interactions. Furthermore, the effects of the atmospheric pCO_2 at the estimated upper limit are less certain.

1.2.2 The mid-Cretaceous thermal maximum and short-term glaciation

Proxy estimates and theoretical calculations suggest that atmospheric pCO_2 decreased from the Aptian-Albian through the Turonian but remained above 1000 ppmv (Bice and Norris, 2002; Larson, 1991; Crowley and Berner, 2001). The high but declining pCO_2 values are inconsistent with long-term warming and the presence of continental ice sheets.

To reconcile the apparent decoupling between declining atmospheric pCO_2 and proxy-inferred warming, a "hidden" pulse of Turonian CO_2 outgassing has been proposed (Wilson et al., 2002). Alternatively, Poulsen et al. (2003) suggest that this discrepancy could be explained by a regional reorganization of the North Atlantic circulation during opening of the equatorial South Atlantic gateway, which led to seawater freshening and isotope lightening of the North Atlantic.

The hypothesized mid-Cenomanian and Turonian continental glaciations have been attributed to the evolution of Earth orbital configuration (e.g. Miller et al., 2003).

Yet, modeling studies on ice ages report the growth of detectable continental ice sheets occurs only once pCO_2 is lower than ~800 ppmv, regardless of the orbital configuration (DeConto and Pollard, 2003; Horton and Poulsen, 2009).

Collectively, these studies suggest that a more comprehensive understanding of the mid-Cretaceous climate system is hampered by the inconsistencies between proxies and models.

1.3. Outline of this dissertation

Previous studies have demonstrated that the understanding of mid-Cretaceous greenhouse climate and marine oxygen isotope record has been enhanced by the evolution of general circulation models. This dissertation tackles the long-standing problems of the mid-Cretaceous stated above using state-of-the art coupled ocean-atmosphere GCMs implemented with recently developed modules for dynamic vegetation and/or water isotope. This thesis attempts to resolve those issues by considering: 1) mechanisms and consequences of mid-Cretaceous climate change; and 2) the reliability of marine carbonate $\delta^{18}O_c$ interpretation. The integration of numerical climate modeling and geological proxy data in this dissertation provide a better constrain on the mid-Cretaceous climate change, proxy interpretation and climate model predictions.

Chapter II explores the effects of atmospheric pCO_2 and vegetation on mid-Cretaceous climate using CCSM3 and focuses on following questions:

1. Can high atmospheric pCO_2 account for the mid-Cretaceous warmth?

2. Does CCSM3 incorporating dynamic vegetation ameliorate the problem of polar warmth?
3. How did the mid-Cretaceous oceanic and atmospheric circulation response to vegetation and increased atmospheric pCO_2?

By increasing pCO_2 to the upper end of the proxy-inferred range, this study simulates a much warmer climate in mid-Cretaceous than previous modeling studies and produces the maximum warmth that could be attributed to the enhanced atmospheric pCO_2. The optional implemention of the dynamic global vegetation module in CCSM3 provides an opportunity to explore a full range of vegetation-climate interaction (Zhou et al., 2011, in review).

Due to the low resolution of mid-Cretaceous geological record, the climate variability on decadal-to-century time scale, an important component of the modern climate system, are unknown. Chapter III investigates how the Arctic variability responds to the atmospheric pCO_2 by analyzing time series of several important climate variables for the CCSM3 mid-Cretaceous experiments. The findings of this chapter provide insights into how natural variability could influence the mid-Cretaceous and future climate system.

As discussed in section 1.2, oxygen isotope paleotemperatures could be biased significantly by the assumptions of seawater oxygen isotope ($\delta^{18}O_{sw}$). Chapter IV compares the distribution of mid-Cretaceous seawater $\delta^{18}O_{sw}$ to that of modern using GENMOM with water isotope-tracking capabilities. This chapter is for the first to produce a relatively realistic distribution of mid-Cretaceous seawater $\delta^{18}O_{sw}$ and addresses three questions:

1. What was the distribution of mid-Cretaceous seawater $\delta^{18}O_{sw}$? Was it substantially different than modern values?
2. What processes controlled the distribution pattern of mid-Cretaceous seawater $\delta^{18}O_{sw?}$
3. Do model simulations support previous interpretations of the mid-Cretaceous marine carbonate $\delta^{18}O_c$? Does the simulated seawater $\delta^{18}O_{sw}$ help reconcile the discrepancy between the model simulated and proxy-inferred equator-to-pole temperature gradient?

The temporal variations of mid-Cretaceous marine carbonate $\delta^{18}O_c$ have been interpreted as the result of global climate changes. Chapter V examines the response of marine carbonate $\delta^{18}O_c$ to changes in mid-Cretaceous atmospheric pCO_2, sea level, paleogeography and proto-North Atlantic freshwater forcing using GENMOM. A comparison between the model simulated $\delta^{18}O_c$ variation and proxy record thereafter is used to assess whether the $\delta^{18}O_c$ variations truly reflect a global thermal maximum and glacial advances during the mid-Cretaceous (Zhou et al., 2008; Zhou and Poulsen, 2011, in review).

Chapter II

Vegetation-climate interactions in the warm mid-Cretaceous

Abstract

Vegetation-climate interactions are thought to have amplified polar warmth during past warm periods. Here, we explore the vegetation-climate interactions in the mid-Cretaceous using a fully coupled ocean-atmosphere general circulation model with a dynamic vegetation component. We run simulations with 1x, 10x and 16x pre-industrial atmospheric pCO_2. Results show that forests expand from mid-latitudes to high latitudes as CO_2 increases from 1x to 10x and 16x, mainly due to the CO_2-induced warming. This expansion of mid-to-high latitude forests are largely supported by the distribution of mid-Cretaceous fossil woods and coal deposits. Globally, the presence of vegetation increases mean annual temperature and precipitation by 0.9 °C and 0.11 mm day^{-1} relative to bare ground. High-latitude warming induced by the presence of vegetation (~1.9 °C) is less than half of that reported in previous studies. The weaker warming here is mainly due to less pronounced albedo feedbacks, and to a less extent, reduced poleward heat transport via weakening of the meridional overturning circulation. These vegetation-induced climate changes largely resemble CO_2-induced changes. However, model results show that high atmospheric pCO_2 and vegetation cannot achieve the estimated polar warmth. We therefore conclude that other mechanisms in addition to high atmospheric pCO_2 and

high-latitude vegetation are required to maintain the polar warmth.

2.1. Introduction

The mid-Cretaceous (~100 Ma) was a period of extreme polar warmth. Paleoclimate proxies indicate that mean annual temperature were as high as 20 ºC and 13 ºC over polar ocean and land, respectively (Bice et al., 2003; Jenkyns et al., 2004; Spicer et al., 2002, 2008). The cause of global warmth is widely accepted to be caused by high atmospheric CO_2 levels (Barron and Washington, 1985) resulting from volcanic outgassing. However, simulations of Cretaceous climate using general circulation models (GCMs) with high atmospheric CO_2 predict polar temperatures that are too cool (Barron et al., 1995; Poulsen et al., 1999, 2004; Spicer et al., 2008), challenging our understanding of greenhouse climate.

Several hypotheses have been proposed to reconcile this high-latitude model-data discrepancy including enhanced poleward heat transport via strengthening of atmospheric or oceanic circulation (e.g. Covey and Barron, 1988; Farrel, 1990; Korty et al., 2008), increased local radiative forcing through high-latitude cloud feedbacks (e.g. Abbot and Tziperman, 2008; Sloan and Pollard, 1998; Kump and Pollard, 2008), high atmospheric methane levels (Bice et al., 2006) and high-latitude forests (Deconto et al., 2000; Otto-Bliesner and Upchurch, 1997; Upchurch et al., 1998). Of these mechanisms, only the existence of high-latitude forests is directly supported by observations in the geological records (e.g., Herman and Spicer, 1996; Falcon-Lang et al., 2001; Spicer and Parrish,

1986; Spicer et al., 1993).

Previous studies have reported that the expansion of forests into polar regions in the Late Cretaceous may have warmed high-latitude regions by 4-7 ºC (Deconto et al., 2000; Otto-Bliesner and Upchurch, 1997; Upchurch et al., 1998). The warming is mainly attributed to a reduction in surface albedo due to the masking of snow via forests and melting of sea ice via transfer of heat from vegetated land to ocean. The role of vegetation feedbacks on polar warming has not been examined for the mid-Cretaceous when CO_2 levels were thought to have been higher. In addition, previous Late Cretaceous modeling studies coupled atmospheric general circulation models (AGCMs) to mixed-layer ocean models that do not allow for dynamic ocean feedbacks. Paleoclimate modeling of Cenozoic intervals has demonstrated that vegetation-induced climate change can influence the strength of the ocean meridional overturning circulation (MOC) (Brovkin et al., 2002, 2009; Ganopolski et al, 1998; Lohmann et al., 2006). Of possible relevance to Cretaceous polar warmth, Lohmann et al. (2006) report that the prescribed present to warm late-Miocene vegetation changes strengthen the North Atlantic MOC by more than 3 times, leading to a warming over the mid-to-high latitude North Atlantic by up to 8 °C. Furthermore, previous studies investigated the Cretaceous vegetation-climate interactions using prescribed vegetation changes (Otto-Bliesner and Upchurch, 1997; Upchurch et al., 1998) or an equilibrium vegetation model (Deconto et al., 2000), which do not allow realistic transient climate-vegetation interactions as in dynamic global vegetation models (Peng, 2000).

In view of the limitations of these earlier studies, we re-examine the vegetation-climate interactions in the Cretaceous under high atmospheric CO_2 using a fully coupled ocean-atmosphere GCM with a dynamic vegetation component (CCSM3). This study addresses three main questions: 1) Can CCSM3 simulate the mid-Cretaceous vegetation distribution, and if so, at what atmospheric CO_2 levels? 2) How does the simulated vegetation affect mid-Cretaceous climate? 3) Can high atmospheric pCO_2 and vegetation account for the extreme warmth during the mid-Cretaceous? We first examine the climate control on vegetation by comparing the vegetation pattern with low (1x) and high (10x and 16x) atmospheric CO_2. We then investigate the impact of vegetation on climate by comparing a simulation with the maximum simulated vegetation mass to a simulation without vegetation. Similarly, the impact of atmospheric pCO_2 is determined by comparing a simulation with 16x atmospheric pCO_2 to a simulation with 10x atmospheric pCO_2.

2.2. Methods

Cretaceous simulations were completed with NCAR's Community Climate System Model version 3 (CCSM3), a fully coupled GCM with dynamic global vegetation (Collins et al., 2006; Levis et al., 2004). CCSM3 was run in a T31x3 configuration, with a T31 spectral truncation (3.75º x 3.75º), 26-level atmosphere component model (Community Atmospheric Model) coupled to a nominal 3º, 25-level ocean component model (Parallel Ocean Program). The land surface model (Community Land Model) and

dynamic global vegetation model (CLM-DGVM) are set to the same horizontal resolution as atmosphere; the sea ice component model (Community Sea Ice Model) has the same horizontal resolution as the ocean. Vegetation distribution in CLM-DGVM is largely determined by solar radiation, air temperature, soil moisture and atmospheric CO_2 concentration (Bonan and Levis, 2006). For example, the survival and establishment of vegetation are constrained by bioclimatic parameters including monthly air temperature, growing degree days (GDD) and mean annual precipitation (Table 2-1). CLM-DGVM classifies vegetation as patches of plant function types (PFTs) (Levis et al., 2004). A PFT represents the average individual for a group of species that share similar physiological and morphological characteristics. All PFTs can coexist in a grid cell's soil-covered portion when climate allows. CLM-DGVM calculates vegetation dynamics including allocation, biomass turnover, mortality, aboveground competition, fire and establishment yearly. Levis et al. (2004) provide a detailed description of vegetation dynamics. Vegetation biogeography and structure is also updated yearly. Canopy phenology is updated daily. The communication between CLM-DGVM and the atmosphere model is achieved through exchanges of energy, momentum, and moisture every 20 minutes (Levis et al., 2004). Our version of CLM-DGVM does not simulate transient changes in atmospheric CO_2.

Table 2-1. Bioclimatic parameters for survival and establishment of plant functional type (PFT). Adapted from Table 1 in Bonan et al. (2003).

PFT	$T_{c,min}$ (ºC)	$T_{c,max}$ (ºC)	T_{hs} (ºC)	GDD (ºC·day)	P (mm yr^{-1})
Tropical broadleaf evergreen	15.5	NA	NA	NA	100
Tropical broadleaf deciduous	15.5	NA	NA	NA	100
Temperate needleleaf evergreen	-2.0	22.0	NA	900	100
Temperate broadleaf evergreen	3.0	18.8	NA	1200	100
Temperate broadleaf deciduous	-17.0	15.5	NA	1200	100
Boreal needleleaf evergreen	-32.5	-2.0	23	600	100
Boreal deciduous	NA	-2.0	23	350	100
C_3 grasses	-17.0	NA	NA	0	100

All values here are based on 20-yr running mean. $T_{c,min}$ = coldest minimum monthly air temperature for survival, $T_{c,\ max}$ = warmest minimum monthly air temperature for establishment, T_{hs} = heat stress air temperature for survival, GDD_{min} = minimum annual growing degree-days above 5 ºC, which is the sum of all positive values of difference between average daily temperature and 5 ºC in one year, P_{min} = minimum annual precipitation for establishment. The only difference between our defined PFTs and the ones in Bonan et al. (2003) is our treatement of $T_{c,\ max}$ for C_3 grasses, in order to allow C3 grasses to expand over the C_4 grass range, we eliminate the maximum temperature threshold for C_3 grasses.

Eight PFTs are defined in this study, with one herbaceous PFT (C_3 grasses) and seven woody PFTs (trees) (Table 2-1). We exclude C_4 grasses in this study because C_4 grasses did not become ecologically important until the Early-middle Miocene (Cerling et al., 1993; Jacobs et al., 1999). Though the origin of C_3 grassland is no earlier than the Late Cretaceous (Jacobs et al., 1999), we include C_3 grasses for two reasons: 1) CLM-DGVM does not have a PFT representing shrubs, therefore, shrublands are often simulated as desert or grasslands (Bonan et al., 2003); and 2) the fossil record suggested a widespread distribution of herbaceous vegetation during the mid-Cretaceous (Spicer et al., 1993).

To determine the equilibrium vegetation distribution corresponding to the mid-Cretaceous warm climate, we conducted three simulations implementing CLM-DGVM, namely, 1xDGVM, 10xDGVM and 16xDGVM (Table 2-2). An additional experiment (10xBG) was run with land surface prescribed as bare ground. Atmospheric pCO_2 concentration was set to 1x, 10x or 16x pre-industrial levels, and physiological CO_2 concentration was set to 355 ppmv in the experiments with DGVM. 16x pre-industrial levels pCO_2 likely falls in the upper limit of the estimated mid-Cretaceous atmospheric pCO_2 (see summary in Bice and Norris, 2002). All experiments were run with a reduced solar constant (99% of modern) (Gough, 1981) and present day orbital parameters. The model geography and topography were based on mid-Cretaceous (100 Ma) reconstructions from PALEOMAP project (Scotese, 2001). Because sea level was at highstand, global land area is 18.6% less than present day in our model.

Table 2-2. Mid-Cretaceous CCSM3 experiments and global annual mean surface temperature (SAT) and precipitation.

Experiment	pCO_2 (ppmv)	Vegetation	Integration (year)	SAT (ºC)	Precipitation (mm day^{-1})
1xDGVM	280	DGVM	2125	13.6	2.90
10xBG	2800	Bare ground	1626	23.1	3.36
10xDGVM	2800	DGVM	1637	24.0	3.47
16xDGVM	4480	DGVM	1615	25.6	3.56

Following Poulsen et al. (2003), we applied an age-depth relationship to reconstruct bathymetry for the deep ocean regions with known magnetic lineations (Barron, 1987). Elsewhere, deep-ocean depths were set to 5300 m. River runoff is routed to the ocean via a river transport model (Branstetter, 2001). All experiments were initiated using zonal ocean temperatures and salinity from a warm Late Cretaceous simulation (Otto-Bliesner et al., 2002). Vegetation was initialized from a 300 year integration of a Cretaceous CAM3-DGVM simulation with 10x pre-industrial pCO_2 levels. Levis et al. (2004) report that global vegetation distribution approaches equilibrium in a few hundred years in CLM-DGVM. Each of our Cretaceous experiments was run in excess of 1600 yrs (Table 2-2). The linear trend for global vegetation cover is on the order of 10^{-3}/century and is statistically insignificant. The drifts in simulated global mean ocean temperature over the last 200 years are also small (on the order of 0.1 °C/century) for all experiments.

2.3. Results

2.3.1. Response of vegetation to atmospheric pCO_2

2.3.1.1 Simulated surface temperature and precipitation

The increase of atmospheric pCO_2 leads to an increase in global annual mean surface temperature from 13.6 to 24.0 and 25.6 °C in the 1xDGVM, 10xDGVM and 16xDGVM experiments, respectively (Table 2-2). Continental surface temperatures increase by up to ~10 °C higher at low latitudes and 29 °C at high latitudes as a result of increasing CO_2 from 1 to 16x PAL (Fig. 2-1a). Consistent with the increase in surface

temperature, global annual mean precipitation increases from 2.90 mm day^{-1} in the 1xDGVM experiment to 3.47 and 3.56 mm day^{-1} in the 10xDGVM and 16xDGVM experiments (Table 2-2). The increase in continental precipitation between 1xDGVM and 16xDGVM experiments is up to 1.8 (~33%) and 1.9 (~150%) mm day^{-1} at low and mid-to-high latitudes. In contrast, the continental precipitation decreases by ~0.3 mm day^{-1} (~20%) in the southern subtropical latitudes (~20-30 °S) (Fig. 2-1b).

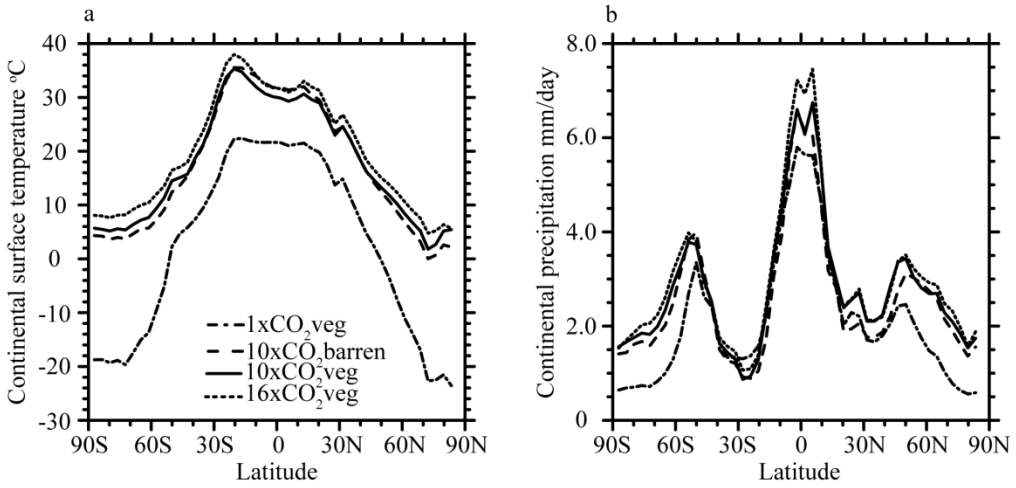

Figure 2-1. Zonal−average annual mean continental surface temperature (ºC) (a); and precipitation (mm day^{-1}) (b) for the 1xDGVM (black dash-dot line), 10xBG (black dashed line), 10xDGVM (black solid line) and 16xDGVM (black dotted line) experiments, respectively.

2.3.1.2 Simulated global vegetation distribution

In the 1xDGVM experiment, the tropics, subtropics, mid-latitudes and high latitudes are dominated by evergreen trees, grasses, mixture of evergreen and deciduous trees and polar desert, respectively (Fig. 2-2 a-c). In the high CO_2 experiments, trees (especially deciduous) and grasses advance into the northern high latitudes and Antarctica (Fig. 2-2d-i). In the northern high latitudes (60-90 °N**),** average fractional tree cover over the soil-covered land increases from 0.7% in the 1xDGVM experiment to 61% (10xDGVM) and 59% (16xDGVM). The change in tree cover at the southern high latitudes (60-90 °S) is slightly less than the northern high latitudes, increasing from 4% (1xDGVM) to 51% (10xDGVM) and 43% (16xDGVM). In contrast, tree cover at low latitudes (30 °S-30 °N) decreases from 60% (1xDGVM) to 54% (10xDGVM) and 50% (16xDGVM). As a result of the poleward expansion of trees and grasses, area-weighted global vegetation cover increases from 56% (1xDGVM) to 85% (10xDGVM and 16xDGVM). Global net primary production (NPP), which is equal to the net gain of carbon through photosynthesis and respiration, is estimated to be 61.8 Pg C/yr in the 1xDGVM experiment, comparable to observational estimates of present-day NPP (Schlesinger 1997). Due to the increase in global vegetation cover, NPP increases by 13.5 PgC yr^{-1} (21.8%) in the 10xDGVM experiment and 10.9 PgC yr^{-1} (17.6%) in the 16xDGVM experiment relative to the 1xDGVM experiment.

The large-scale changes in vegetation distribution are linked to changes in surface temperatures and precipitation. The expansion of trees and grasses at mid- and high

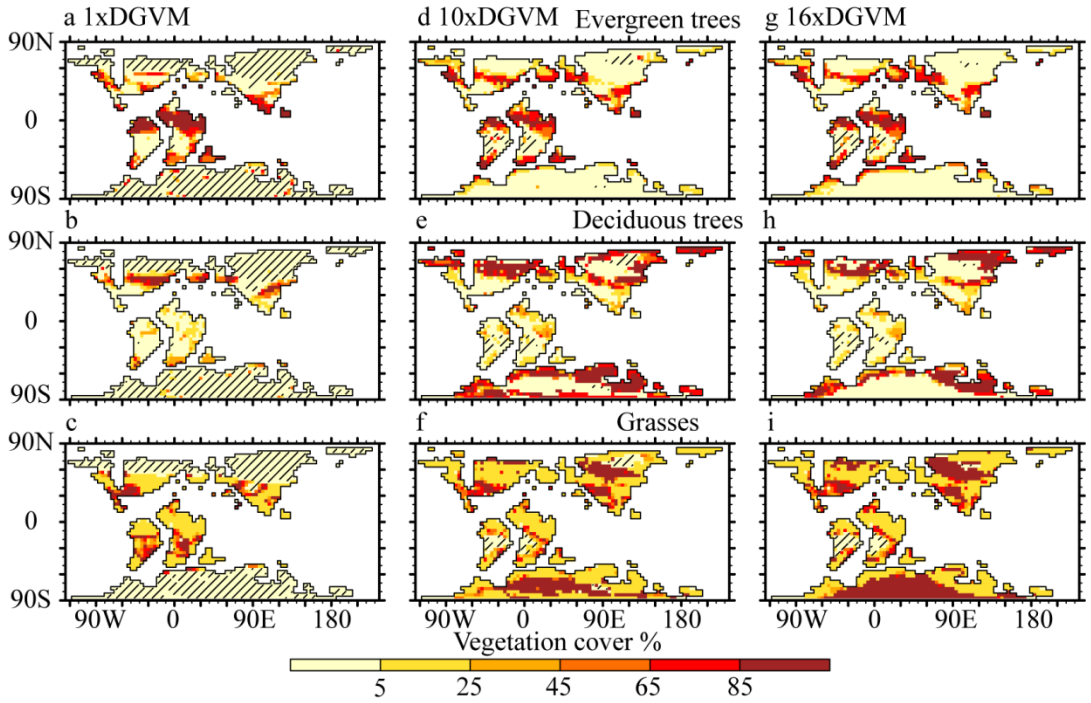

Figure 2-2. Global distribution of evergreen trees (a), (d), (g), deciduous trees (b), (e), (h) and grasses (c), (f), (i) (%) for the 1xDGVM, 10xDGVM, and 16xDGVM experiments, respectively. Land area with <10% vegetation cover, which is defined as desert, is shaded. Note, hereafter, continental outlines delimit area with >50% land cover. Evergreen trees include tropical and temperate broadleaf evergreen, and temperate and boreal needleleaf evergreen. Deciduous trees include tropical and temperate broadleaf deciduous and boreal deciduous.

latitudes in the two high CO_2 experiments is mainly due to CO_2-induced warming (Fig. 2-1a). In the 1xDGVM experiment, GDD (i.e. annual growing degree- days above 5 ºC), which measures the accumulation of growing season warmth in a year, is largely less than 350 ºC·day at high latitudes inhibiting tree growth (Table 2-1) and the minimum monthly temperature is lower than -17 ºC prohibiting grass growth (Table 2-1). In contrast, in the high CO_2 experiments, GDD is generally greater than 1200 ºC·day except in the cold Siberian interior due to the large increase in surface temperature (Fig. 2-1a), providing a sufficient growing season for all tree PFTs to thrive (Table 2-1). In addition, the minimum monthly temperature exceeds -17 ºC, allowing the establishment of temperate trees and grasses. The retreat of subtropical grasses in the Southern Hemisphere in the two high CO_2 experiments is caused by a decrease in precipitation associated with enhanced subtropical subsidence. The decrease in low-latitude evergreen tree cover and increase in deciduous tree cover with higher CO_2 are also associated with the decrease in precipitation (Fig. 2-1b).

The poleward expansion of trees at mid-to-high latitudes under high atmospheric CO_2 matches the fossil data reasonably well (Fig. 2-3). The simulated dominant woody PFTs at mid- and high-latitude North America, Greenland, coastal Eurasia, New Zealand, Australia and coastal Antarctica are supported by fossil woods and coal deposits (Beerling et al, 1999; Falcon-Lang et al., 2001; Herman and Spicer, 1996; and Price et al, 1997). In contrast, the simulated predominant woody PFTs in the tropical South America and Africa appears inconsistent with the presence of fossil elaterate assemblages, a

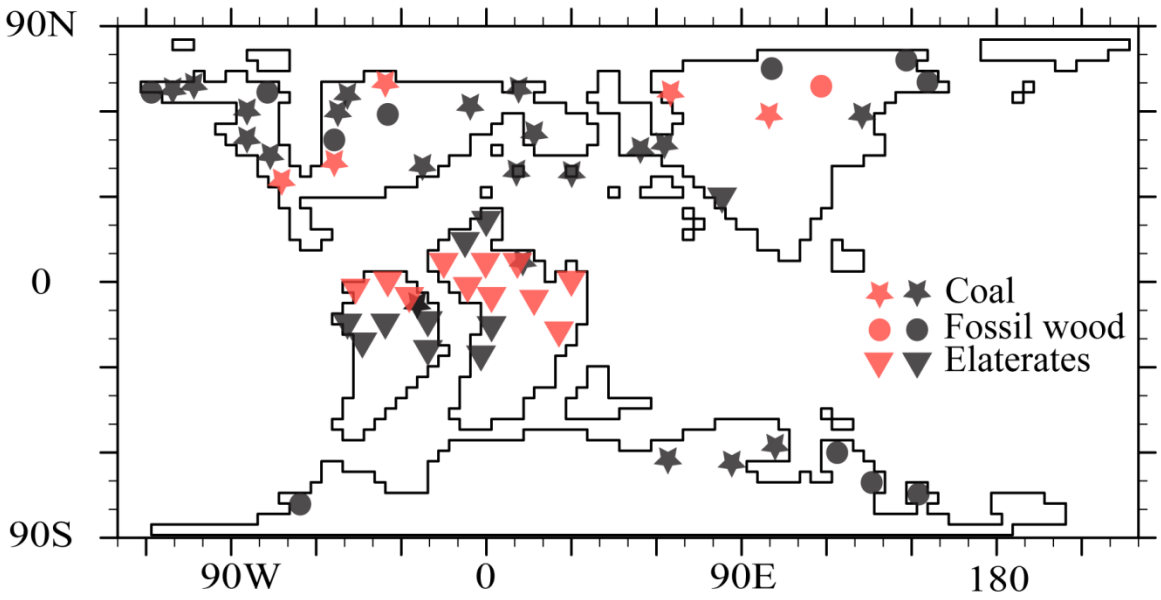

Figure 2-3. Distribution of mid-Cretaceous vegetation inferred from fossil wood, pollen of Elaterate assemblages and coal deposits and comparison with simulated vegetation. Fossil wood (solid circle) and coal deposits (solid star) are indicators of high-productivity forests; fossil pollen of Elaterates assemblages (down triangle) indicates dry climate and/or mangrove swamps and savannah (Dino et al., 1999; Ziegler et al., 2003). Paleofloral data is adapted from Beerling et al. (1999), Dino et al. (1999), Falcon-Lang et al. (2001), Herman and Spicer (1996), and Price et al. (1997). The shading of symbols shows agreement between the simulated vegetation in the 10xDGVM experiment and paleofaunal data. Black indicates that the model simulates the observed faunal type; red indicates that it does not. The model-data comparison (not shown) is nearly identical for the 16xDGVM experiment.

unique palynoflora assemblage indicating arid climate (Dino et al., 1999). The dense tropical trees simulated in our model are similar to the simulated mid-Cretaceous vegetation pattern by the University of Sheffield dynamic global vegetation model or FOAM-LPJ (Beerling et al., 1999; Donnadieu et al., 2009).

2.3.2 Impact of vegetation and atmospheric pCO_2 on mid-Cretaceous climate

2.3.2.1 Surface temperature

The presence of vegetation in the 10xDGVM experiment increases mid-Cretaceous global surface temperature by 0.9 ºC (Table 2-2). Changes in surface temperature show significant spatial (Fig. 2-4b) and seasonal variations (Fig. 2-5a, f & k). High-latitude forested areas experience annual warming of 2.3 ºC with early summer warming of up to 4.0 ºC (Fig. 2-4b & Fig. 2-5a). In contrast, low-latitude forested areas undergo year-round cooling (Fig. 2-4b & Fig. 2-5f). Mid-latitude Northern Hemisphere surface temperatures increase during the cold seasons and decrease during the warm seasons (Fig. 2-5k). Changes in surface temperatures over ocean are generally less than 1 ºC at low latitudes and up to 3 ºC at high latitudes (Fig. 2-4b). The maximum increase in surface temperature (> 5 ºC) occurs in the mid-latitude North Pacific, and is caused by the poleward shift of western boundary currents (explained in section 2.3.2.3).

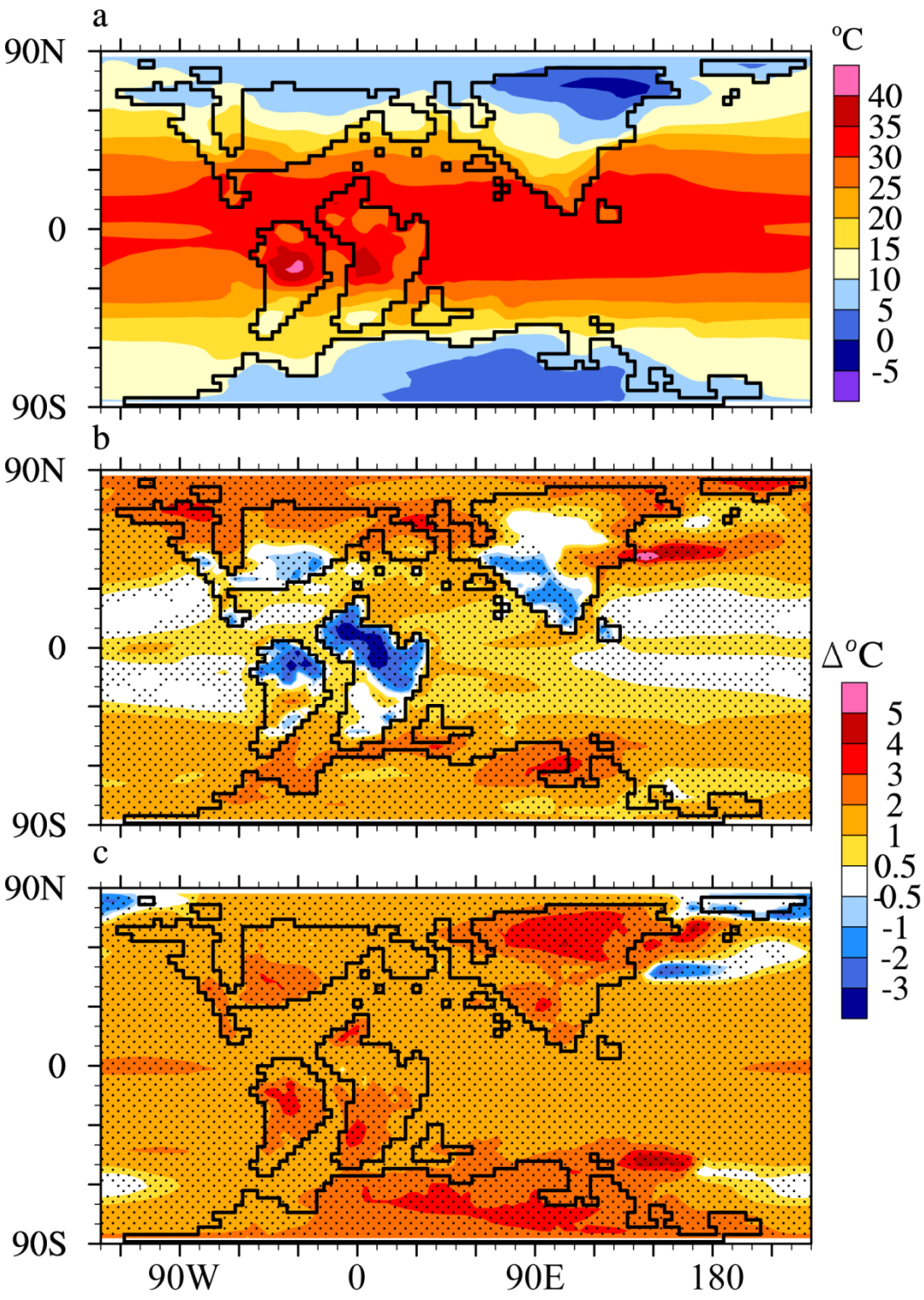

Figure 2-4. Mean annual surface temperature (ºC) for the 10xDGVM experiment (a); 10xDGVM – 10xBG experiments (b); and 16xDGVM - 10xDGVM experiments (c). The differences exceed 95% confidence level are shaded.

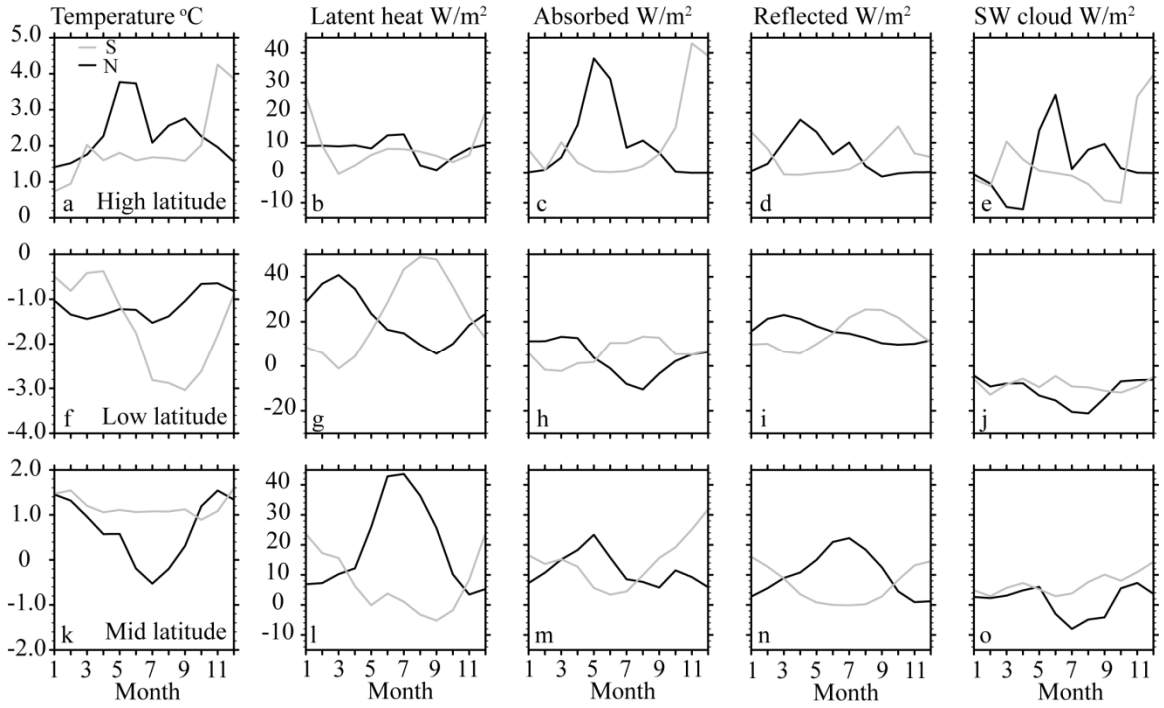

Figure 2-5. Annual cycles of surface temperature (ºC), latent heat fluxes (W m^{-2}), surface absorbed solar radiation (W m^{-2}), surface reflected solar radiation (W/m2), surface shortwave cloud forcing (W m^{-2}) over the high-latitude forests (a-e), low-latitude forests (f-j) and mid-latitude forests (k-o) for 10xDGVM – 10xBG experiments. Solid black lines denote changes in the Northern Hemisphere and grey lines denote changes in the Southern Hemisphere.

The changes in land surface temperature can be explained by the net effect of vegetation-induced changes in latent heat fluxes and surface absorbed solar radiation. The former results from changes in evapotranspiration (Fig. 2-6a); the latter is mainly due to changes in surface albedo (Fig. 2-6b) and low-cloud cover (Fig. 2-6c). As a result of canopy evapotranspiration, the total annual mean evapotranspiration over land increases by 0.38 mm day^{-1} (22.7%) in the 10xDGVM experiment relative to the 10xBG experiment (Fig. 2-6a). And the increase (> 1.0 mm day^{-1}) is most significant over the low-to-mid latitude evergreen forests. In contrast, the annual mean land surface albedo decreases by 0.04 (~20%) in the 10xDGVM experiment (Fig. 2-6b and Table 2-3), due to the darkening of land surface via forests, and to a less extent via reduced snow cover. The reduction (up to 0.2) is most pronounced over mid-to-high latitude deciduous forests through snow-masking (Fig. 2-6b). Seasonally, over high-latitude forests, the net surface radiation (i.e. the difference between surface absorbed solar radiation and net upward longwave radiation) increases by ~24 W m^{-2} due to the large gain in surface absorbed solar radiation (> 31 W m^{-2}) during late spring and early summer (Fig. 2-5c), which greatly exceeds increases in latent heat fluxes (Fig. 2-5b), leading to significant warming (Fig. 2-5a). The increases in surface absorbed solar radiation are due to 1) decreases in surface reflected solar radiation associated with the reduction in surface albedo (Fig. 2-5d), and 2) increases in incoming solar radiation associated with reduced low cloud cover (Fig. 2-6c). The decreases in low cloud cover are linked to the reduced boundary layer relative humidity with increased temperatures. In contrast, over low-latitude forests,

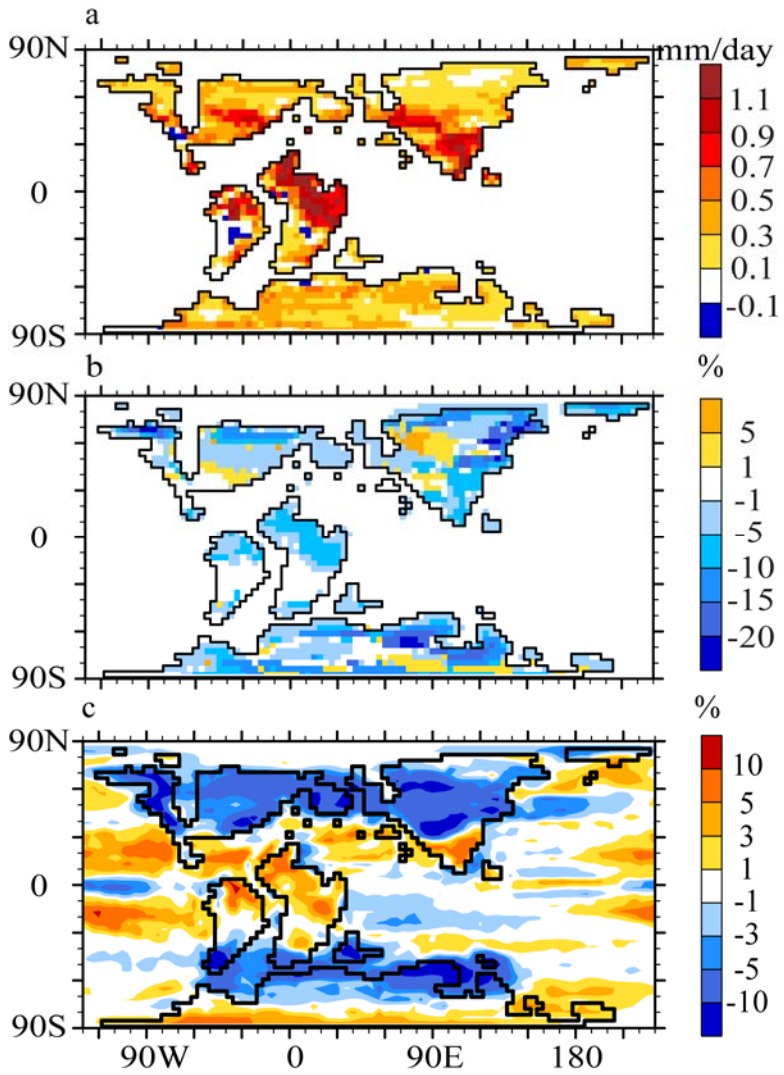

Figure 2-6. Annual mean a) total evapotranspiration over land (mm day^{-1}); b) surface albedo (%); and c) low cloud cover (%) for the 10xDGVM – 10xBG experiments (%).

Table 2-3. Global and high-latitude annual mean climatic variables in the 10xBG and 10xDGVM experiments

Variable	10xDGV	10xDGVM -10xBG	16xDGVM -10xDGVM
SAT (land, 60 – 90 ºN, ºC)	6.3	1.9	2.3
SAT (ocean, 60 – 90 ºN, ºC)	10.0	1.9	1.4
SAT (land, 60 – 90 ºS, ºC)	6.4	1.7	2.7
SAT (ocean, 60 – 90 ºS, ºC)	12.3	1.3	1.4
Snow fraction (land, 60 – 90 ºN)	0.09	-0.03	-0.03
Snow fraction (land, 60 – 90 ºS)	0.10	-0.04	-0.04
Polar sea ice fraction	0.002	-0.003	-0.002
Surface albedo (land)	0.173	-0.04	-0.002
Surface albedo (land, , 60 – 90 ºN)	0.216	-0.057	-0.019
Surface albedo (land, , 60 – 90 ºS)	0.242	-0.062	-0.011
Surface LW↓ (ocean, W m^{-2})	404.0	7.3	15.8
Latent heat fluxes↑ (W m^{-2})	100.5	3.4	2.7
Latent heat fluxes↑ (land, W m^{-2})	59.9	11.1	2.4
Precipitable water (kg m^{-2})	41.1	3.3	6.1
Precipitation (land, mm day^{-1})	2.95	0.26	0.15
Snow (land, mm day^{-1})	0.10	-0.02	-0.04
Precipitation (ocean, mm day^{-1})	3.64	0.07	0.07
Evapotranspiration (land, mm day^{-1})	2.07	0.38	0.06
MOC (Northern Hemisphere, Sv)	16.9	-4.5	-7.7
MOC (Southern Hemisphere, Sv)	8.3	-1.0	-3.5
OHT (Northern Hemisphere, PW)	1.61	-0.23	-0.16
OHT (Southern Hemisphere, PW)	1.09	-0.07	-0.10

increases in latent heat fluxes are up to 31 (26) W m^{-2}greater than increases in surface absorbed solar radiation in the Northern (Southern) Hemisphere (Fig. 2-5 g&h) leading to significant cooling (Fig. 2-5f). The increases in absorbed solar radiation are significantly smaller than the surface albedo feedback (Fig. 2-5i), because low-latitude forest evapotranspiration leads to denser low cloud cover (Fig. 2-6c), and thus offsets the surface albedo feedback by reducing incoming solar radiation at the surface (Fig. 2-5j). Over the northern mid-latitude forests, the increases in latent heat fluxes are up to 35 W m^{-2}greater than increases in absorbed solar radiation during summer (Fig. 2-5 l&m) leading to summer cooling (Fig. 2-5k).

Unlike over land, changes in surface albedo are negligible over ocean except the northern Eurasian coastal area (Table 2-3 and Fig. 2-4c). The large-scale background warming over ocean results from the increase in downwelling longwave radiation (7.3 W m^{-2}) (Table 2-3) associated with elevated atmospheric water vapor content (correlation > 0.7). Warming over the southern South Atlantic and Tethys Ocean, the equatorial and northern mid-latitude Pacific Ocean, and the Western Interior Seaway is also enhanced by positive cloud radiative forcing due to reduced low cloud cover (Fig. 2-6c). In contrast, warming over the subtropical Pacific Ocean is suppressed by negative cloud radiative forcing due to increased low cloud cover.

Increasing atmospheric pCO_2 from 2800 to 4480 ppmv increases global temperature by 1.6 ºC (Table 2-2). Similar to vegetation effect, the more pronounced warming over the Antarctica and Siberian continental interiors (Fig. 2-4c) are due to

snow-albedo feedback (Fig. 2-7a). The large-scale background warming over ocean (~1.5 ºC) is mainly attributed to the increase in downwelling longwave radiation (15.8 W m^{-2}) (Table 2-3). The surprise cooling over the subpolar northern and southern Pacific Ocean is associated with the weakening of NMOC (Table 2-3). And the cooling is further intensified by low-cloud forcing (Fig. 2-7b).

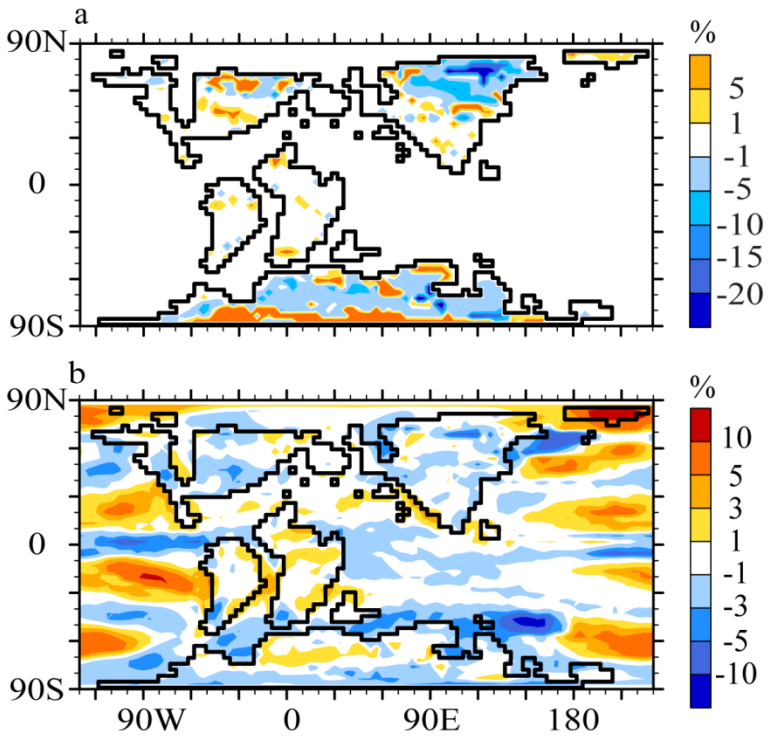

Figure 2-7. Difference between the 16xDGVM and 10xDGVM experiments for the annual mean surface albedo (%) (a); and low cloud cover (%) (b).

2.3.2.2 Precipitation

From a global perspective, the presence of vegetation slightly intensifies the mid-Cretaceous hydrological cycle (Table 2-3). As a result of the increases in the surface temperature and evapotranspiration, the global precipitable water (i.e. vertically integrated specific humidity) and precipitation increases by 3.3 kg m^{-2} (8.7%) and 0.11 mm day^{-1} (3.3%), respectively. In contrast, snowfall decreases by 0.02 mm day^{-1} (17%) over land. The increases in precipitation are more pronounced over land (0.26 mm day^{-1}, 9.7%) than over ocean (0.07 mm day^{-1}, 2.0%). Due to enhanced precipitation, the freshwater flux into the high-latitude North and South Pacific Ocean increases by 0.05 Sv (15.2%) and 0.03 Sv (11.5%), respectively.

The presence of vegetation leads to significant regional changes in precipitation (Fig. 2-8b), though the large-scale precipitation pattern remains unchanged. The most significant regional changes (> 1.0 mm day^{-1}) occur over the low-to-mid latitude forests, intertropical convergence zones (ITCZ) and mid-latitude Western Pacific. The increases in continental precipitation are mainly due to the enhanced recycling of water via canopy evapotranspiration, with a point-to-point correlation larger than 0.6 over most areas. In contrast, the changes in precipitation over ocean mainly reflect changes in large-scale atmospheric circulation, as shown by the changes in zonal-average annual mean meridional streamfunction (Fig. 2-9a). The Hadley cells weaken by 3.2 * 109 kg s^{-1} (3%) and 6.3 * 109 kg s^{-1} (7%) in the Northern and Southern Hemisphere, respectively, due to the reduced equator-to-pole temperature gradient.

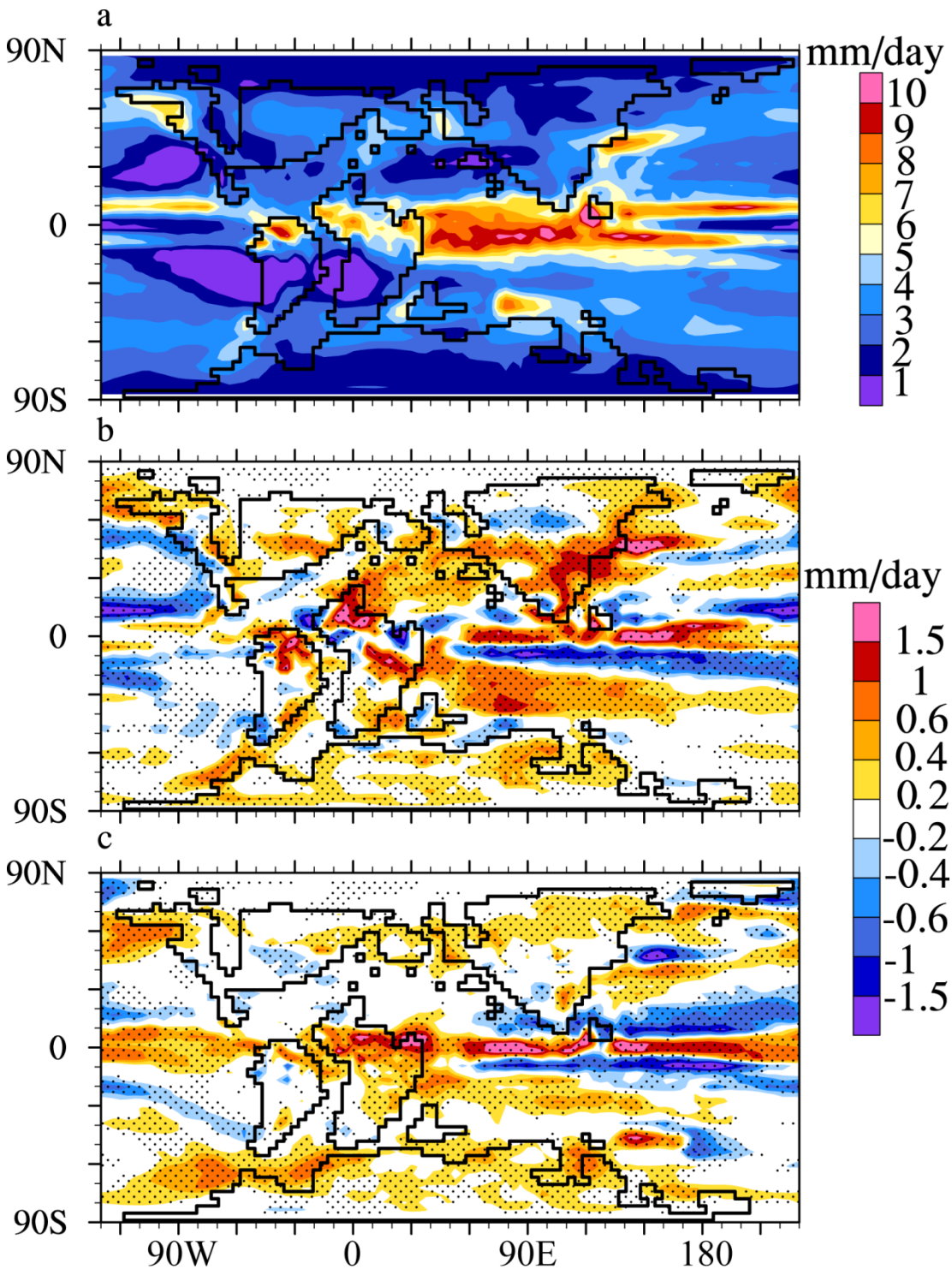

Figure 2-8. Mean annual precipitation (mm day^{-1}) for the 10xDGVM experiment (a); 10xDGVM – 10xBG experiments (b); and 16xDGVM - 10xDGVM experiments (c). The differences exceed 95% confidence level are shaded.

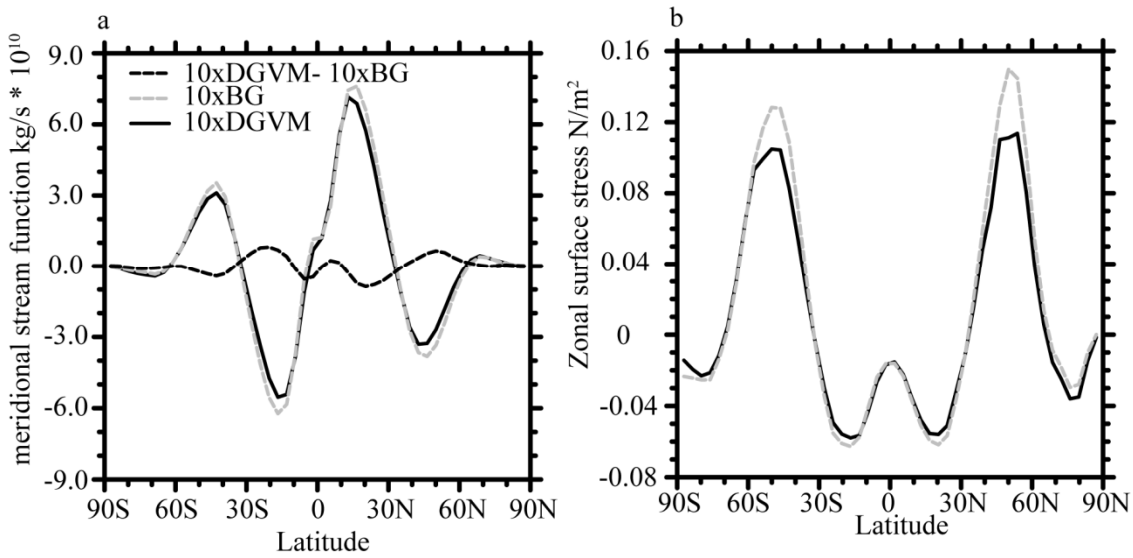

Figure 2-9. Zonal-average annual mean meridional streamfunction (10^{10} kg s^{-1}) at 400 mb (a); and wind stress (N m^{-2}) over the Pacific Ocean (b) for the 10xDGVM (black solid line) , 10xBG (grey dashed line) and 10xDGVM – 10xBG experiments (black dashed line), respectively.

In addition, the ascending branches of the Hadley cells contract equatorward (from ~16.7 ºN/S to 13.0 ºN/S). The equatorward contraction in each hemisphere mainly occurs during winter and spring seasons when the Hadley cell expands to the other hemisphere (not shown). The weakening and contraction of Hadley cells cause anomalous ascending motion at equatorial latitudes (~5 ºS-5 ºN) and ~20-40 ºN/ºS and anomalous subsidence at ~10-20 ºN/ºS. As a result, precipitation increases at ~5 ºS-5 ºN and 20-40 ºN/ºS and decreases at ~ 10-20 ºN/ºS. The increase in precipitation at mid-latitude North Pacific is associated with warming due to a poleward shift of the western boundary currents.

The changes in precipitation induced by increasing atmospheric pCO_2 largely resemble the vegetation-induced changes (Fig. 2-8 b-c), especially at low latitudes. In the absence of significant increase in evapotranspiration, the increase in continental precipitation resulted from increasing atmospheric pCO_2 is less than that caused by the presence of vegetation, despite a more pronounced warming (Table 2-3).

2.3.2.3 Ocean circulation response

The reduction in the equator-to-pole temperature gradient in the 10xDGVM experiment leads to a decrease in zonal wind strength. As shown in Fig.2-9b, the maximum zonal-mean wind stress over the Pacific Ocean decreases by 0.02 N/m^2 (~13%) in the Southern Hemisphere and 0.03 N m^{-2} (~20%) in the Northern Hemisphere. As a result, the maximum intensity of the subtropical gyres decreases by 7.9 Sv (10%) from 77.1 Sv (10xBG) to 69.2 Sv (10xDGVM) in the Northern Hemisphere and by 14.0 Sv

(13.3%) from 105.4 Sv (10xBG) to 91.4 Sv (10xDGVM) in the Southern Hemisphere. In addition, the mean position of the maximum wind stress shifts poleward by a grid cell (3.75º) from 50.1 ºN to 53.8 ºN in the Northern Hemisphere. Consistent with this poleward shift in wind stress, the western boundary current shifts from ~43 ºN in the 10xBG experiment to ~46 ºN in the 10xDGVM experiment in the western North Pacific. This poleward displacement of warm, saline subtropical water leads to the significant increase in temperature (> 5 ºC) (Fig. 3-4b) and salinity (>2 PSU) at ~45 ºN.

The global MOC also decreases in the 10xDGVM experiment. As shown in Fig. 2-10 a-b, the maximum magnitude of MOC decreases by 1.0 Sv (~11%) from 9.3 Sv in the 10xBG experiment to 8.3 Sv in the 10xDGVM experiment in the Southern hemisphere and decreases by 4.5 Sv (~21%) from 21.4 Sv in the 10xBG experiment to 16.9 Sv in the 10xDGVM experiment in the Northern hemisphere. This decrease is 0.8 Sv larger than CO_2-induced decrease between the 10xDGVM and 1xDGVM (20.6 Sv) experiments. The slight weakening of MOC in the Southern Hemisphere is caused by warming (Fig. 2-4b) and freshening through enhanced precipitation (Fig. 2-8b) of the high-latitude South Pacific. In addition to the freshening via enhanced precipitation, the poleward migration of the low-salinity subpolar front associated with the poleward shift of the western boundary currents, also contributes to the decrease in seawater salinity at the high-latitude North Pacific. As a result, deep water formation along the Northeast coast of Asia vanishes and MOC slows down in the Northern Hemisphere.

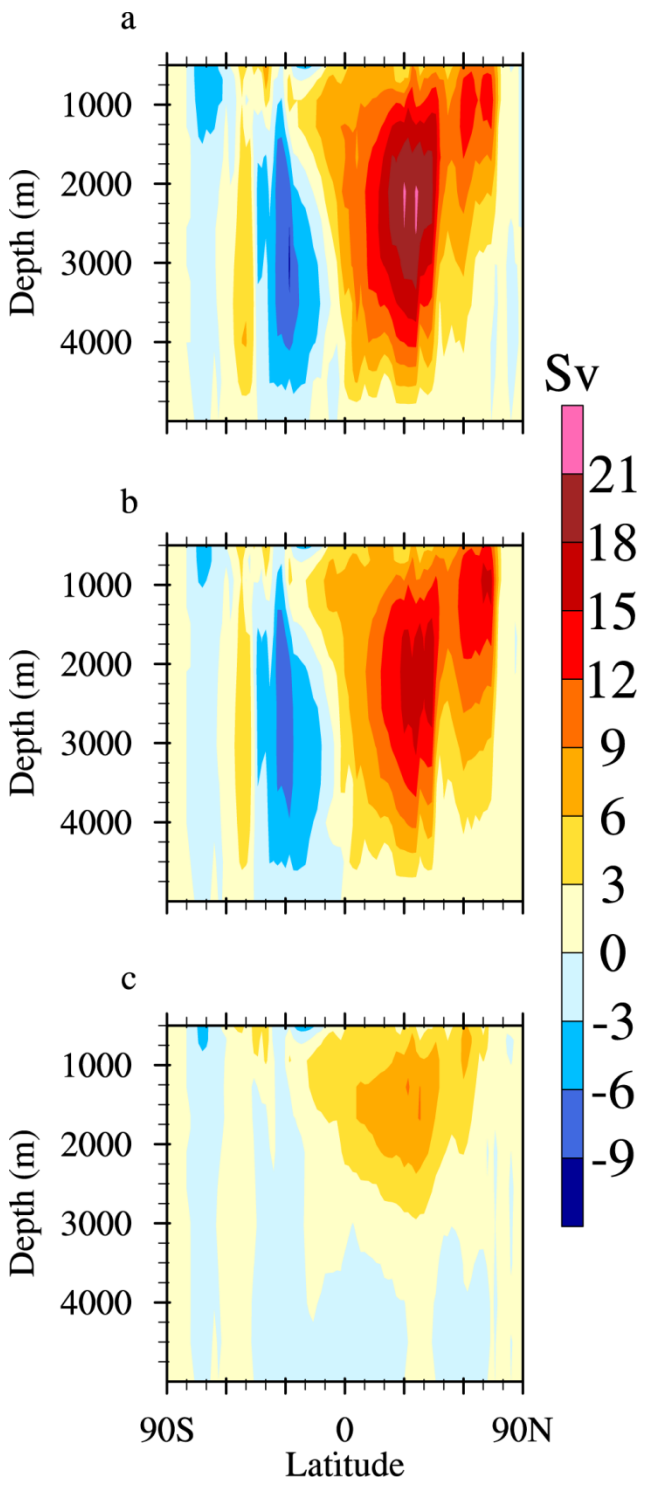

Figure 2-10. Annual mean Meridional overturning circulation (Sv) for a) 10xDGVM experiment; and b) 10xBG experiment. Positive (in yellow and red) means clockwise flow direction and negative means counterclockwise flow direction.

In response to the weakening of MOC, poleward oceanic heat transport decreases by 0.07 PW (~6%) in the Southern Hemisphere and 0.23 PW (~13%) in the Northern Hemisphere (Table 2-3). This decrease in poleward heat transport diminishes the warming over the high-latitude Pacific Ocean (~ 70 ºS/ ºN) (Fig. 2-4b).

Similarly, as atmospheric pCO_2 increases from 2800 to 4480 ppmv, MOC decreases by 7.7 Sv (45.6%) in the Northern Hemisphere and 3.5 Sv (42.2%) in the Southern Hemisphere (Fig. 2-10). As a result, poleward oceanic heat transport decreases by 0.10 PW (~9%) in the Southern Hemisphere and 0.16 PW (~10%) in the Northern Hemisphere (Table 2-3). This decrease in poleward heat transport diminishes the warming over the high-latitude Pacific Ocean (~ 70 ºS/ ºN) (Fig. 2-4c).

2.4. Discussion

2.4.1 The role of vegetation feedbacks under high CO_2

Our results show that vegetation acts to warm high latitudes and cool low latitudes in a warm climate with high CO_2, similar to the role of modern vegetation (Bonan, 2008). The simulated warming effect of high-latitude forests on polar regions is also consistent with previous Cretaceous studies (Deconto et al., 2000; Otto-Bliesner and Upchurch, 1997; Upchurch et al., 1998). However, our simulated reduction in high-latitude surface albedo (~0.06) and the associated warming (< 2 ºC) are more than one-half less than in these studies, mainly because we assess the impact of vegetation in a warm mean climate with little snow (< 0.15) and sea ice (< 0.01) (Table 2-3). In contrast,

using a atmospheric CO_2 value of 580 ppmv, Upchurch et al. (1998) report that snow and sea ice fraction are up to 0.62 and 0.38, allowing a stronger vegetation-snow-sea ice albedo feedback. The weaker warming here is also linked to the decrease in poleward oceanic heat transport resulting from the weakening of MOC, which is not resolved in the earlier studies. The simulated mean annual temperatures over the Eurasian interior and Arctic Ocean only increase ~2 ºC by vegetation and are up to 10 ºC lower than those estimated by proxies such as leaf physiognomy (Spicer et al., 2002, 2008) and TEX_{86} method (Jenkyns et al., 2004) (Fig. 2-11). Therefore, we conclude that high-latitude forests can only be considered a secondary mechanism for the mid-Cretaceous polar warmth. Other mechanisms in addition to high atmospheric CO_2 and high-latitude vegetation are required to maintain the polar warmth.

We find that ~20-40 % of the increase in surface absorbed solar radiation over high-latitude forests is due to cloud feedbacks. In fact, the increase in cloud radiative forcing surpasses the albedo feedback during late spring and early summer (Fig. 2-5 d, e). This positive cloud feedback contradicts a previous study (Betts, 1999), which reports that the presence of vegetation induced a high-latitude summer cooling of > 2 ºC mainly by reducing surface solar radiation via enhanced cloud cover. These contrasting results highlight the uncertainty of cloud feedbacks in determining the overall effect of high-latitude forests.

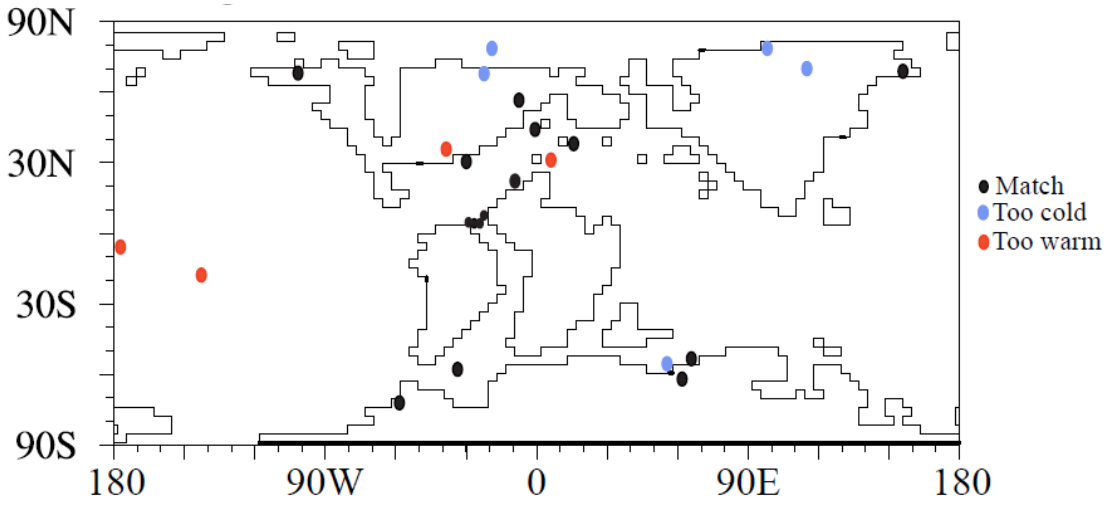

Figure 2-11. Model-data comparison for mid-Cretaceous surface temperature. Red dots denote that model temperatures are higher than proxy estimates, black dots denote that model temperatures are comparable to proxy estimates, and blue dots denote that model temperatures are lower than proxy estimates. See Chapter I for proxy references.

2.4.2 Oceanic circulation

Our simulations are consistent with modeling studies with a dynamic ocean component that vegetation can have an important impact on MOC, due to vegetation-induced changes in hydrological cycle and sea surface temperature (Brovkin et al., 2002, 2009; Ganopolski et al, 1998; Lohmann et al., 2006). Moreover, our simulations suggest that the response of MOC to vegetation could exceed that of a tenfold increase in atmospheric CO_2 concentration. Proxy records and model studies demonstrate that global vegetation pattern is highly correlated with climate changes during the geological past and future (e.g., Spicer and Chapman, 1990; Alo and Wang, 2008; Cramer et al., 2001). Therefore, vegetation-climate interactions should be taken into account for simulating the MOC response to past and future climate change.

2.5. Caveats

In the absence of global paleovegetation reconstructions, most previous modeling studies of the mid-Cretaceous have assumed a uniform vegetation type on all continents (e.g. Donnadieu et al., 2006; Poulsen et al., 2007; Zhou et al., 2008). In this contribution, we use a dynamic vegetation model to overcome this limitation. We emphasize, though, that the simulation of pre-Quaternary vegetation is subject to uncertainty, mainly due to a paucity of evidence for the construction and physiology of past ecosystems. Due to our lack of understanding of past ecosystems, paleo-vegetation modeling relies on a modern understanding of PFTs and their bioclimatic, physiological, and dynamic relationships

that may not be entirely appropriate for past times. For example, grass, which is a dominant PFT at present, had not evolved yet in mid-Cretaceous. We keep grass in our simulation because it is the only available herbaceous PFT. Another substantial change between the modern and mid-Cretaceous is angiosperms. The modern angiosperm-dominated tropical forests may not have appeared until the Paleocene (Burnham and Johnson, 2004). Yet our simulations show extensive tropical forests resembling the modern distribution, an overestimation that may be linked to the inclusion of PFTs that represent modern angiosperm trees. Consequently, CLM-DVGM may overestimate the impact of low-latitude vegetation on mid-Cretaceous climate, because angiosperms have a much larger impact on hydrology relative to other plants due to their high transpiration capacity (Boyce and Lee, 2010). To more accurately simulate the mid-Cretaceous vegetation and its feedbacks, more paleo-vegetation data is needed to appropriately parameterize the mid-Cretaceous dominant PFTs.

2.6. Conclusions

We investigate the vegetation-climate interaction using a coupled ocean-atmosphere GCM (CCSM3) with a dynamic vegetation component. The model demonstrates a positive feedback between vegetation and polar climate – CO_2-induced warming promotes expansion of high-latitude forests, which leads to additional polar warming via reducing surface albedo and low cloud cover. However, the warming effect

of vegetation at high latitudes is smaller than reported in previous studies, mainly due to the less pronounced surface albedo feedback in the absence of large snow and sea ice cover under the simulated warm mean climate. Over low latitude continents, the feedbacks between vegetation and climate are opposite; forest cover decreases with higher CO_2, and the presence of forests leads to year-round cooling. The cooling is associated with enhanced evpotranspiration and low cloud cover.

The simulation of mid-Cretaceous vegetation has unexpected effects on the ocean, and largely resembles CO_2 effect. First, as a result of the enhanced atmospheric vapor content with vegetation, downwelling longwave radiation increases over ocean, leading to surface warming at sea surface. Second, vegetation alters wind fields, resulting in weakening of wind-driven subtropical and subpolar gyres and poleward displacement of the North Pacific western boundary current. Lastly, the intensified precipitation enhances the freshwater flux into the high-latitude Pacific. This freshening in conjunction with surface warming reduces the meridional overturning circulation in both hemispheres, which reduces meridional heat transport and damps high-latitude warming.

Chapter III

Abrupt Arctic warming in a greenhouse climate

Abstract

Past abrupt climate change has previously been linked to external forcing in a glacial climate. Here we report on unforced abrupt warming in a simulation of the Cretaceous greenhouse using NCAR's CCSM ocean-atmosphere model. After ~800 model years, the Arctic experiences a warming of 1.6 °C within ~30 years that persists for the duration of the simulation (>800 yrs), and initiates a gradual intensification by ~50% of the ocean meridional overturning circulation. This event is triggered by transport of saline subtropical water into the high latitudes, and sustained by an increase in local surface heat flux, atmospheric convection and cyclonic flow. Polar warming is mainly due to a breakdown of static stability in the Arctic troposphere, which reduces low-cloud amounts and increases cloud radiative forcing. Our results provide a new mechanism for polar temperature amplification and past thermohaline reorganization, and identify a climate hysteresis in a world with less sea ice that leads to abrupt and long lasting polar warming.

3.1. Introduction

Abrupt climate change describes the transition of the climate system across a threshold to a new state at a rate faster than the cause (Alley et al., 2003), and usually refers to transitions that occur on timescales of human relevance (typically <~30 yrs). The paleoclimate record shows that large, abrupt cooling events have repeatedly occurred in the past. The Dangaard-Oeschger oscillations, Heinrich events, the Younger Dryas, and the 8.2 kyr event were triggered by massive meltwater discharge events associated with the wasting of continental ice sheets (Overpeck and Cole, 2006). Surprisingly, there are no unambiguous cases of abrupt climate change in warm climates. The most famous candidate, the Paleocene-Eocene thermal maximum, occurred on longer timescales (~10^5 yrs) likely due to the destabilization of oceanic methane hydrate (Thomas et al., 2002).

The mid-Cretaceous was one of the warmest periods in Earth history, and warmest in the last 100 Ma. Mid-Cretaceous (90-100 Ma) CO_2 levels are estimated from fossil leaf stomatal indices, soil carbonate proxy records, and biomarker $\delta^{13}C$ to range between 2 and 16 times pre-industrial levels (<700 ppmv and >4000 ppmv) (Bice et al., 2006; Haworth et al., 2005; Retallack, 2001). Consistent with high greenhouse gas concentrations, Cretaceous surface temperatures were considerably higher than modern. Low-latitude marine temperatures are estimated to have been ~33 (±3) °C (Norris et al., 2002; Schouten et al., 2003; Wilson et al., 2002), approximately 6 °C warmer than present. High-latitude continents were warm with mean-annual temperatures above 0 °C and up to 10 °C (Parrish and Spicer, 1988; Spicer et al., 2008). Arctic surface waters are

estimated to have been ~15 °C and ice free during summer (Davies et al., 2009).

Here we report on abrupt climate warming in a Cretaceous simulation completed using the fully coupled ocean-atmosphere GCM, Community Climate System Model Version 3 (CCSM3).

3.2. Methods

The Cretaceous simulations were developed using the NCAR Community Climate System Model version 3 (CCSM3), a fully coupled ocean-atmosphere-sea ice-land surface with dynamic global vegetation global climate model (Collins et al., 2006). The atmospheric model, the NCAR Community Atmosphere Model (CAM3), is run with a T31 spectral resolution and 26 vertical levels. The land surface model, the Community Land Model (CLM3.0) (Dickinson et al., 2006), has the same horizontal resolution as CAM3 and is coupled to the Lund-Potsdam-Jena dynamic vegetation model (DGVM) (Levis et al., 2004). River drainage routes were based on surface topography such that flow runs downhill.

The ocean model, the Parallel Ocean Model (POP) (Smith and Gent, 2002), has a nominal horizontal resolution of 3.0° and 25 vertical levels. Both experiments use the same vertical and horizontal mixing parameterizations and values. Vertical mixing is represented using the fully implicit kpp mixing parameterization with a background vertical diffusivity of 0.524 cm^2s^{-1}. Horizontal mixing of tracers uses the Gent-McWilliam parameterization, which forces mixing to occur along isopycnals. Horizontal

mixing of momentum uses a parameterization that allows for anisotropic mixing. The sea-ice model, the Community Sea Ice Model (CSIM) (Briegleb et al.,2004*)*, has the same resolution as POP and includes the elastic-viscous-plastic (EVP) scheme.

We have completed two simulations (1xDGVM and 10xDGVM) with mid-Cretaceous paleogeography and paleobathymetry (Scotese, 2001), and a reduced solar constant (99% of present) (Gough, 1981), and modern orbital parameters. The experiments differ only in their atmospheric CO_2 levels, which are prescribed at pre-industrial (1x; 280 ppmv) and ten times pre-industrial (10x; 2800 ppmv) levels.

In our experience using coupled ocean-atmosphere models, the deep ocean reaches equilibrium faster when the ocean is cooling, mainly due to more vigorous convective mixing. Thus, to expedite the convergence to radiative equilibrium, both the 1xDGVM and 10xDGVM experiments were branch runs initialized from a pre-existing 10x Cretaceous experiment. The original 10xDGVM experiment did not include a dynamic vegetation model and was initialized with zonal atmospheric temperatures of 32 °C at the equator and 16 °C at the poles and zonal mean ocean temperatures from a Late Cretaceous simulation (Otto-Bliesner et al., 2002). The 1xDGVM and 10xDGVM simulations were run for 2125 years and 1637 years, respectively. The longer integration time for the 1x experiment in comparison to the 10xDGVM experiment reflects the fact that it was initially furthest from radiative equilibrium.

We assess equilibrium of the simulations by calculating the statistical p-value for the top-of-atmosphere (TOA) radiation and ocean MOC trends. The p-value tests the null

hypothesis that the trend is 0. A p-value >0.1 indicates that the trend is not distinguishable from 0 at the 90% confidence interval. In the 10xDGVM experiment, p-values for years 540-804 are 0.42 and 0.23 for TOA radiation (-0.02 W m^{-2} $century^{-1}$) and MOC (0.1 Sv/century) rates of change, implying quasi-equilibrium. The mean TOA radiation fluxes are 0.08 Wm^{-2} and the MOC flux is 11.6 Sv. In the 1xDGVM experiment, the p-value for TOA radiation fluxes (0.002 W m^{-2} $century^{-1}$) for years 1925-2125 is 0.958.

3.3. Results

3.3.1. Simulation of mean climate

In the 1xDGVM case, the global surface temperature is 14.6 °C (Fig. 3-1a), ~1.0 °C higher than the pre-industrial global surface temperature (Otto-blister et al., 2005). Low-latitude surface temperatures are slightly lower (1-2 °C) than modern as a result of the reduced solar factor and pre-industrial pCO_2. Antarctic surface temperatures are higher due to the absence of an Antarctic ice sheet. Perennial sea-ice covers the Arctic Ocean, the southward limb of the subpolar gyre in the Northern Pacific, and the Antarctic margin (Fig. 3-1a). Deepwaters are formed in both the northern North Pacific and South Pacific Oceans along the Antarctic coast with maximum meridional overturning rates of 20.6 Sv (1 Sv = 10^6 m^3 s^{-1}) and 23.5 Sv respectively (Fig. 3-2a), comparable to present volume fluxes in the North Atlantic (15 ±2 Sv) and Southern Ocean (21 ±6 Sv) (Ganachaud and Wunsch, 2000).

In comparison, the 10xDGVM simulation has a global surface temperature of 23.6 °C. Mean-annual low-latitude sea-surface temperatures range between 28-36 °C, and are consistent with Cretaceous proxy temperatures (e.g. Norris et al., 2002;

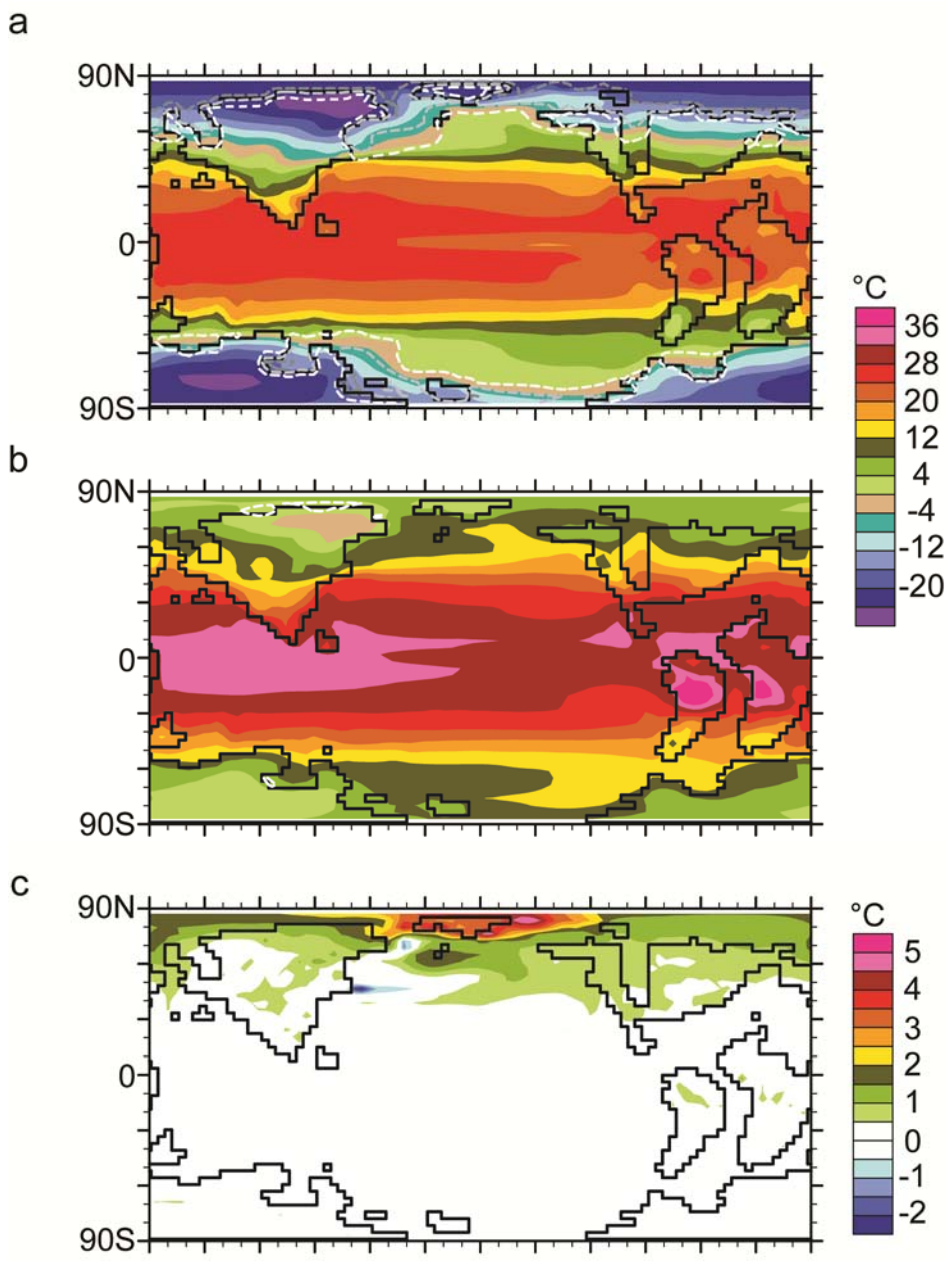

Figure 3-1. Map view of mean annual a) surface temperature (color) and sea-ice fraction (dashed contour lines; 10, 40, and 90%) for the 1xDGVM experiment; b) surface temperature (color) and sea ice fraction (dashed contour lines; 10%) for the 10xDGVM experiment, averaged over years 700-750 (before the abrupt Arctic warming); c) surface temperature anomaly between years 900-950 (after the abrupt Arctic warming) and years 700-750. Units for temperature and sea ice cover are °C and %, respectively.

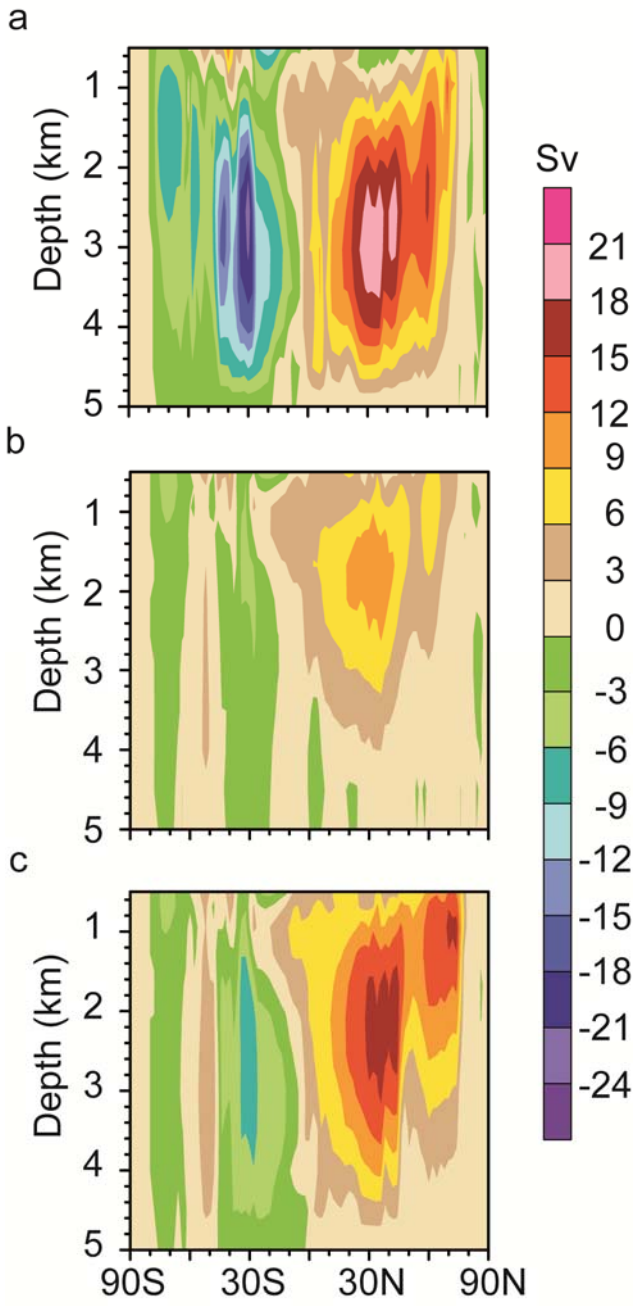

Figure 3-2. Mean annual global MOC for a) the 1xDGVM experiment; b) the 10xDGVM experiment, averaged over years 700-750; c) the 10xDGVM experiment, averaged over years 1550-1600. Unit for MOC is Sv (10^6 m^3 s^{-1}).

Schouten et al., 2003; Wilson et al., 2002). In the high latitudes, only northernmost Siberia has mean-annual surface temperatures below freezing (Fig. 3-1b). As a consequence of CO_2-induced warming, Northern Hemisphere (NH) sea ice is present only in the winter along the northern Siberian coast (>65 °N, 60-165 °E, Fig. 3-1b). Deep waters form mainly in the northern North Pacific and initially have a volume flux of 11.3 Sv (Fig. 3-2b).

3.3.2. Abrupt warming in the 10xDGVM experiment

In year 805 of the 10xDGVM simulation, the Arctic warms abruptly. Surface temperatures increase for approximately 30 years at a rate of 0.53 °C/decade ($P < 10^{-10}$) (Fig. 3-3a). Arctic summer sea-surface temperatures increase from 11.0 °C to 13.0 °C, while the Pacific sector of the Arctic warms more than 4 °C (Fig. 3-1c). Mid-latitude temperatures warm at a rate of 0.10 °C/decade ($P = 0.001$). The new warm-Arctic climate state persists for the remainder of the run (>800 yrs).

The abrupt warming is triggered by anomalous transport of warm, saline subtropical water into the Arctic Ocean. The transport of warmer waters and the breakdown of polar ocean stratification through convective mixing increase the surface heat flux to the atmosphere by 4.8 Wm^{-2} in the Arctic region, and up to 60 Wm^{-2} in the convection zone. The enhanced surface heat flux intensifies the Northern Pacific surface low, and strengthens the polar easterlies and to a lesser extent the mid-latitude Westerlies. The upper-ocean geostrophic response intensifies transport of relatively warm, saline water from the subtropical North Pacific to the polar region through the Bering Strait

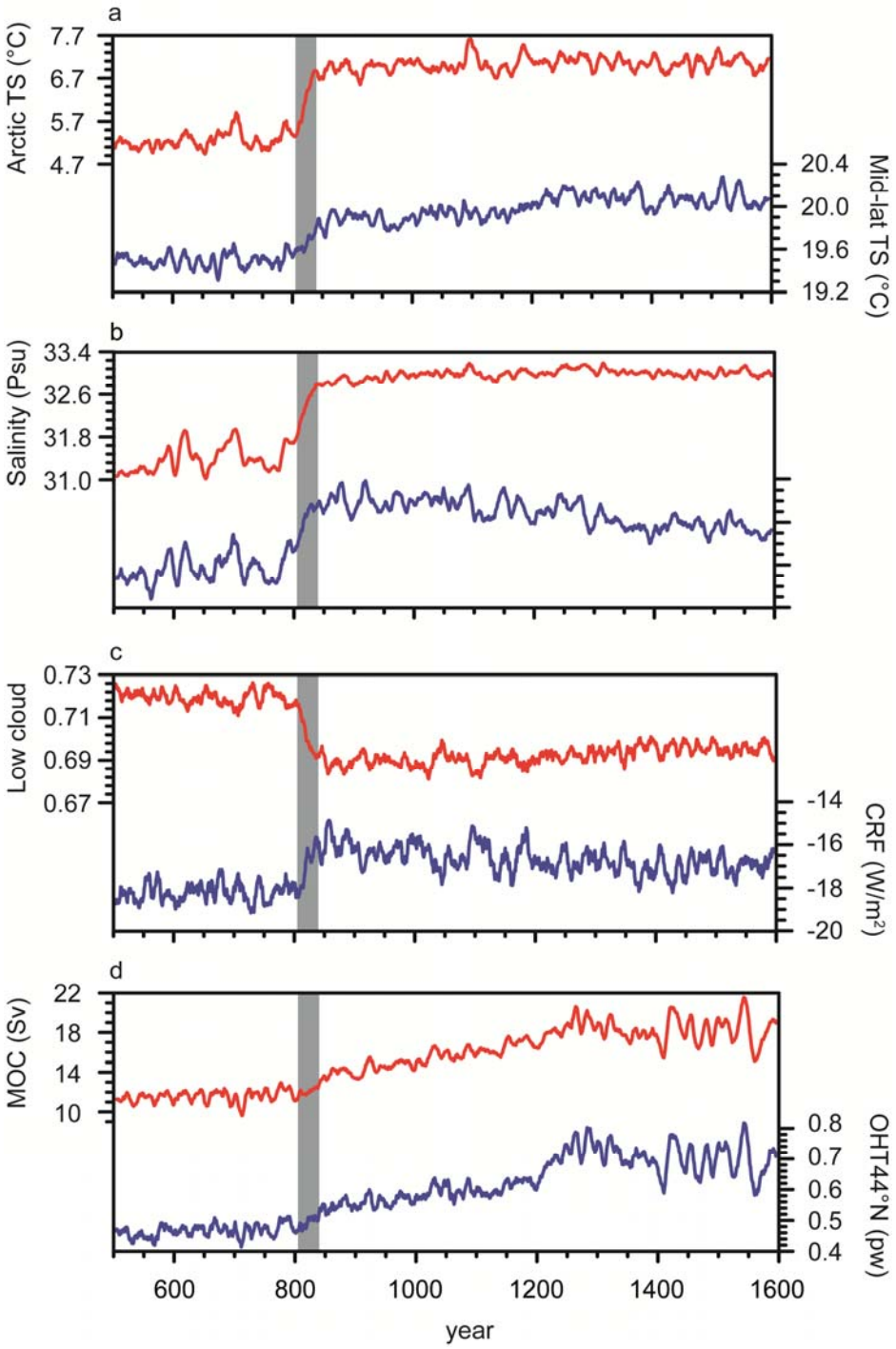

Figure 3-3. Time series for the 10x experiment of a) Arctic (70-90 °N) surface temperature (°C, red) and mid-latitude surface temperature (°C, blue); b) salinity of the North Pacific (psu, red), and oceanic heat transport at 70 °N (PW, blue); c) Arctic (70-90 °N) low-cloud fraction (red), and cloud radiative forcing (Wm^{-2}, blue); d) maximum Northern Hemisphere MOC intensity below 500 m (Sv, red), and oceanic heat transport across 44 °N (PW, blue).

(Fig. 3-4a, b). This positive feedback between surface heating, cyclonic intensification, and subtropical water transport sustains the Arctic warming. Poleward oceanic heat transport (OHT) at 70 °N is significantly correlated with Arctic surface temperature with a lead of six years ($r = 0.79$), confirming the role of ocean heat transport in triggering the abrupt warming event.

Although subtropical water transport into the northern North Pacific triggers the abrupt event, Arctic warming is mainly due to a decrease in low cloud cover (Fig. 3-3c). The increase in poleward OHT at 70 °N is compensated by a decrease in poleward atmospheric heat transport at the same latitude ($r = -0.72$ with a 1 yr lag). However, the increased upward sensible heat flux in the Arctic reduces static stability in the troposphere, destroying the inversion at which low-level stratus clouds form and enhancing atmospheric convection. As a result of the reduction in low clouds, Arctic cloud radiative forcing increases by up to 2.4 Wm^{-2} (Fig. 3-3c) and is positively correlated with Arctic surface temperature ($r = 0.67$ with no lag).

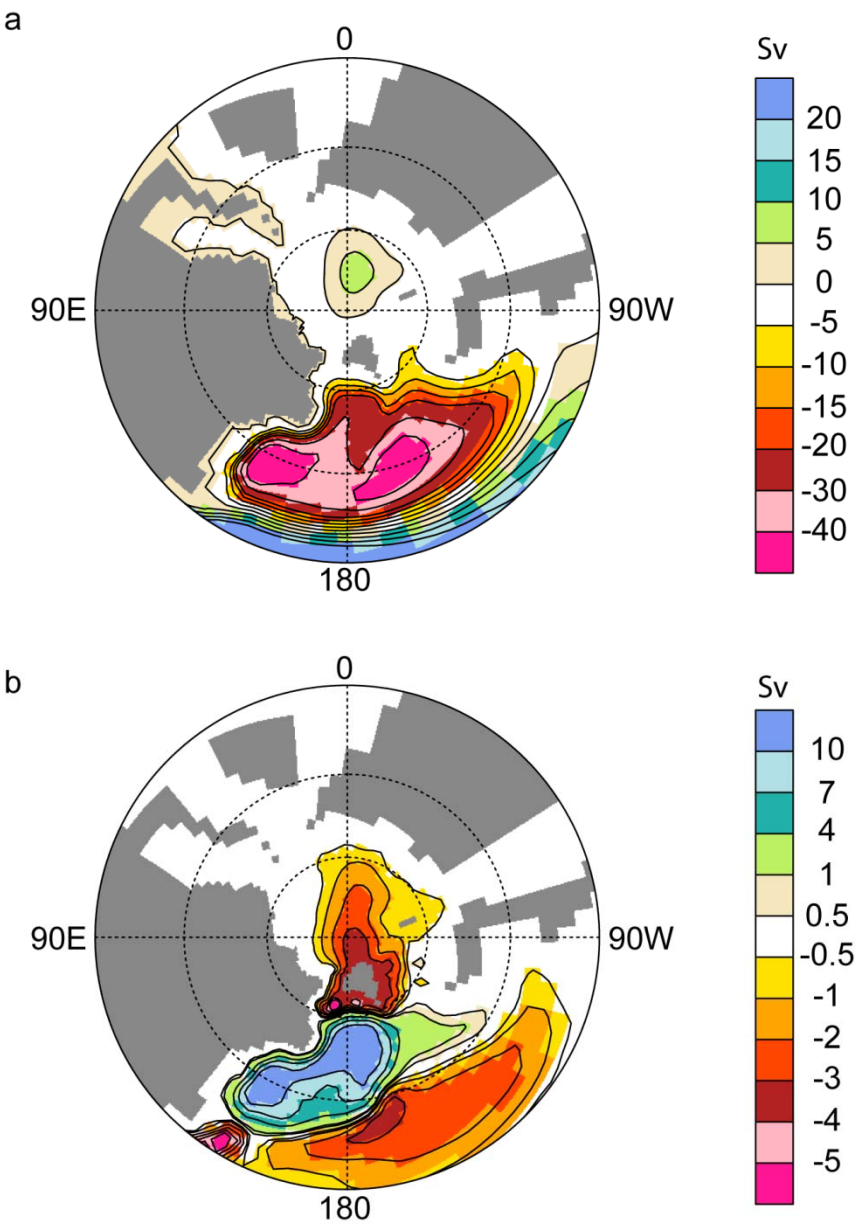

Figure 3-4. a) Mean annual barotropic stream function (Sv) in the 10x experiment a) averaged over model years 700-750; b) difference (Sv) between model years 900-950 and years 700-750. Positive (negative) values indicate anticyclonic (cyclonic) flow. Note that the contour interval is non-uniform in b.

The abrupt Arctic warming event drives a slow intensification of thermohaline circulation (Fig. 3-3d). After year 805, convective mixing in the upper ocean intensifies and migrates northward towards the Arctic Ocean (Fig. 3-5). Between years 805 and 1600, NH MOC increases by 50% (5.6 Sv) and Southern Hemisphere MOC increases by 57% (3.0 Sv) (Fig. 3-2c). The increase in MOC leads to a secondary mid- and high-latitude warming, 0.3 °C between 45-60 °N and 0.5 °C poleward of 60 °S, and slight cooling over the low-latitude oceans. Importantly, MOC intensification is a response, rather than a driver of Arctic climate change (Fig. 3-3a). Arctic surface temperature and NH MOC are modestly correlated ($r = 0.40$) when Arctic surface temperature leads by 7 years.

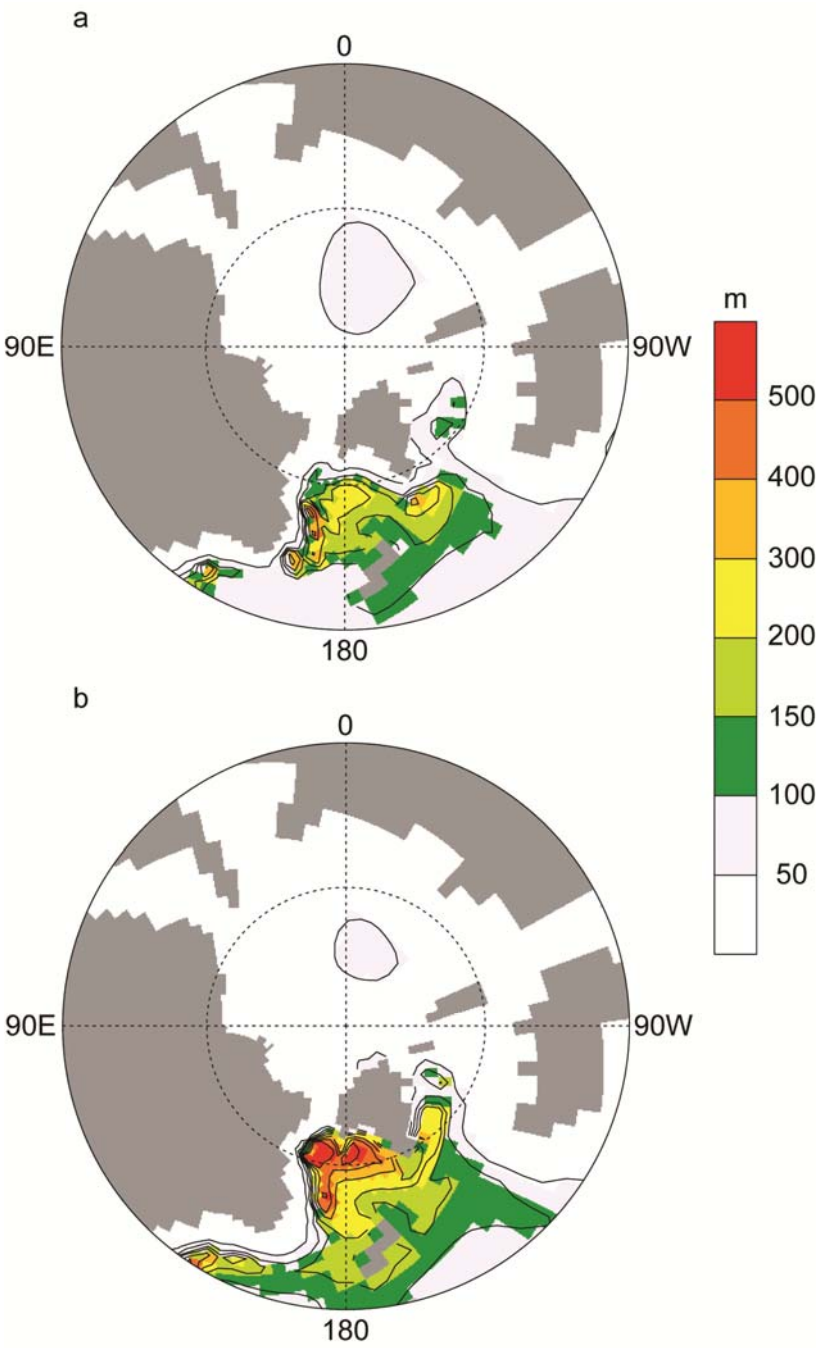

Figure 3-5. Mean annual North Pacific mixed-layer depth in the 10x experiment a) averaged over model years 700-750; b) averaged over model years 900-950. Mixed-layer depth is an indicator of convective mixing, greater depth implies stronger convection. During the abrupt climate event, the convective zone migrates northward and convective mixing reaches greater depths.

3.4. Discussion

The simulation of warm Cretaceous high-latitude conditions is a longstanding problem that has led to the conclusion that climate models are missing or incorrectly representing high-latitude physics in a greenhouse world (Abbot and Tziperman, 2008; Korty et al., 2008; Kump and Pollard, 2008; Poulsen et al., 2007; Sloan and Pollard, 1998). Our 10x experiment demonstrates a polar warming mechanism without any modifications to the existing model physics. A warm-Arctic state is maintained through large poleward OHT and vigorous atmospheric convection, which reduces polar atmospheric stratification and low-cloud coverage. The warm polar state is in better agreement with Cretaceous high-latitude paleo-temperatures; nonetheless, mean-annual surface temperatures (~4 ºC) in the Siberian continental interior remain lower than paleo-temperatures (13.1 ±3.5 ºC) estimated by leaf-margin analyses (Davies et al., 2009). We note, however, that the representation of clouds and convective processes in models is a source of uncertainty and speculate that higher cloud sensitivity, or more vigorous atmospheric convection, might lead to additional polar warming.

Cretaceous oceans experienced episodes of black shale deposition during which regions of the subsurface ocean were anoxic or suboxic (OAEs). To explain OAEs, it has been suspected that the Cretaceous oceans were stratified with low turnover rates during times of high atmospheric pCO_2 (Bralower and Thierstein, 1984). Our model results indicate that multiple overturning states with relatively strong and weak overturning may exist under high atmospheric pCO_2, and that transitions between states can be

geologically instantaneous. This result raises the intriguing possibility that the onset/demise of OAEs could have been triggered through unforced ocean-atmosphere variability.

The Arctic warming event in the 10xDGVM experiment is not completely unprecedented. The two most pronounced warming events in the 20th century (1920s-1940s and post-1979) are associated with intrinsic Arctic ocean-atmosphere-sea-ice variability (Bengtsson et al., 2004; Johannessen et al., 2004; Overland et al., 2008; Polyakov and Johnson, 2000). A reduction in sea ice played a crucial role in these events by facilitating oceanic inflow into the Barents Sea, enhancing surface heat fluxes, and reducing the ice-albedo feedback. Likewise, our 1x experiment, which has perennial and widespread sea-ice cover, exhibits Arctic climate variability and warming events. For instance, during model years 1610-1640, the Arctic warms by 1.6 °C in 13 yrs (Fig. 3-6b). Throughout this multi-decadal event, sea-ice area leads increases in poleward OHT at 70 °N and surface heat fluxes by 1 year.

The return to mean Arctic conditions in the 20th century and in our 1x experiment is linked to an expansion of NH subpolar sea ice (Fig. 3-6a), which acts to insulate the ocean and reduce surface heat fluxes to the atmosphere. In the absence of sea ice, this negative feedback is absent. As a result, in contrast to these decadal events, polar warming in the 10x experiment persists for at least centuries.

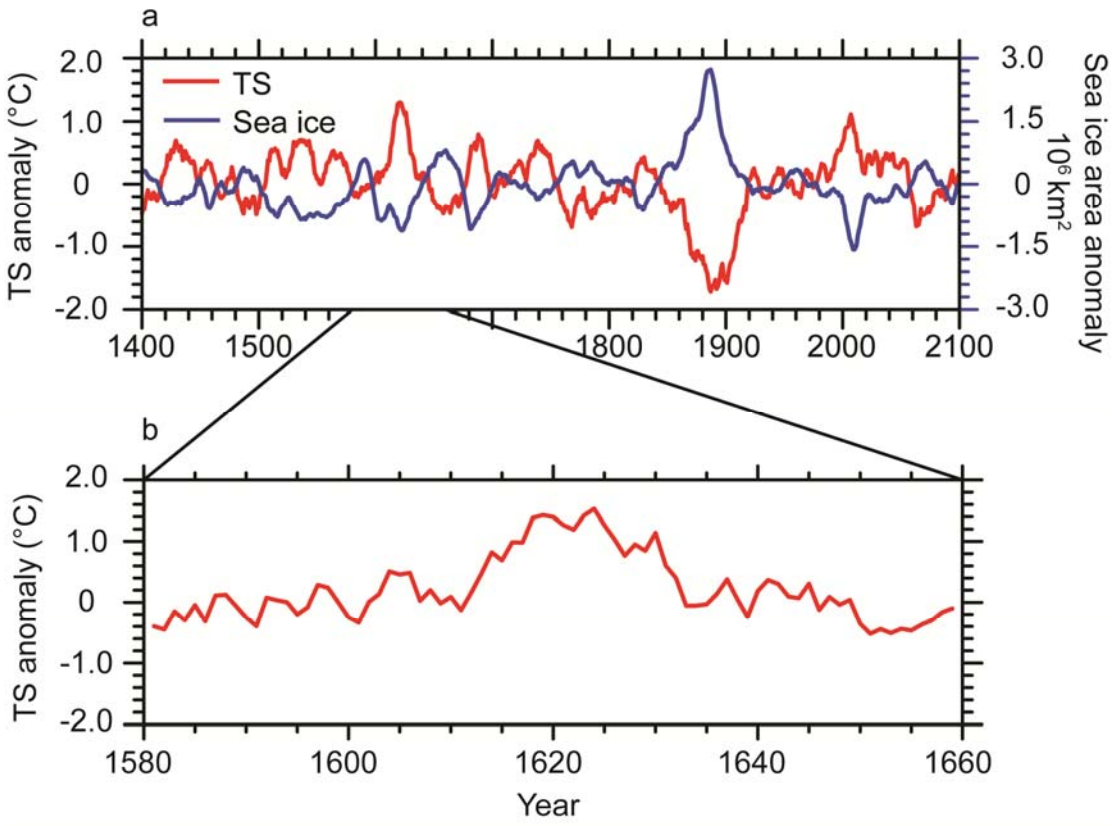

Figure 3-6. Detrended time series of 1xDGVM experiment a) Arctic (70-90 °N) surface temperature anomalies (red), and sea ice area anomalies (blue); b) Arctic surface temperature anomalies between years 1580 and 1660.

The similarity between Arctic climate variability in our 1xDGVM experiment and in the 20th century suggests that there is no *a priori* reason to think that high-latitude climate operated in a fundamentally different way due to differences in geography between the modern and Cretaceous. This leads us to conclude that the hysteresis between cool and warm Arctic states simulated in our 10xDGVM experiment is likely to exist in a future world with less sea ice.

Chapter IV

Simulation of modern and middle Cretaceous marine $\delta^{18}O$ with an ocean-atmosphere GCM

Abstract

We have developed a coupled ocean-atmosphere general circulation model, the GENESIS-MOM model, with the ability to transport and fractionate water isotopes in the ocean and atmosphere. The model is used to predict modern and Cretaceous precipitation and seawater $\delta^{18}O$. The model reproduces the large-scale modern-day isotopic distribution. In the zonal mean, the difference between simulated and observed seawater $\delta^{18}O$ is within 0.2‰ in the low- and mid-latitudes and within 1‰ at high latitudes. In comparison to modern, simulated Cretaceous surface seawater $\delta^{18}O$ is systematically depleted by 0.3‰ at low and middle latitudes. These differences are attributed to equilibrium fractionation during surface evaporation at low latitudes, enhanced low-to-high latitude vapor transport, and an increased partitioning of ^{18}O from the surface into the deep ocean at high latitudes in the Cretaceous. We also find that regional seawater $\delta^{18}O$ is significantly influenced by the paleobathymetry and the resolution of oceanic gateways, boundary conditions that are not well known for the past. Our simulation of Cretaceous seawater $\delta^{18}O$ has implications for oxygen isotope paleothermometry. We conclude that conventional assumptions of past seawater $\delta^{18}O$ may lead to an overestimate of Cretaceous sea-surface temperatures, especially at middle and

high latitudes.

4.1. Introduction

The middle Cretaceous (Albian-Turonian) is considered one of the warmest periods in Earth history. This inference is supported by sedimentological evidence of ice-free polar regions (Jenkyns et al., 2004; Moriya et al., 2007; Price, 1999) and paleo-floral and faunal evidence of tropical species at high latitudes (Huber, 1998; Nathorst, 1911; Spicer and Parrish, 1986; Tarduno et al., 1998), and leaf-margin analyses of fossil leaves (Parrish and Spicer, 1988; Herman and Spicer, 1996). The most direct evidence for warm conditions comes from oxygen isotope paleothermometry, which provides a quantitative estimate of past seawater temperatures. Recent estimates of past seawater temperatures using oxygen isotope paleothermometry are as high as 33-39°C at low latitudes to >14°C at high latitudes (Huber et al., 1995; Norris et al., 2002; Wilson et al., 2002; Bice et al., 2006; Pucéat et al., 2007). However, the extreme polar warmth cannot be resolved by most atmosphere-ocean general circulation models with moderate tropical temperature (Bice et al.,2003; Sloan and Pollard, 1998). These oxygen isotope temperature estimates are dependent on assumptions about the mean isotopic composition of Cretaceous seawater.

The oxygen isotope paleo-thermometer works because natural fractionation processes in seawater are temperature dependent. Due to an equilibrium effect, water molecules with ^{16}O are preferentially evaporated from seawater to produce vapor. Importantly, the equilibriuim fractionation factor decreases with increasing seawater temperature, causing the seawater isotopic composition to become enriched in ^{16}O and

depleted in ^{18}O. The ambient isotopic composition of past seawater is ultimately sampled and preserved through precipitation of marine carbonates, e.g. shells of foraminifera or fish teeth. Though the isotopic composition of marine carbonates ($\delta^{18}O_c$) is often offset from seawater due to biotic effects during carbonate precipitation, laboratory and field experiments have established that the relative isotopic abundance in many species is preserved (e.g., Shackleton, 1974; Erez and Luz, 1983; Kolodny et al., 1983; Bemis et al., 1998).

In addition to $\delta^{18}O_c$, the mean isotopic composition of seawater $\delta^{18}O_w$ must be known to calculate paleo-temperature. $\delta^{18}O_w$ is known for the modern and Holocene and varies regionally (Zachos et al., 1994). The $\delta^{18}O_w$ of earlier periods is not known and is an important source of uncertainty in reconstructing paleotemperature. Cretaceous paleotemperatures have conventionally been estimated using a global mean $\delta^{18}O_w$ of -1.0‰ (SMOW) reflecting the absence of continental ice sheets during this time (Shackleton and Kennett, 1975), even though it is highly improbable that $\delta^{18}O_w$ was uniform across the Cretaceous oceans. Using a uniform $\delta^{18}O_w$ yields paleotemperature estimates that are lower at low latitudes and higher at high latitudes than estimates made using a latitudinally-varying $\delta^{18}O_w$ (Poulsen et al., 1999b). Because a uniform $\delta^{18}O_w$ was unlikely, Cretaceous paleotemperatures are frequently estimated using both global mean Cretaceous seawater and modern local $\delta^{18}O_w$ corrected by -1.0‰ (e.g., Norris et al., 2002; Wilson et al., 2002; Pucéat et al., 2007). However, it is not clear that using modern corrected $\delta^{18}O_w$ is justified, or an improvement over global mean $\delta^{18}O_w$.

To test these assumptions, we have recently developed a coupled ocean-atmosphere general circulation model (GCM) with the capability to transport and fractionate water isotopes in the oceans and atmosphere. This model represents a significant advance over previous climate modeling studies of Cretaceous water isotopes (e.g. Roche et al., 2006; Poulsen et al., 2007b). Here, we describe and discuss our simulations of modern and Cretaceous seawater and precipitation $\delta^{18}O$, and their comparison with modern measured $\delta^{18}O$. Our results show that the distribution of Cretaceous surface $\delta^{18}O_w$ is largely similar to that of the modern. Significant differences occur in the low latitudes, where Cretaceous surface $\delta^{18}O_w$ is slightly lower, and the Arctic Ocean.

4.2. Methods

The experiments presented here were developed using the GENESIS version 3.0 Earth system model coupled to the MOM2 oceanic GCM. GENESIS is comprised of an atmospheric GCM coupled to multilayer models of vegetation, soil and land ice, and snow (Thompson and Pollard, 1997). In comparison to GENESIS version 2.3, the solar and infrared radiation scheme has been replaced with that used in NCAR's CCM3 (Kiehl et al., 1998). Our version of GENESIS also includes water isotopic transport and fractionation in the atmospheric physics (Mathieu et al., 2002). Building on previous isotopic GCM development by Jouzel et al. (1994) and Joussaume and Jouzel (1993), the O^{18}/O^{16} and D/H ratios are predicted in atmospheric vapor, liquid, ice, and soil water reservoirs. Fractionation is modeled as a result of condensation and evaporation in the free atmosphere and from surface waters. Atmospheric ratios are transported using the

same Lagrangian transport as for bulk vapor and clouds. GENESIS-MOM does not currently include a river routing scheme, and continental river runoff is globally averaged and uniformly spread over the world ocean. Such an approximation is appropriate for the Cretaceous where major river drainage basins are not known in detail, and makes the modern simulations consistent with the Cretaceous regarding runoff.

We have previously used GENESIS with isotope capabilities to predict water isotopes in atmospheric vapor (Poulsen et al., 2007a, 2007b). In this study, we add the ability to calculate isotope transport through the ocean by coupling GENESIS to MOM2, a 3-dimensional, z-coordinate ocean GCM with passive-tracer capabilities (Pacanowski, 1995). MOM2 has a horizontal grid spacing of approximately 3.75°, and 20 vertical levels. To ensure conservation of energy and mass, the horizontal grid has been adjusted with a cosine-weighted distortion in order to match the T31 spectral grid used in GENESIS. In our implementation of MOM2, we use an isopycnal mixing scheme (Redi, 1982). Coefficients of horizontal viscosity and diffusion are $2x10^9$ cm^2s^{-1} and $0.5x10^7$ cm^2s^{-1}; coefficients of vertical viscosity and diffusion are 1.0 cm^2s^{-1} and 0.2 cm^2s^{-1}. MOM2 also includes a full convection scheme (Marotzke, J., 1991; Rahmstorf, S., 1993), which removes buoyancy instabilities within a water column. Water isotopes are advected, diffused and convectively mixed as passive tracers within the ocean.

Sea-surface isotopic fluxes due to hydrological processes, including precipitation/evaporation, river runoff, and sea-ice formation/melt, are calculated in GENESIS and then passed to MOM2. As documented in Mathieu et al. (2002), sea ice is treated as a two-layer isotopic reservoir. In the lower layer, the isotopic content of sea ice is estimated from the isotopic composition of seawater with the appropriate isotopic

fractionation. The accumulation of snow on sea ice is tracked in the upper layer. Rain on sea ice is treated as runoff. Surface isotopic fluxes from continental runoff are implicitly estimated to maintain the all-ocean mean isotopic content; this treatment is fully consistent with the global runoff treatment described above.

The GENESIS and MOM models can be fully coupled, exchanging heat, moisture, and momentum fluxes every six hours. However, in order to make long integrations (>5000yrs), we have developed an alternating synchronous-asynchronous coupling technique that works as follows: (i) Fully coupled synchronous segments of 35 years are run, with atmospheric-ocean exchanges performed at each OGCM time step of 6 hours. During the last 10 years of each segment, monthly mean near-surface meteorology (air temperature, humidity, winds, downward solar and infrared radiative fluxes, precipitation, and the isotopic fractionation of precipitation and evaporation) were stored as 10-year averages. (ii) Following each synchronous segment, the saved fluxes are then used to drive the OGCM alone through the next asynchronous segment of 500-2000 years, with ocean surface fluxes calculated by the AGCM's (LSX) boundary layer routine using the previously saved atmospheric conditions and the current OGCM sea-surface temperatures. (Sea ice is considered part of the AGCM, and where sea ice exists in the synchronous segments, all saved "surface meteorological" quantities are those at the sea-ice base.) (iii) A final 35 yr fully coupled synchronous segment is completed to produce data for analyses.

Modern and Cretaceous simulations were integrated through at least 4 asynchronous-asynchronous segments, representing integration durations of more than 6000 years. After these long integrations, the ocean is very close to equilibrium. Global

average temperature trends are 0.015 °C/1000 yrs and -0.05 °C/1000 yrs for Cretaceous and modern experiments, respectively. In the upper ocean (top 25m), seawater temperature trends are 0.08 °C/1000 yrs and 0.01 °C/1000 yrs, respectively. In addition, $\delta^{18}O$ is well conserved in all experiments. Global average ocean $\delta^{18}O$ is -1.0 and -0.0‰ (SMOW) for the Cretaceous and modern experiments, identical to the initial values of -1.0 and -0.0‰ (SMOW).

Four climate-isotope experiments were completed in this study (Table 4-1). Two modern experiments were completed with modern geography, ocean bathymetry and atmospheric pCO_2. The modern experiments differ only in their resolution of the Bering Strait. On the T31 grid, the Bering Strait is too narrow to be fully resolved. As a result, in the first experiment (MOD), the Bering Strait is not represented; i.e., there is no ocean connection between the North Pacific and Arctic Oceans. To evaluate the influence of this ocean connection on high-latitude seawater $\delta^{18}O$, a second experiment (MOD-Bering) was conducted in which the bathymetry has been modified to include a Bering Strait connecting the North Pacific and Arctic Oceans. Though the model representation of the strait is narrow (3 grid cells in width), it nonetheless exaggerates the width of the modern strait.

Table 4-1. Model parameters and global average sea-surface temperature (ºC), precipitation (mm day^{-1}), $\delta^{18}O$ of surface seawater and precipitation (‰) (SMOW).

Exp.	Description	pCO_2 (ppm)	SST	Precip.	Precip. $\delta^{18}O$	Seawater $\delta^{18}O$
MOD	Modern geography and bathymetry but with no Bering Strait.	355	18.4	3.0	-7.1	0.0
MOD-Bering	Modern geography and bathymetry with Bering Strait resolved.	355	18.2	3.0	-7.1	0.0
K-Flat	Cenomanian geography and topography; ocean bathymetry is uniformly 5600m	2240	23.0	3.5	-6.1	-1.0
K-Bathy	Cenomanian geography and topography; ocean bathymetry is based on PALEOMAP project reconstruction*	2240	23.0	3.5	-6.2	-1.0

*Ocean bathymetry of K-Bathy experiment is based on reconstructions from the PALEOMAP project (http://www.scotese.com/)

Note: $\delta^{18}O$ of seawater is not corrected as stated in the methods part, to show the initial ocean $\delta^{18}O$ difference.

Two Cretaceous experiments were also completed with Cretaceous geography and topography representing Cenomanian lowstand conditions (as in Poulsen et al., 2007b). Middle Cretaceous atmospheric pCO_2 likely ranged between 2 and 16x pr-industrial levels (Bice et al., 2006); in this study we used a median Cretaceous pCO_2 value of 2240 ppmv, 8x pre-industrial levels. In the first Cretaceous experiment (K-flat), the ocean bathymetry is uniformly 5600m. In the second Cretaceous experiment (K-bathy), we included Cretaceous paleo-bathymetry based on reconstructions from the PALEOMAP project (http://www.scotese.com/). Ocean $\delta^{18}O_w$ was initialized to 0.0‰ in the modern experiments and -1.0‰ (SMOW) in the Cretaceous experiments to reflect the absence of major ice sheets at that time (Shackleton and Kennett, 1975). However, unless otherwise noted, we refer to and show "corrected" $\delta^{18}O$, which is the simulated Cretaceous $\delta^{18}O$ plus 1.0‰ (SMOW) to compensate for differences between modern and Cretaceous mean seawater $\delta^{18}O$, to facilitate comparison with the modern experiments. All analyses were made with the last ten years of climate data from the final 35 yr coupled iteration.

4.3. Results

4.3.1. Simulation of modern $\delta^{18}O$

GENESIS has previously been shown to simulate the large-scale modern surface $\delta^{18}O$ distribution including east-west gradients due to continental and altitudinal effects, seasonal variations, and the zonal profile except over Antarctica (Mathieu et al., 2002). Because our coupling of GENESIS 3.0 with MOM2 is a major revision, in this section we compare our simulated isotope composition of precipitation ($\delta^{18}O_p$) and surface seawater ($\delta^{18}O_w$) with modern observational data sets from Rozanski et al. (1993) and

LeGrande and Schmidt (2006), which was based on the Schmidt et al. (1999) online database of $\delta^{18}O$ and salinity measurements.

In the zonal mean, modeled precipitation $\delta^{18}O_p$ agrees well with IAEA/WMO data (Rozanski et al., 1993) where data coverage is relatively dense. As shown in Fig. 4-1, the 2σ uncertainty of zonally-averaged $\delta^{18}O_p$ encloses nearly all the observed data. Since observational data is sparse or nonexistent in southern high latitudes, it is impossible to evaluate the model's performance in this region.

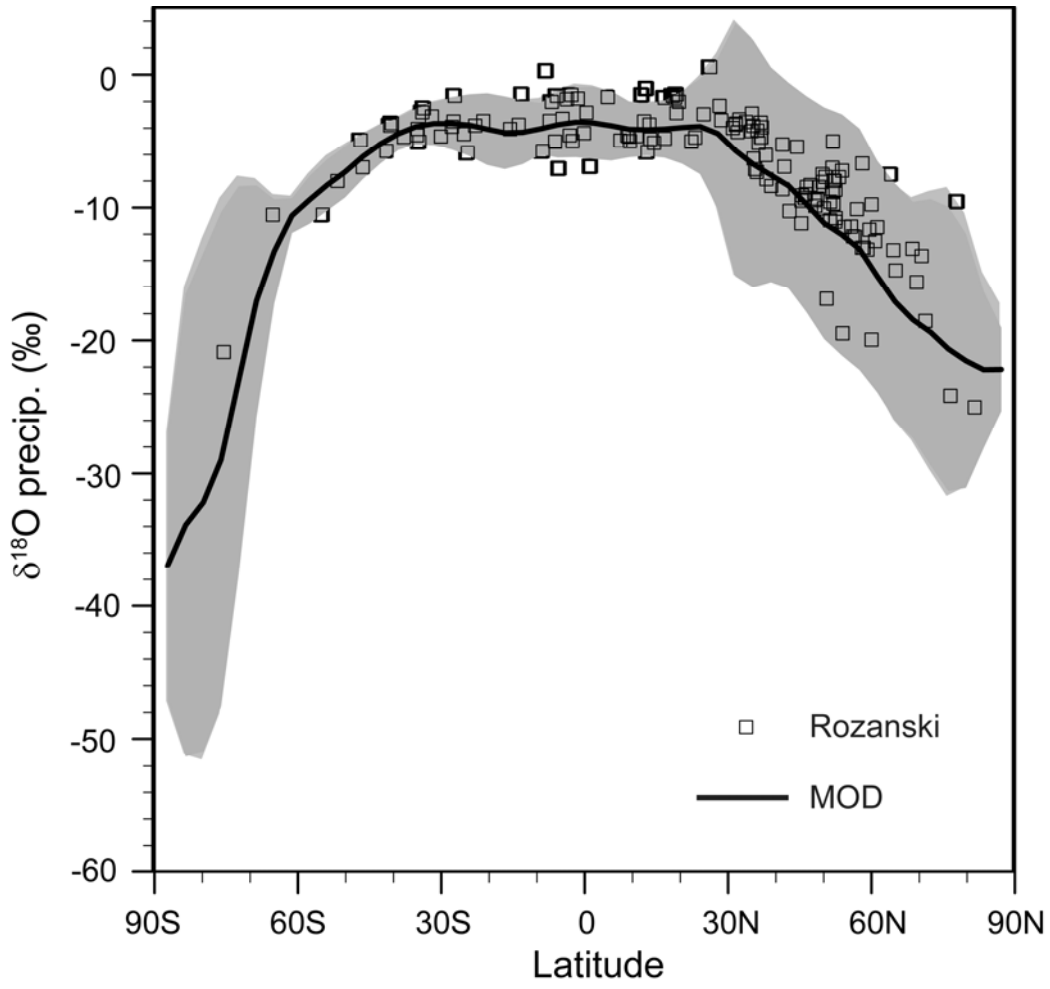

Figure 4-1. Mean annual zonal average $\delta^{18}O_p$ (SMOW) of precipitation predicted in our MOD experiment and from IAEA/WMO data (Rozanski et al., 1993). The shaded area is 2σ confidence interval of simulated zonally-averaged $\delta^{18}O_p$.

The annual average surface seawater $\delta^{18}O_w$ captures most large-scale features in the LeGrande and Schmidt (2006) data set (compare Figs. 4-2a and 4-2b). The model predicts enriched surface seawater $\delta^{18}O$ in the subtropical oceans (especially in the Atlantic), and depleted surface seawater $\delta^{18}O$ in the Arctic and Southern Oceans. Surface seawater $\delta^{18}O_w$ differences between our MOD experiment and observation are generally within 0.5‰ except in the Arctic Ocean. In the zonal mean, the average surface seawater $\delta^{18}O_w$ in MOD experiment is within 2σ error range of the averaged $\delta^{18}O_w$ from LeGrande and Schmidt (2006) at low and middle latitudes (Fig. 4-3a) At high latitudes, simulated $\delta^{18}O_w$ is depleted by up to 1‰ in the Southern Ocean and 11‰ in the Arctic Ocean. These large differences in the Arctic are due to the absence of a Bering Strait and connections between western and eastern Arctic Ocean. Without these gateways, no mixing occurs between the Arctic and Pacific Oceans. Consequently, Arctic $\delta^{18}O_w$ is driven to low values approaching those of the high-latitude continental runoff. In the MOD-Bering experiment, in which the Bering Strait has been opened and widened, the $\delta^{18}O_w$ difference between the model and observations in the Arctic is less than 2‰ (Fig. 4-3a). In the Southern Ocean, the observed surface seawater $\delta^{18}O_w$ is derived from empirical $\delta^{18}O$-salinity relationships. The coefficient of determination (R^2) between $\delta^{18}O$ and salinity is 0.374, suggesting the Southern Ocean surface seawater $\delta^{18}O_w$ is not well characterized (LeGrande and Schmidt, 2006). At this point, it is impossible to determine whether model errors or observational uncertainties are chiefly responsible for the 1‰ discrepancy.

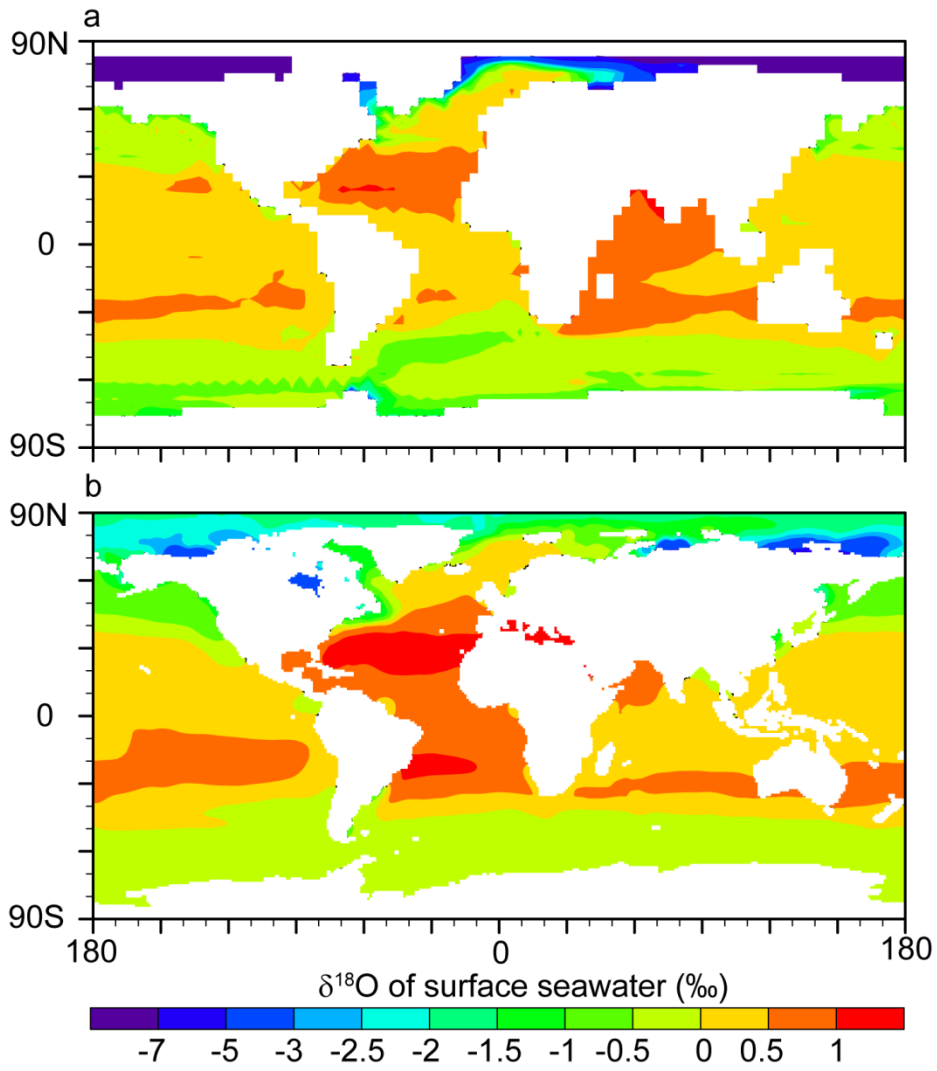

Figure 4-2. Mean annual $\delta^{18}O_w$ (SMOW) spatial distribution of modern surface seawater predicted in our MOD experiment (a), and interpolated from global gridded empirical data (LeGrande and Schmidt, 2006) (b). Continental regions are shaded in grey.

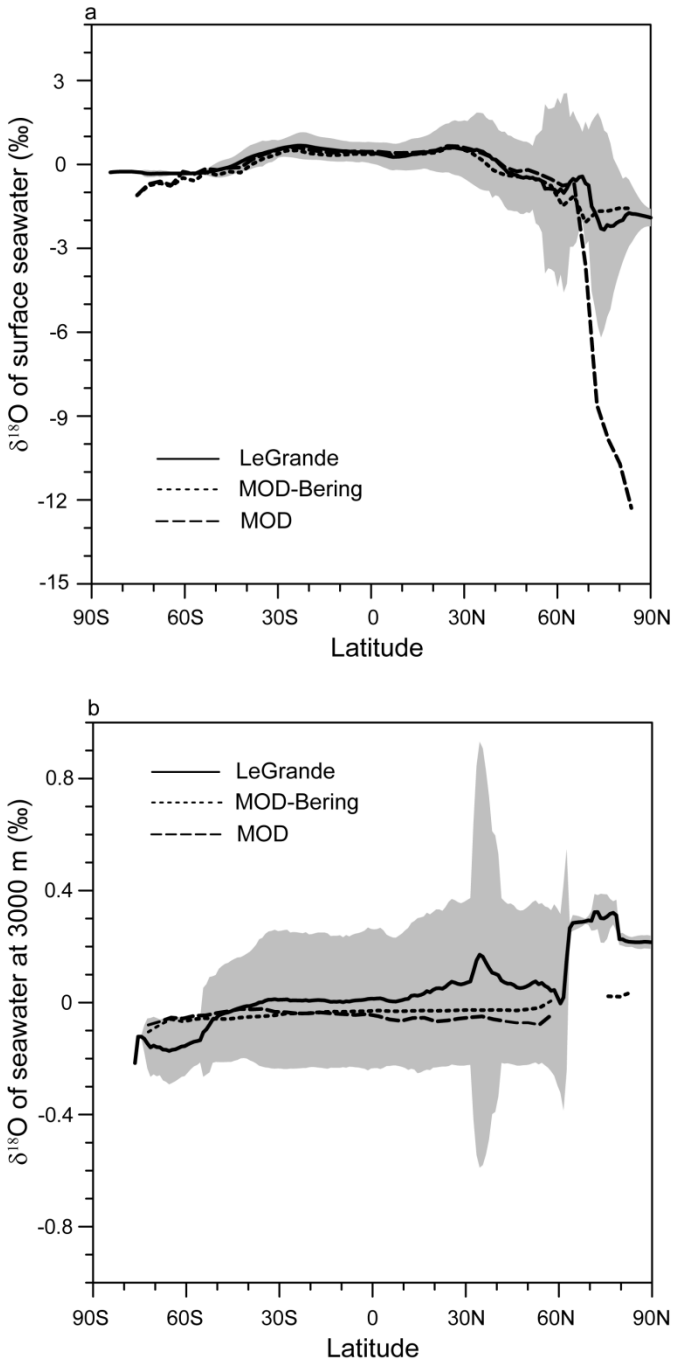

Figure 4-3. Mean annual zonal average $\delta^{18}O_w$ (SMOW) of modern surface seawater (A); and modern deep water at 3000 m (B) predicted in our MOD (medium dashed line) and MOD-Bering (short dashed line) experiments and from LeGrande and Schmidt (2006) (solid line). The shaded area is the 2σ confidence interval of zonally-averaged $\delta^{18}O_w$ from LeGrande and Schmidt (2006) and represent spatial variability due to zonal heterogeneity in $\delta^{18}O_w$. Note that the MOD experiment has Arctic seawater $\delta^{18}O_w$ of -12‰ (see discussion in text). This low value is outside of the range shown in the figure.

The simulation of deep-water $\delta^{18}O$ also compares well with observations. Seawater $\delta^{18}O$ at 3000m is within 2σ of the LeGrande and Schmidt (2006) $\delta^{18}O_w$ except in the Arctic (Fig. 4-3b). As described above, the differences in the Arctic region are attributed to insufficient mixing between the Arctic Ocean and Atlantic and Pacific Oceans. In sum, GENESIS-MOM reproduces modern observed seawater $\delta^{18}O_w$ in most regions where a meaningful comparison is possible.

4.3.2. Simulation of Cretaceous climate and precipitation $\delta^{18}O_p$

As a result of higher CO_2 in our Cretaceous experiments, simulated surface temperature and precipitation rate are higher than present, consistent with previous Cretaceous simulations (e.g. Barron et al., 1989; Donnadieu et al., 2006; Poulsen et al., 1999a, 2003, 2007b). The global mean-annual Cretaceous sea-surface temperature is 23.0 ºC, approximately 4.6 °C higher than that in the MOD simulation (Table 4-1 and Fig. 4-4). The global precipitation rate is 3.5 mm day^{-1}, about 0.5 mm day^{-1} higher than those simulated in the MOD experiment (Table 4-1).

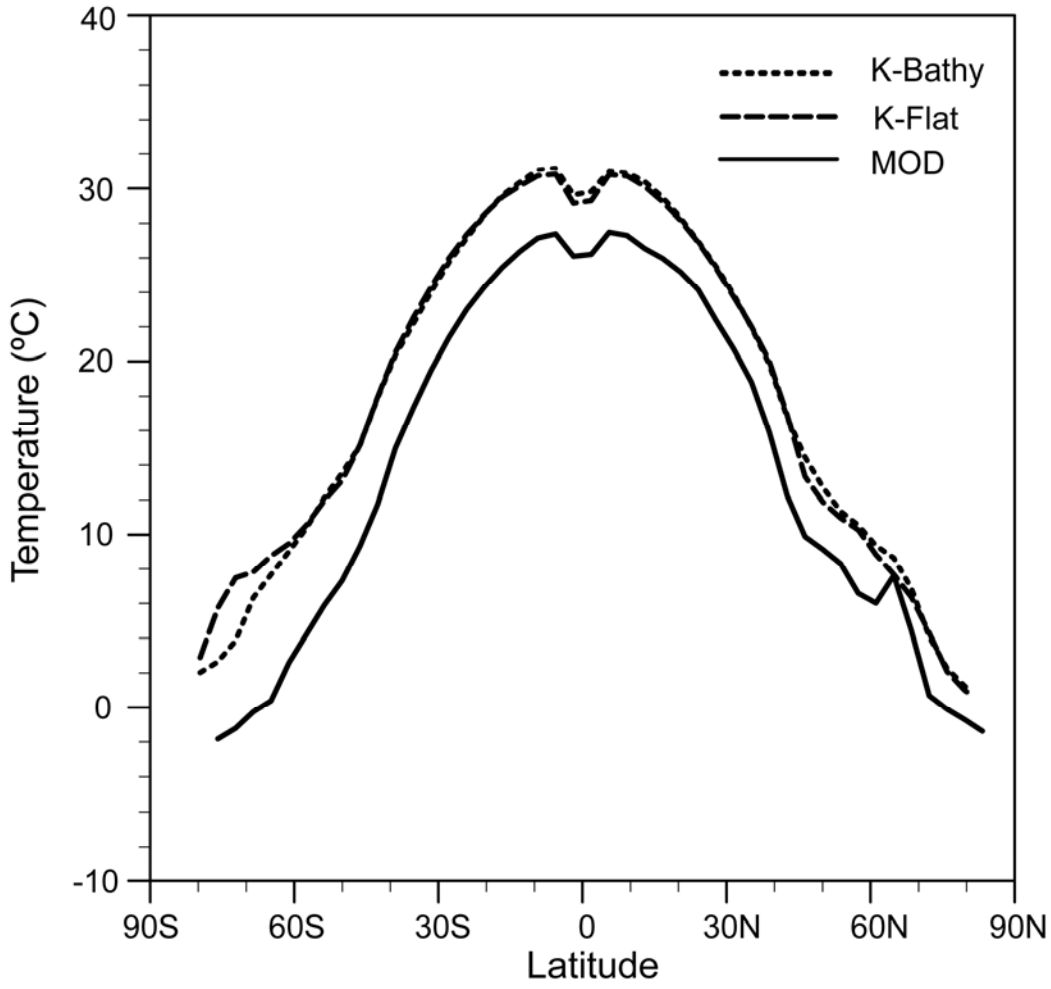

Figure 4-4. Mean annual zonal average sea-surface temperature in MOD (solid line), K-Flat (medium dashed line) and K-Bathy (short dashed line) experiments.

Cretaceous precipitation $\delta^{18}O_p$ ranges from -3.5‰ in subtropical areas to -20.8‰ (K-flat) and -20.4‰ (K-Bathy) in the Antarctica regions (Fig. 4-5). Cretaceous $\delta^{18}O_p$ in tropical and subtropical areas is practically identical to MOD. However, Cretaceous $\delta^{18}O_p$ is up to 16‰ and 5‰ greater than MOD in the southern high latitudes and Arctic region, respectively. Several factors are responsible for the enrichment of Cretaceous high-latitude precipitation including: (1) reduced equilibrium fractionation due to higher polar temperatures, (2) reduced altitudinal fractionation in the Southern Hemisphere due to the absence of a tall Antarctic ice sheet, and (to a smaller degree) (3) a source of relatively high $\delta^{18}O$ vapor from a seasonally ice-free Arctic Ocean.

Precipitation $\delta^{18}O_p$ is indistinguishable between the K-Flat and K-Bathy experiments except at northern high latitudes where the difference is ~1.4‰ (Fig. 4-5). Because surface temperature and precipitation rate are nearly identical in these experiments, northern high-latitude precipitation $\delta^{18}O_p$ differences are likely due to differences in the isotopic concentration of the Arctic Ocean, which is seasonally ice-free and serves as an important regional vapor source. In the K-Flat experiment, Arctic seawater $\delta^{18}O_w$ is 4.4‰ greater than in the K-Bathy experiment due to enhanced seawater exchange between the Pacific and Arctic basins (see below), leading to greater precipitation $\delta^{18}O_p$.

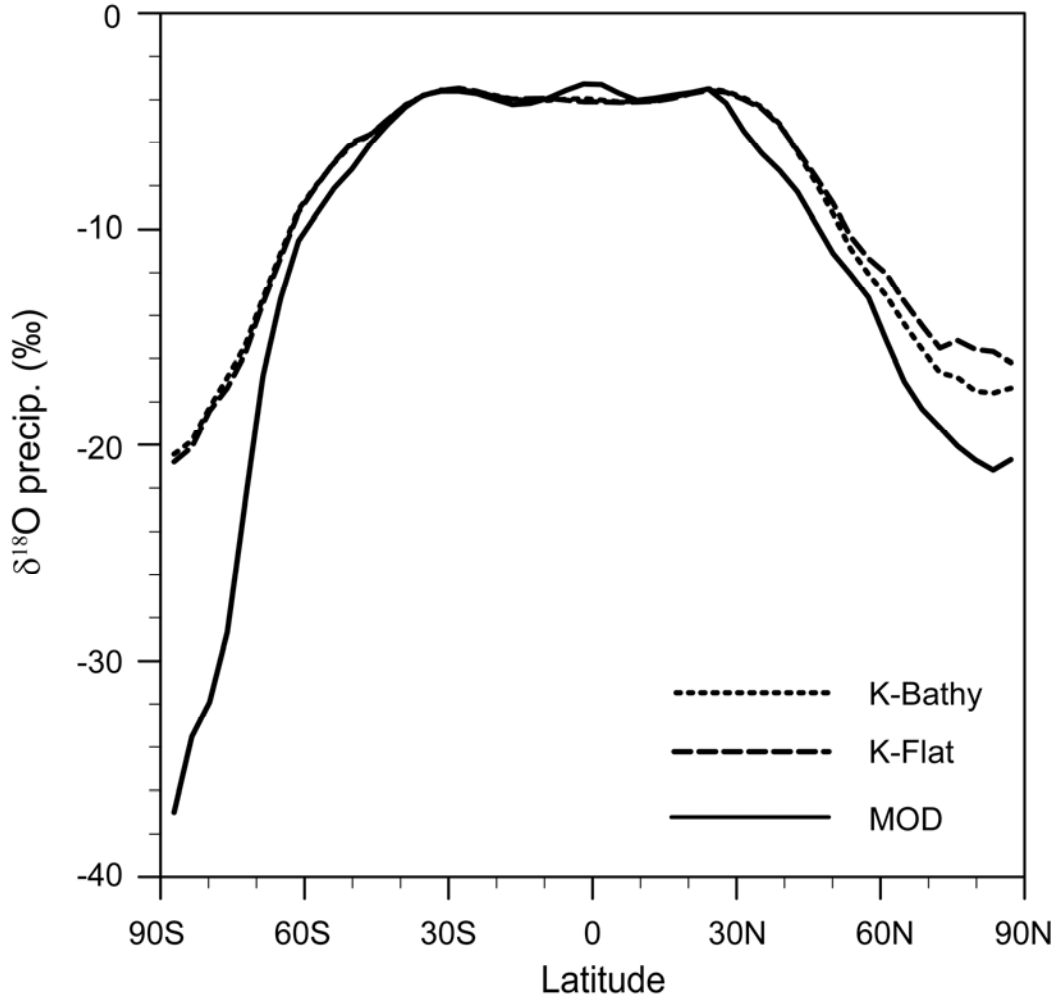

Figure 4-5. Mean annual zonal average precipitation $\delta^{18}O_p$ (SMOW) in MOD (solid line), K-Flat (medium dashed line) and K-Bathy (short dashed line) experiments. Note that "corrected" Cretaceous $\delta^{18}O$ is shown. As described in the Methodology (section 2), 1.0‰ (SMOW) has been added to the simulated Cretaceous $\delta^{18}O$ to facilitate comparison with the modern simulation.

4.3.3. Simulation of Cretaceous surface seawater $\delta^{18}O_w$

The large-scale surface seawater $\delta^{18}O_w$ in the Cretaceous experiments is similar to the modern simulation. As in the MOD experiment, Cretaceous $\delta^{18}O_w$ is depleted in high latitudes and enriched in the subtropical oceans (Fig. 4-6a and 4-6b). In the zonal mean, the Cretaceous surface seawater $\delta^{18}O_w$ distribution pattern is similar to modern in most areas, ranging from 0.3‰ in the subtropical oceans to -4.2‰ (K-Flat) and -8.6‰ (K-Bathy) in the Arctic (Fig. 4-7). Cretaceous surface seawater $\delta^{18}O_w$ is ~0.3‰ lighter than modern in tropical and subtropical regions. The $\delta^{18}O_w$ difference is even smaller at the southern mid-to-high latitudes, which is ~0.1‰. In the Arctic Ocean, however, Cretaceous $\delta^{18}O_w$ is up to 8.1‰ (K-Flat) and 4.2‰ (K-Bathy) greater than that in the MOD experiment, but as much as 2.6‰ (K-Flat) and 7.0‰ (K-Bathy) lower than that in the MOD-Bering experiment. As discussed in 4.3.1, these differences between Cretaceous and modern Arctic $\delta^{18}O_w$ are due primarily to ocean mixing rates between the Arctic and Pacific Oceans. Similarly, differences in Arctic $\delta^{18}O_w$ between the Cretaceous simulations are also attributed to differences in Arctic-Pacific mixing rates. In the K-Flat experiment, with a deep (5600m) paleo-Bering Strait and greater seawater exchange between the Pacific and Arctic, Arctic Ocean $\delta^{18}O_w$ is 4.4‰ higher than in the K-Bathy experiment with a shallow (144m) strait and reduced seawater exchange.

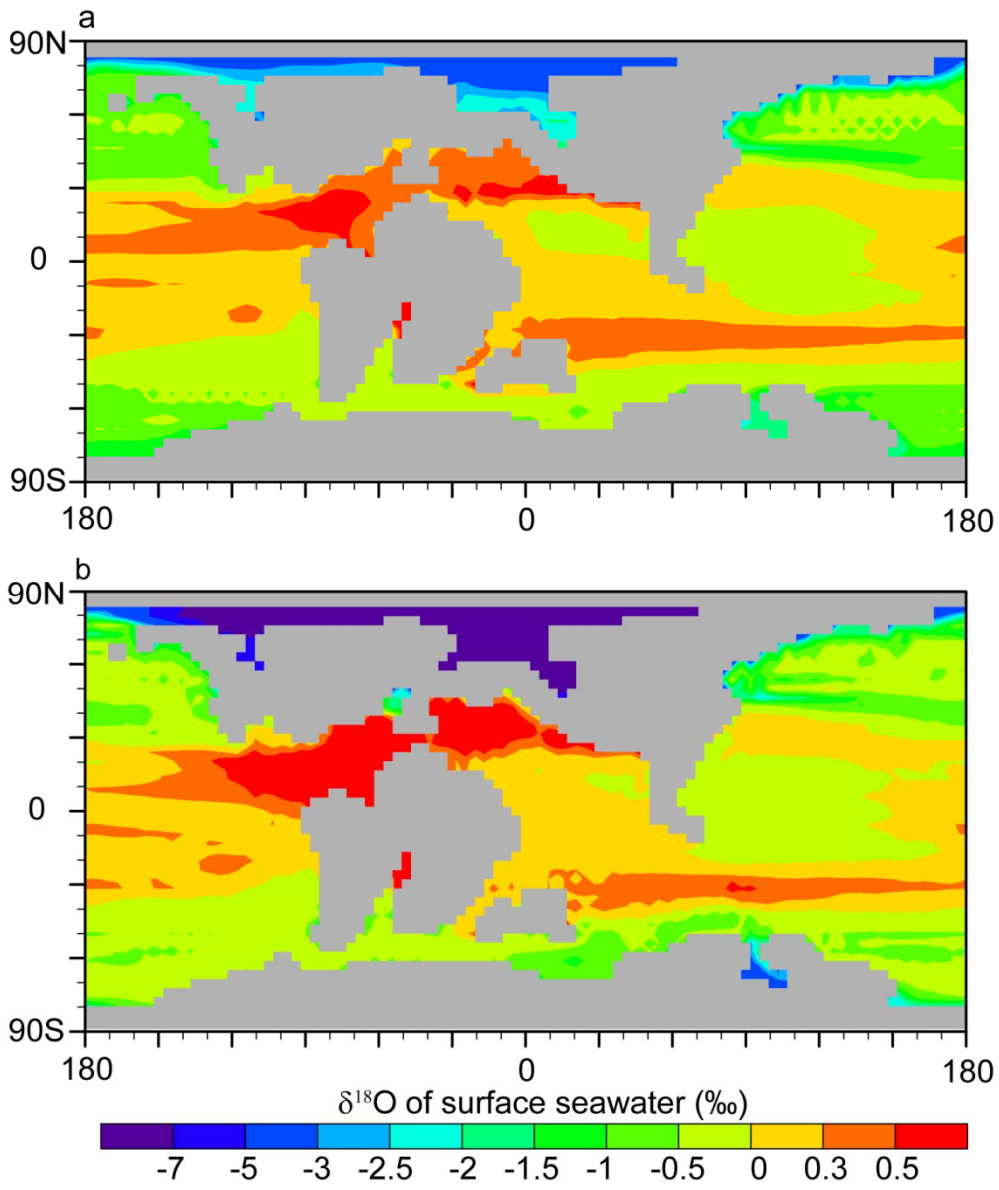

Figure 4-6. Mean annual $\delta^{18}O_w$ (SMOW) spatial distribution of Cretaceous surface seawater predicted for the K-Flat experiment (a), and K-Bathy experiment (b). Continental regions are shaded in grey. Note that "corrected" Cretaceous $\delta^{18}O$ is shown (see caption in Fig. 4-5).

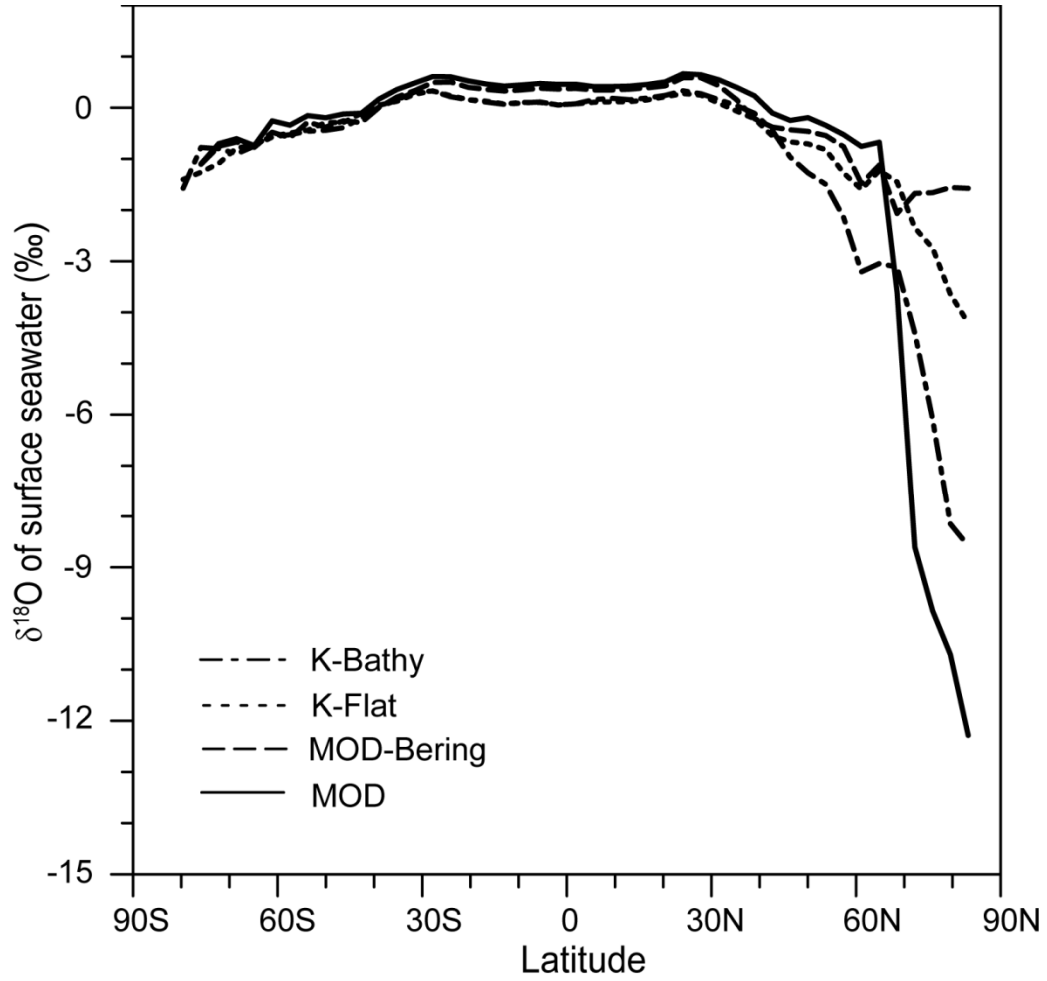

Figure 4-7. Mean annual zonal average $\delta^{18}O_w$ (SMOW) of surface seawater in MOD (solid line), MOD-Bering (medium dashed line), K-Flat (short dashed line) and K-Bathy (dash-dot line) experiments. Note that "corrected" Cretaceous $\delta^{18}O$ is shown (see caption in Fig. 4-5).

4.3.4. Simulation of Cretaceous subsurface seawater $\delta^{18}O_w$

In the most general sense, simulated Cretaceous subsurface seawater $\delta^{18}O_w$ is similar to modern. In both modern and Cretaceous experiments, the upper ocean (~150-1000 m) is more enriched in ^{18}O than the lower ocean (>1000 m), reflecting the preference for intermediate and deep water formation at high latitude sites with relatively low $\delta^{18}O_w$. Moreover, at depths greater than 500 m, mean Cretaceous subsurface $\delta^{18}O_w$ is within 0.1‰ of modern (Fig. 4-8).

Though generally similar, there are meaningful differences between the modern and Cretaceous subsurface $\delta^{18}O_w$. In comparison to the modern, Cretaceous subsurface $\delta^{18}O_w$ is lower in the upper ocean and higher in the deep ocean (Fig. 4-8). These differences result from the sites of intermediate- and deep-water formation. In both Cretaceous experiments, subtropical waters from the Tethys and proto-South Atlantic regions contribute significantly to the overall intermediate and deep water volumes. In the upper ocean (Fig. 4-9a), saline, ^{18}O-enriched seawater originates from the Tethys and flows through the equatorial Pacific Ocean. This watermass is constrained to ~1400 m. At greater depths (Fig. 4-9b), the North Pacific region provides the primary source of ^{18}O-enriched seawater. However, because North Pacific surface $\delta^{18}O_w$ is relatively depleted (Fig. 4-6a), it cannot be the sole source of this water. Rather, warm, saline, ^{18}O-enriched seawater from Tethys flows into the North Pacific, mixes with colder North Pacific water, and sinks to form this water mass. Finally, at the greatest depths (Fig. 4-9c), the proto-South Atlantic is a significant source of saline, ^{18}O-enriched seawater. Above, we have

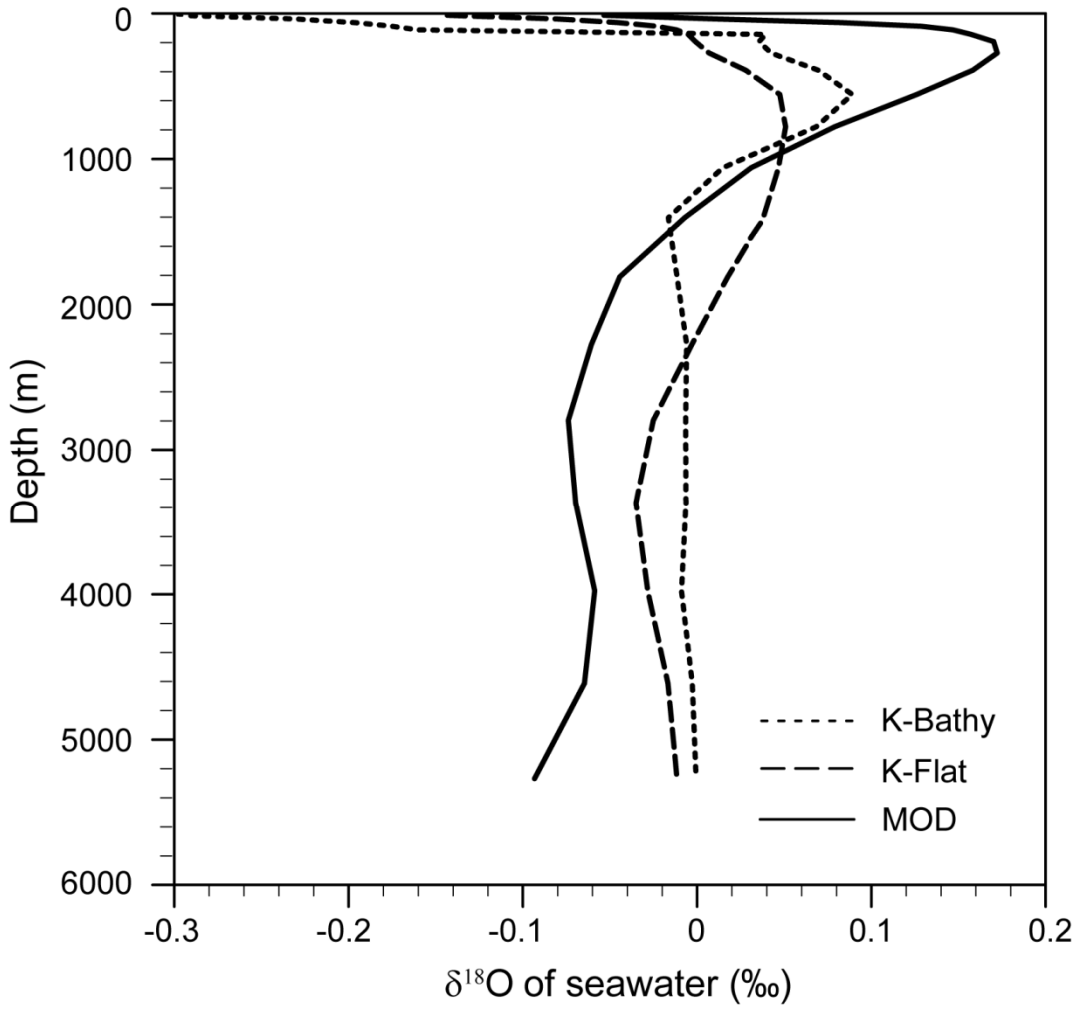

Figure 4-8. Vertical distribution of global mean seawater $\delta^{18}O_w$ (SMOW) in the modern and Cretaceous simulations. Cretaceous $\delta^{18}O_w$ is lesser above ~1000m and greater below ~1000m than modern due to differences in the isotopic composition of intermediate and deep water sources. Note that "corrected" Cretaceous $\delta^{18}O$ is shown (see caption in Fig. 4-5).

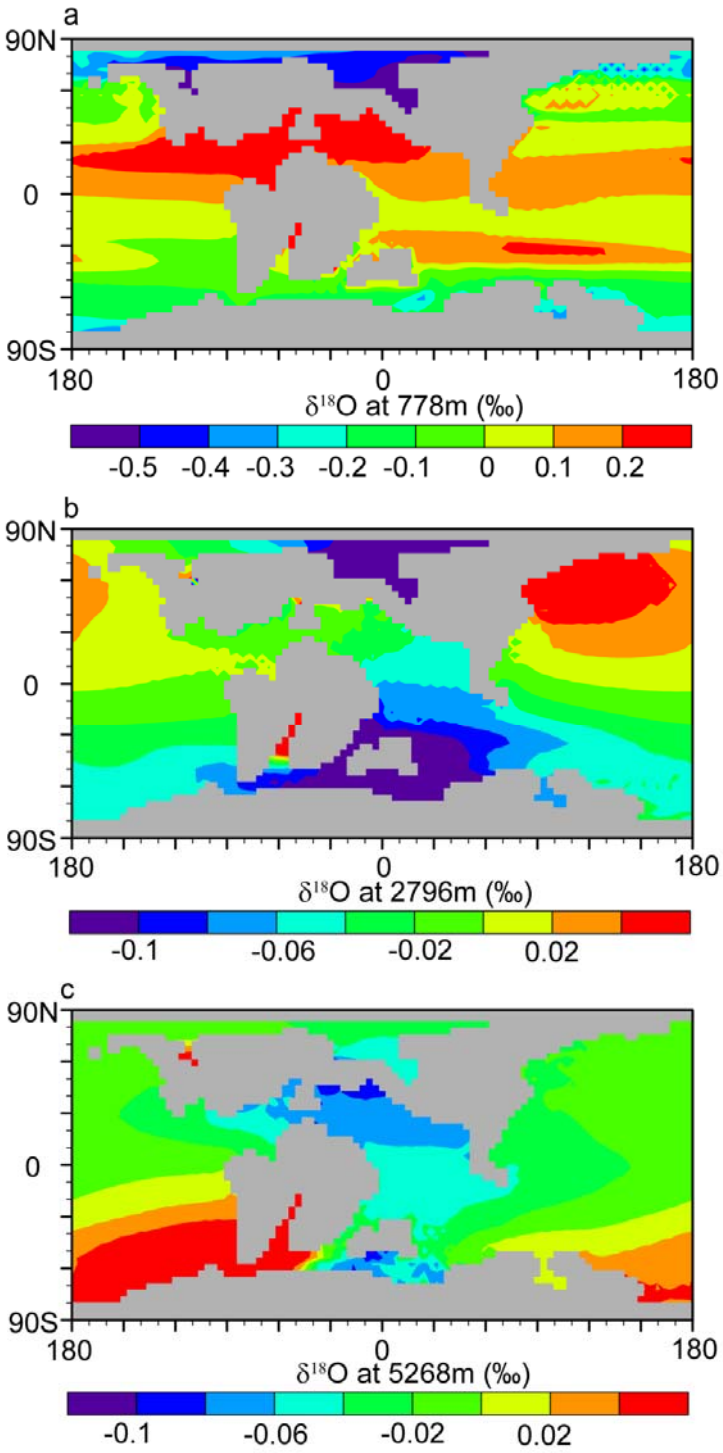

Figure 4-9. Mean annual $\delta^{18}O_w$ (SMOW) spatial distribution of Cretaceous seawater in K-Flat experiment at depth of 778 m (A); at depth of 2796 m (B); and at depth of 5268 m (C). Continental regions are shaded in grey. The mean annual $\delta^{18}O_w$ distribution for the K-Bathy experiment is similar. Note that "corrected" Cretaceous $\delta^{18}O$ is shown (see caption in Fig. 4-5).

focused on the sources of relatively ^{18}O-enriched seawater. However, in both Cretaceous experiments, high latitude regions around Antarctica are also important sites of intermediate- and deep-water formation (Figs. 4-9 b,c).

4.4. Discussion

4.4.1. Simulation of Cretaceous surface seawater $\delta^{18}O_w$

To our knowledge, this study is the first to simulate Cretaceous seawater $\delta^{18}O_w$ using a coupled atmosphere-ocean GCM with isotopic capabilities. Poulsen et al. (2007b) used an atmosphere-only model to demonstrate that high atmospheric pCO_2 causes a systematic, moderate (<3‰) increase in Cretaceous precipitation $\delta^{18}O_p$ resulting from reduced equilibrium fractionation due to higher surface temperatures. Although precipitation $\delta^{18}O_p$ can be strongly influenced locally by geography and topography, the large-scale $\delta^{18}O_p$ distribution changes little because it is controlled by the large-scale atmospheric circulation (Poulsen et al., 2007b).

Our results build on this previous study, and indicate that global ocean circulation has a small but important influence on the large-scale distribution of Cretaceous seawater $\delta^{18}O_w$. (The exception occurs in isolated basins, such as the Arctic Ocean and proto-South Atlantic Ocean, where the local precipitation flux can have a large influence on $\delta^{18}O_w$.) In our simulations, Cretaceous surface seawater $\delta^{18}O_w$ is ~0.3‰ less than modern at the low and middle latitudes. This decrease in surface seawater $\delta^{18}O_w$ is mainly due to differences in the partitioning of ^{18}O between the surface and the deep ocean. In the modern ocean, intermediate and deep water is formed primarily in high-latitude oceans, regions with

relatively depleted surface $\delta^{18}O$ (Frew et al., 1995). In the Cretaceous experiments, the subtropical Tethys and proto-South Atlantic Oceans, regions with relatively high surface seawater $\delta^{18}O$, are important sources of intermediate and deep waters. The transport of these waters from the surface to depth lowers surface $\delta^{18}O$ and increases subsurface $\delta^{18}O$. This process of ^{18}O segregation in the ocean is the "compensation effect" described by Roche et al. (2006).

Roche et al. (2006) report on changes in seawater $\delta^{18}O_w$ under warm climate conditions using CLIMBER-2, a coupled ocean-atmosphere model of intermediate complexity, and reach different conclusions from those presented here. Their model results predict an increase in low and mid-latitude surface $\delta^{18}O_w$ by up to 1‰. There are two major differences between our studies. First, Roche et al. (2006) use a modern geography. In contrast to the modern, the Cretaceous geography includes subtropical basins that are not well connected to the global ocean and consequently evolved distinct water mass properties (Poulsen et al., 2001) including relatively enriched $\delta^{18}O_w$. Second, in Roche et al. (2006), water vapor isotopes are not tracked explicitly but are based on "simpler physical hypotheses". Using this methodology, Roche et al. (2006) report increased transport of $\delta^{18}O$-depleted humidity to high latitudes in a warmer world, leading to a decrease in high-latitude $\delta^{18}O_w$. High-latitude deepwater formation and the "compensation effect" then cause the deep ocean to become relatively depleted in ^{18}O and the surface ocean to become enriched. In contrast, with water isotope tracer capabilities, GENESIS predicts $\delta^{18}O$-enriched vapor and precipitation at high latitudes as a result of a reduction in equilibrium fractionation in a warmer (high CO_2) world (Poulsen et al., 2007b).

4.4.2. Implications for oxygen isotope paleo-thermometry

Oxygen isotope paleo-thermometry, arguably the most valuable tool in reconstructing past climate, requires knowledge of past seawater $\delta^{18}O_w$. In the absence of this information, previous studies have assumed that past seawater $\delta^{18}O_w$ was constant or the same as modern. Our simulation of Cretaceous $\delta^{18}O_w$ allows us to assess these assumptions, and their influence on paleo-temperature estimates. Here, we calculate and compare paleo-temperature estimates using constant (-1.0‰ SMOW), present-day, and simulated seawater $\delta^{18}O$. The present-day $\delta^{18}O$ distribution is based on a best fit to surface seawater $\delta^{18}O$ from southern hemisphere Atlantic and Pacific Oceans and describes $\delta^{18}O$ distribution as a function of latitude (Zachos et al., 1994). In comparison to the LeGrande and Schmidt (2006) data, the Zachos et al. (1994) present-day $\delta^{18}O$ distribution is systematically higher, ranging from an increase of 0.02‰ at ~30°N to as much as 2.2‰ in the Arctic region, and no more than 0.3‰ in the southern hemisphere.

Following Roche et al. (2006), we use the temperature-$\delta^{18}O$ equation from Shackleton (1974):

$$T = 16.9 - 4.38(\delta^{18}O_c - \delta^{18}O_w) + 0.1(\delta^{18}O_c - \delta^{18}O_w)^2 \qquad (1)$$

where $\delta^{18}O_c$ and $\delta^{18}O_w$ denote the oxygen isotopic content of foraminiferal calcite and seawater, respectively. To estimate the temperature bias (ΔT) due to the various assumptions about $\delta^{18}O_w$ ($\Delta(\delta^{18}O_w)$), we derive the first-order Taylor expansion of (1), which is:

$$\Delta T \sim 4.18\Delta(\delta^{18}O_w) \qquad (2)$$

Expression (2) indicates that $\delta^{18}O_w$ is a significant factor in calculating paleotemperature.

Similar results would be derived using other temperature-$\delta^{18}O_w$ relationships (Bemis et al., 1998, Table 1).

We use (2) to compare the influences of common $\delta^{18}O_w$ assumptions and our simulated $\delta^{18}O_w$ on paleo-temperature estimates. (Note that here we use "uncorrected" Cretaceous $\delta^{18}O_w$ from our simulation, and the values from Zachos et al (1994) minus 1.0‰ to account for the absence of Cretaceous polar ice sheets). In comparison to paleotemperatures estimated using our simulated zonal-average Cretaceous $\delta^{18}O_w$, paleotemperatures estimated using either a uniform $\delta^{18}O_w$ (-1.0‰) or the Zachos et al. (1994) present-day distribution of $\delta^{18}O_w$ generally overestimate paleotemperatures (Fig. 4-10). At high latitudes, this temperature overestimate is substantial, ranging from 2 to 17.6°C. Using the Zachos et al. (1994) present-day $\delta^{18}O_w$ also leads to substantially higher (~3°C) paleotemperature at low latitudes.

The use of zonal-average $\delta^{18}O_w$ is another important source of uncertainty in calculating paleotemperature. Our model results indicate that local $\delta^{18}O_w$ can vary by more than 1.5‰ from zonal-average $\delta^{18}O_w$ at high latitudes (Fig. 4-11), leading to isotopic paleo-temperatures that differ up to 6°C according to (2). These large zonal differences in $\delta^{18}O_w$ occur in latitudinal zones with isolated or semi-isolated basins, including the Arctic, northern Tethys, and northern South Atlantic Oceans. In these regions where seawater exchange is limited by features of the paleogeography, the surface $\delta^{18}O_w$ is more strongly influenced by local precipitation $\delta^{18}O_w$ and deviates from open ocean $\delta^{18}O_w$.

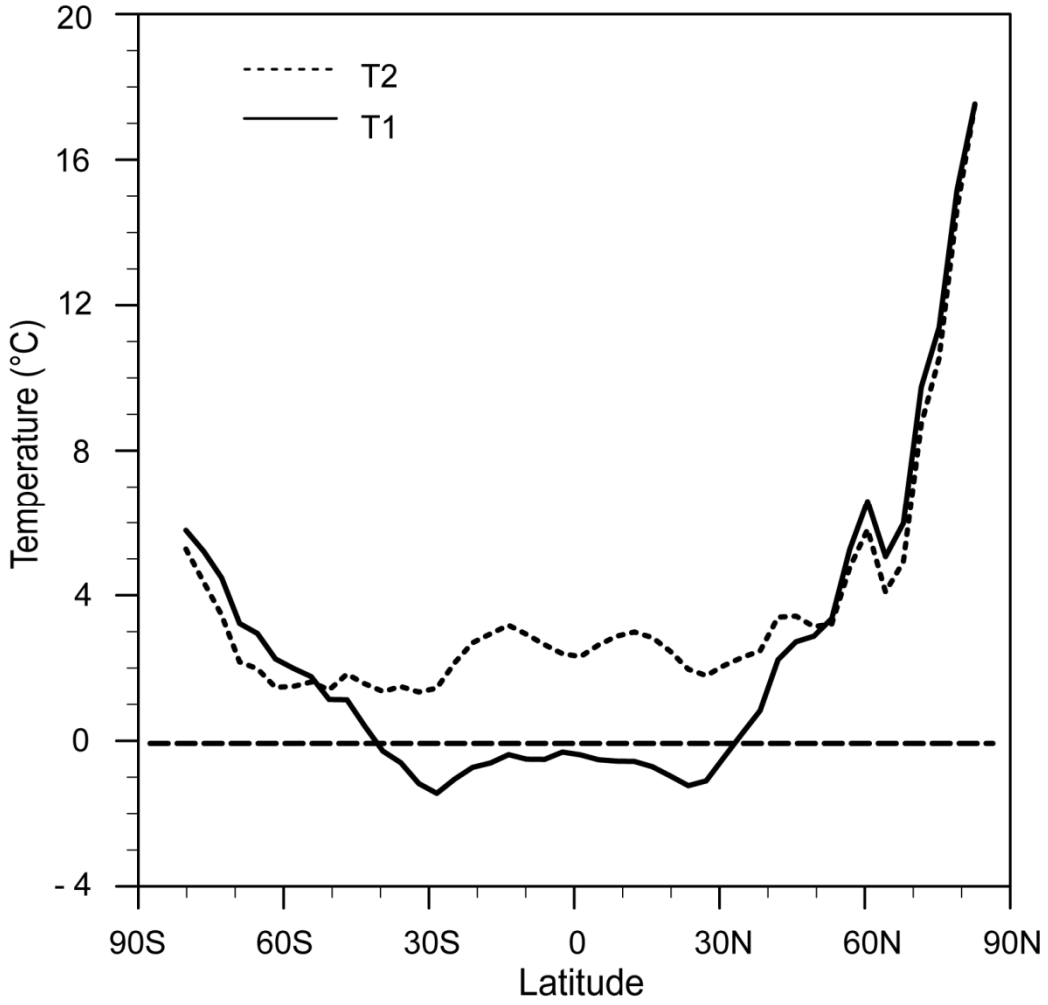

Figure 4-10. Comparison of temperature estimates using different assumptions about Cretaceous seawater $\delta^{18}O_w$. T1 ($T_{uniform} - T_{K\text{-}Flat}$) (solid line) denotes the temperature difference that results from assuming a uniform global mean surface seawater $\delta^{18}O_w$ of -1.0‰ (SMOW) rather than the $\delta^{18}O_w$ predicted in K-Flat. T2 ($T_{present} - T_{K\text{-}Flat}$) (dashed line) denotes the temperature difference that results from using present latitudinal $\delta^{18}O_w$ distribution from Zachos et al (1994) rather than the $\delta^{18}O_w$ from K-Flat. As discussed in the text, we here use the "uncorrected" Cretaceous $\delta^{18}O_w$ from our simulation, and the Zachos et al (1994) $\delta^{18}O_w$ minus 1.0‰ (SMOW).

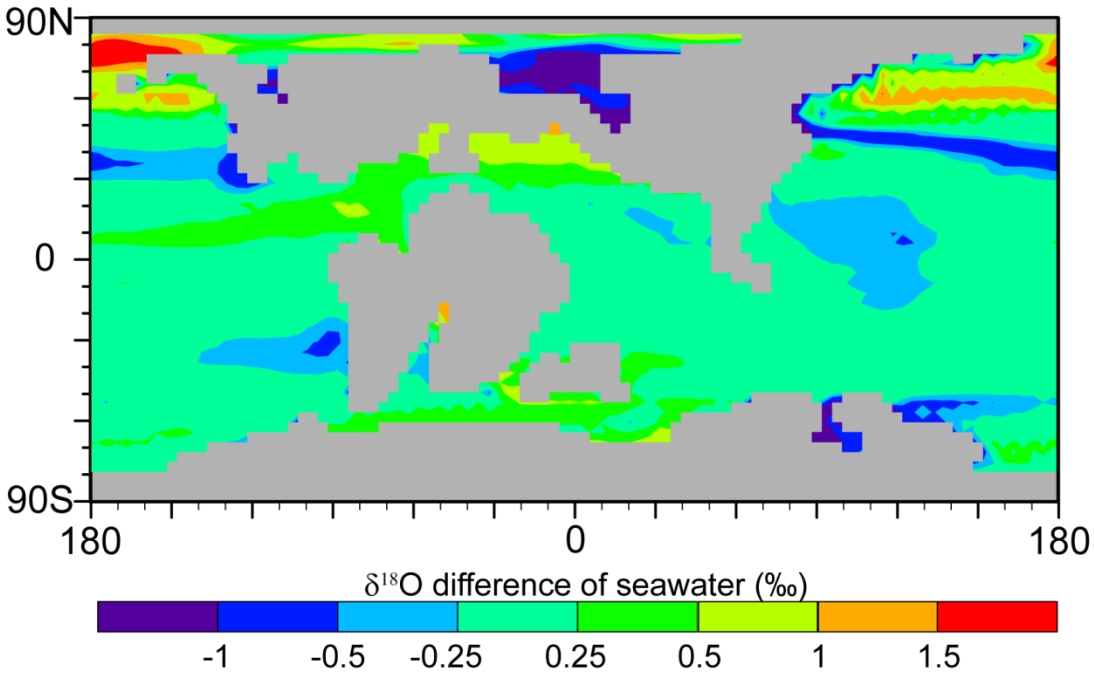

Figure 4-11. Mean-annual $\delta^{18}O_w$ (SMOW) difference between local and zonal average surface seawater. For each grid cell, the $\delta^{18}O_w$ difference is obtained by subtracting the zonal average $\delta^{18}O_w$ at that latitude from the local $\delta^{18}O_w$.

The simulation of the Cretaceous equator-to-pole temperature gradient has been a long-standing problem (Barron, 1983; Poulsen et al., 1999b; Poulsen, 2004; Bice et al., 2003). Proxy data, most notably $\delta^{18}O$ paleothermometry, has been used to infer that the equator-to-pole temperature gradient was small mainly as a result of very warm high-latitude paleotemperatures (e.g. Huber et al., 1995). In contrast, climate models have traditionally simulated large Cretaceous equator-to-pole temperature gradients. This mismatch has typically been attributed to flaws in the climate models stemming from, for example, the treatment of heat transport and clouds (e.g. Barron, 1994; Sloan and Pollard, 1998; Kump and Pollard, 2008). Here, we emphasize another source of potential model-data mismatch, the interpretation of proxy data. Our calculation of Cretaceous seawater $\delta^{18}O$ substantially ameliorates the model-data mismatch by reducing the temperature inferred from high-latitude calcite $\delta^{18}O$. We do not claim to have solved this problem; other types of non-isotopic proxy data also suggest that the Cretaceous high-latitude temperatures were warm, and site specific model-data intercomparisons are still required to fully assess the significance of the $\delta^{18}O_w$ effect on isotopic paleotemperatures. However, we do view this as an important step forward, one that is critical to truly assessing the capability of models to simulate past warm worlds.

4.4.3. Oceanic gateways, continental runoff, and seawater $\delta^{18}O_w$

Our modern and Cretaceous experiments indicate that the resolution of oceanic gateways can substantially influence regional seawater $\delta^{18}O_w$ (Fig. 4-7). In both modern and Cretaceous experiments, the Bering Strait is critical to ocean mixing and isotopic exchange between the Pacific and Arctic Oceans. With no or weak exchange, Arctic seawater $\delta^{18}O$ will tend to resemble the high-latitude precipitation that feeds it.

The implications of these results are twofold. Firstly, paleogeography can be a first-order control on regional seawater $\delta^{18}O$. Secondly, in the absence of detailed knowledge about paleogeographic evolution, oxygen isotopic records should be interpreted with caution. Paleogeographic or eustatic changes that alter regional circulation and seawater $\delta^{18}O$ could be misconstrued as climatic change. Isotopic proxies from semi-isolated ocean basins would be particularly susceptible to this influence. Similar caveats on the interpretation of marine water isotope records have been found in other isotopic GCM experiments for the Holocene (Schmidt et al., 2007).

Continental runoff is also potentially an important influence on seawater $\delta^{18}O$. In this study, we have uniformly distributed continental runoff over the surface of the ocean, and have not tracked runoff from specific drainage basins into the ocean. This treatment of runoff could influence the simulated isotopic content of seawater especially in semi-isolated basins. A river routing scheme, in which runoff from specified drainage basins flows into the ocean at a point source, is likely to enhance regional isotopic differences in many basins. For example, the seawater $\delta^{18}O$ of the Cretaceous Arctic Ocean, which is relatively depleted in ^{18}O due to net precipitation, is likely to become further reduced with inflow of high-latitude continental runoff. In addition to this direct effect on seawater $\delta^{18}O$, continental runoff could also alter the distribution of ^{18}O between the surface and deep ocean through its influence on deep-water formation. Bice et al. (1997) have shown that the specification of continental runoff in an ocean general circulation model can substantially change the location of deep-water formation.

4.5. Conclusions

We have developed a coupled ocean-atmosphere general circulation model that successfully simulates many aspects of modern precipitation and seawater $\delta^{18}O$ distribution. When applied to the Cretaceous, the model predicts surface seawater $\delta^{18}O$ that is similar in many respects to modern. Differences from the modern include: 1) a small decrease in low- and middle-latitude surface seawater $\delta^{18}O$ due to a decrease in equilibrium fractionation, and a "compensation effect" caused by partitioning of the heavy isotope in the deep ocean due to intermediate and deep-water formation in subtropical basins, and 2) large changes in Arctic surface seawater $\delta^{18}O$ that are linked to differences in seawater exchange rates between the Pacific and Arctic Oceans. The similarity between modern and Cretaceous zonal-average surface seawater $\delta^{18}O$ highlights the fact that surface $\delta^{18}O_w$ is mainly constrained by large-scale atmospheric and oceanic circulation patterns, which change little between the modern and Cretaceous except in regions where paleogeography creates isolated or semi-isolated ocean basins.

Our results have important implications for oxygen isotope paleothermometry, and indicate that conventionally used assumptions of surface seawater $\delta^{18}O$ likely overestimate Cretaceous mid- and high-latitude temperature. Compensating for these isotopic effects by using simulated $\delta^{18}O_w$ reduces the Cretaceous low equator-to-pole thermal gradient problem.

Chapter V

No climate extremes in the mid-Cretaceous

Abstract

The Cretaceous thermal maximum at the Cenomanian/Turonian boundary represents the warmest interval in the last 144 my. Cretaceous tropical paleotemperatures derived from the oxygen isotopic concentration of planktonic foraminifera ($\delta^{18}O_c$) indicate that surface temperatures increased through the mid-Cretaceous and peaked at temperatures as high as 36 °C, more than 6 °C warmer than modern. During this same interval, however, atmospheric pCO_2 is estimated to have declined and rapid (~100 ky), positive excursions in marine $\delta^{18}O_c$ have been cited as evidence of continental glaciation. Here, we evaluate whether factors other than global climate change could explain the marine $\delta^{18}O_c$ record. Using a coupled ocean-atmosphere general circulation model with isotope-tracking capabilities, we explore the response of marine $\delta^{18}O_c$ to global climate change induced by atmospheric pCO_2 and regional oceanographic changes initiated by prescribed alterations in regional paleogeography or freshwater forcing. Our results show that doubling atmospheric pCO_2 leads to a nearly uniform depletion in marine $\delta^{18}O_c$. In contrast, changes in regional oceanography produce excursions in marine $\delta^{18}O_c$ as large as those observed yet with little influence on global temperatures. Thus, we suspect that the apparent inconsistency between mid-Cretaceous climate proxy records is due to the fact

that they reflect regional oceanographic rather than global climate change. On the basis of our results, we propose that the mid-Cretaceous was neither a thermal maximum nor an ice age.

5.1. Introduction

The oxygen isotope composition of marine carbonate ($\delta^{18}O_c$) is the most widely employed proxy for both short- and long- term paleoclimate change. Oxygen isotope paleothermometry is based on the principle that oxygen isotope fractionation during carbonate precipitation is negatively correlated with ambient temperature such that low $\delta^{18}O_c$ indicates high seawater temperature. In practice, oxygen isotope paleothermometry also requires knowledge of the ambient seawater oxygen isotope concentration ($\delta^{18}O_{sw}$). However, because there are no independent proxies of $\delta^{18}O_{sw}$, this value is often assumed to be globally uniform or to have a distribution similar to modern. During times of glaciation, $\delta^{18}O_c$ preserves a signal of both seawater temperature and ice volume. The preferential storage of ^{16}O in terrestrial ice sheets causes enrichment of ^{18}O in seawater. As a result, rapid positive excursions in $\delta^{18}O_c$ are often interpreted as a sign of ice-sheet growth.

The long-term depletion of marine carbonate $\delta^{18}O_c$ in the mid-Cretaceous to their lowest values in 144 my has been used to indicate global surface warming that culminated in the Cretaceous thermal maximum during the latest Cenomanian and early Turonian (Bice et al., 2003, 2006; Clarke and Jenkyns, 1999; Jenkyns et al., 1994; Huber et al., 1995, 2002; Wilson et al., 2002). Paradoxically, short-term (~100 ky) positive excursions in carbonate $\delta^{18}O_c$ during this same interval have been interpreted to reflect the growth of continental ice sheets on Antarctica (Bornemann et al., 2008; Galeotti et al.,

2009; Miller et al., 2003, 2005; Stoll and Schrag, 2000). Both interpretations of mid-Cretaceous carbonate $\delta^{18}O_c$ are at odds with proxy estimates and theoretical calculations of atmospheric pCO_2, which suggest that values decreased from the Aptian-Albian through the Turonian but remained above 1000 ppmv (Bice and Norris, 2002; Larson, 1991; Crowley and Berner, 2001). The high but declining pCO_2 values are inconsistent with long-term warming and the presence of continental ice sheets. Modeling studies of Paleozoic and Cenozoic ice ages report the growth of continental ice sheets with a detectable isotopic signal (~0.2‰ enrichment in seawater $\delta^{18}O_{sw}$) occurs only once pCO_2 levels have exceeded ~800 ppmv, regardless of the orbital configuration (DeConto and Pollard, 2003; Horton and Poulsen, 2009).

To reconcile the apparent decoupling between declining atmospheric pCO_2 and proxy-inferred warming, a "hidden" pulse of Turonian CO_2 outgassing has been proposed (Wilson et al., 2002). Alternatively, Poulsen et al. (2003) suggest that this discrepancy could be explained by a regional reorganization of the North Atlantic circulation during opening of the equatorial South Atlantic gateway, which led to seawater freshening and isotope lightening of the North Atlantic.

Similarly, the short-term positive carbonate $\delta^{18}O_c$ excursions have been attributed to changes in the water mass balance in the North Atlantic (Ando et al., 2009; Friedrich et al., 2008; Voigt et al., 2004). Voigt et al. (2004) propose that regional cooling in the North Atlantic during sea-level lowstand led to enhanced oceanic ventilation and subsurface cooling, preserved as an increase in carbonate $\delta^{18}O_c$. In contrast, Friedrich et al. (2008) postulate that the increases in carbonate $\delta^{18}O_c$ reflect enhanced formation and sinking of warm, saline intermediate waters through surface evaporation in the tropical North

Atlantic

These studies highlight the need to investigate the influence of global climate change, eustatic sea level, paleogeography and freshwater budget on marine carbonate $\delta^{18}O_c$. In this study, we quantify these effects using a water isotope-enabled ocean-atmosphere general circulation model (GCM) and compare them with the marine carbonate $\delta^{18}O_c$ from the North Atlantic. Our results show that doubling atmospheric pCO_2 leads to a relatively uniform surface and subsurface depletion in carbonate $\delta^{18}O_c$. Changes in sea level, regional paleogeography and freshwater forcing have a substantial influence on carbonate $\delta^{18}O_c$ that varies with latitude and depth.

5.2. Methods

We investigate the effects of CO_2, sea level and regional paleogeography on marine carbonate $\delta^{18}O_c$ using GENMOM, a fully coupled ocean-atmosphere GCM with isotope-tracking capability. GENMOM has been shown to successfully simulate modern and paleo- meteroic and seawater oxygen isotope composition (Mathieu et al., 2002; Poulsen et al., 2007, 2010; Zhou et al., 2008). The atmospheric component, the GENESIS version 3.0 Earth System Model (GENESIS3), is composed of an atmospheric GCM coupled to multilayer land surface models of vegetation, soil, snow and sea ice (Thompson and Pollard, 1997). The oceanic component, the Modular Ocean Model version 2 (MOM2), is a 3-dimensionl, z-coordinate ocean GCM with passive-tracer capabilities (Pacanowski, 1995). A horizontal resolution of ~3.75° was implemented to GENESIS3 and MOM2. GENESIS3 and MOM2 have 18 and 20 vertical levels, respectively. Initial seawater temperatures and salinity for MOM2 were taken from

modern observations. In order to promote long equilibrium runs, we employed the synchronous-asynchronous coupling techniques as described in Zhou et al. (2008). Each GENMOM experiment was integrated for several synchronous-asynchronous iterations until the rate of change of the global ocean temperature became negligible (~ 0.1 °C/ky).

Following Zhou et al. (2008), our control experiment (8x) was implemented with a mid-Cretaceous lowstand paleogeography and topography (Barron, 1987) (Fig. 5-1) and 8x pre-industrial levels atmospheric pCO_2. In the absence of accurate reconstructions, open ocean bathymetry was set to 5600 m. Other boundary conditions remain the same in each experiment. Earth orbital parameters and concentrations of trace gases (methane, nitrous oxide) were set to their pre-industrial values. Solar luminosity was reduced to 99% of the modern (Gough, 1981). Global seawater $\delta^{18}O_{sw}$ was initialized at -1.0‰ (SMOW) to represent the absence of large continental ice sheet in mid-Cretaceous (Shackleton and Kennett, 1975).

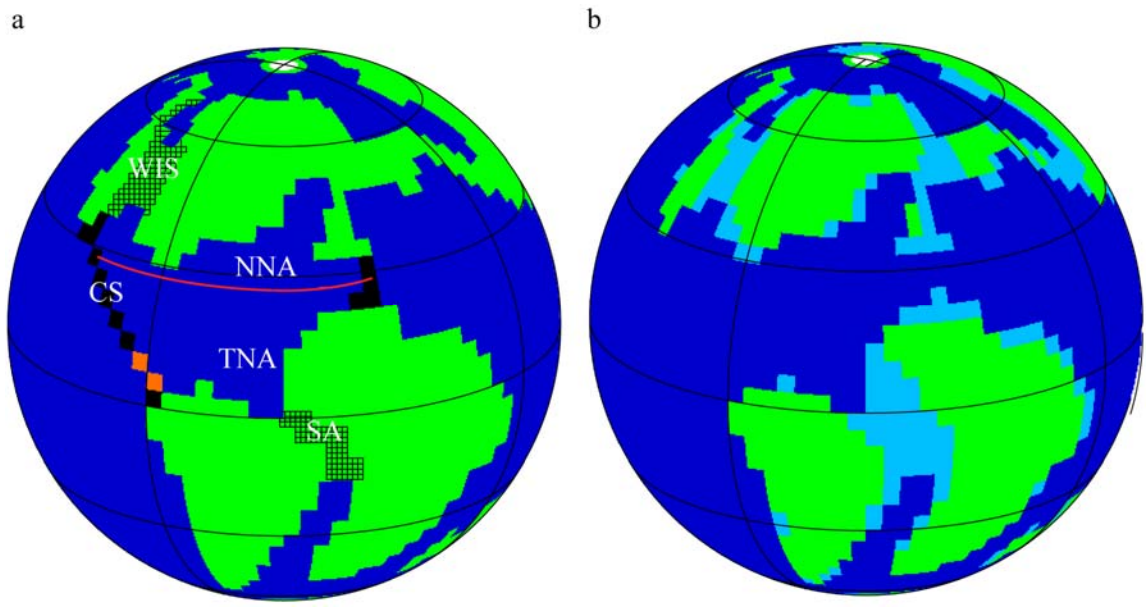

Figure 5-1. Paleogeography for the 8x experiment (a), and Paleogeography for the HiStand experiment (b). Continents are shaded in green and deep oceans (5600 m) are shaded in dark blue. The shading and hatching in these figures illustrates the paleogeography used in our sensitivity experiments. Black hatching in a marks the Western Interior Seaway (WIS) and the South Atlantic Ocean (SA), which were opened in the OpenWIS and OpenSA experiments, respectively. The black shading in a illustrates the restriction of North Atlantic Ocean in the SmallCS experiment, allowing only a narrow gateway between the Pacific and Atlantic (illustrated in orange). In the CloseCS experiment, the region shaded in orange was specified as land, closing the ocean gateway. In b, shallow seas (with a depth of 200 m) are shaded in light blue. A red line indicates the division between the northern North Atlantic (NNA) and tropical North Atlantic (TNA).

We have completed three series of sensitivity experiments that evaluate the response to (i) atmospheric pCO_2, (ii) paleogeographic changes due to gateway opening/closing and eustacy, and (iii) fresh-water forcing (Table 5-1). To evaluate the role of atmospheric CO_2, a simulation with 16x pre-industrial levels pCO_2 was completed. Atmospheric pCO_2 of 16x pre-industrial levels falls with the upper limit of the mid-Cretaceous proxy estimates (Bice and Norris, 2002, figure 1). Five additional sensitivity experiments were conducted to represent the rise of eustatic sea-level (HiStand) (Haq et al., 1987), the opening of the South Atlantic gateway (OpenWIS) and Western Interior Seaway (OpenWIS) and the narrowing/closing of the Caribbean Seaway (Small CS/ CloseCS) (Iturralde-Vinent, 2003) during the mid-Cretaceous.

To examine the effects of freshwater forcings, five MOM2 experiments were performed in which the freshwater fluxes in the northern or tropical North Atlantic were modified (Table 5-1 and Fig. 5-2). The modeling technique used in these experiments was slightly different than that in the other sensitivity experiments. Our freshwater forcing runs were started from the end of our equilibrium control experiment (8x). To mimic changes in freshwater forcing in the North Atlantic, we systematically altered the surface freshwater budget (i.e. precipitation-evaporation) passed from GENESIS to MOM. To mimic freshening (FreshNNA), the freshwater budget was increased by a factor of 3 in regions with a positive budget and decrease by 1/3 in regions with a negative budget. Similarly, to mimic enhanced evaporative conditions (SaltNNA, SaltTNA), the freshwater budget was decreased by 1/3 in regions with a positive budget and increased by a factor of 3 in regions with a positive budget (Table 5-1).

Table 5-1. List of experiments, simulated global-average seawater temperatures and $\delta^{18}O$ (T_{gl}, °C), North Atlantic Ocean seawater temperature and $\delta^{18}O$ (T_{NA}, °C; δ_{NA}, ‰), and mass flux of the North Atlantic meridional overturning circulation (NAMOC, Sv).

Exp.	Description	25 m			1059 m		*NA
		T_{gl}	T_{NA}	δ_{NA}	T_{gl}	*T_{NA}	MOC
8x	2240 ppmv CO_2	22.9	26.0	-0.83	9.4	11.2	10.4
16x	4480 ppmv CO_2	26.8	29.8	-0.79	13.1	14.6	8.9
HiStand	Highstand	23.0	26.4	-0.73	8.6	10.2	7.7
OpenSA	Open South Atlantic	22.8	26.5	-0.80	9.2	11.5	10.6
OpenWIS	Open WIS	22.8	25.6	-0.92	9.3	11.0	8.7
SmallCS	Narrow Caribbean Seaway	22.7	26.1	-0.79	10.2	13.6	12.1
CloseCS	Close Caribbean Seaway	22.7	26.2	-0.67	10.4	16.3	16.6
+SaltNNA	Reduce freshwater flux (FF) into the northern NA (NNA) to 1/3 for 8x	22.9	26.0	-0.86	9.6	12.7	14.0
+FreshNNA	Triple FF into the NNA	22.9	25.9	-0.77	9.2	10.2	6.7
+SaltTNA	Reduce FF into the tropical NA (TNA) to 1/3	22.9	26.1	-0.84	9.9	12.8	12.2
+SaltNCS	Reduce FF into the NNA to 1/3 for SmallCS	22.7	26.0	-0.98	10.6	15.8	16.6
+SaltTCS	Reduce FF into the TNA to 1/3 for SmallCS	22.7	25.7	-1.07	9.3	17.2	17.8

" + " experiment is completed with MOM2, otherwise, experiment is completed with GENMOM.

"*" Linear analysis demonstrates a positive correlation between NAMOC and bathyal temperature over the North Atlantic with 8x atmospheric pCO_2:

T_{NA} (1059 m) = 0.64 * NAMOC + 5.2, $r^2 = 0.93$.

δ_{NA} is ~-0.9- -1.0 ‰ at 1059 m except in the CloseCS experiment, in which bathyal seawater $\delta^{18}O_{sw}$ is as enriched as surface seawater $\delta^{18}O_{sw}$ in the North Atlantic.

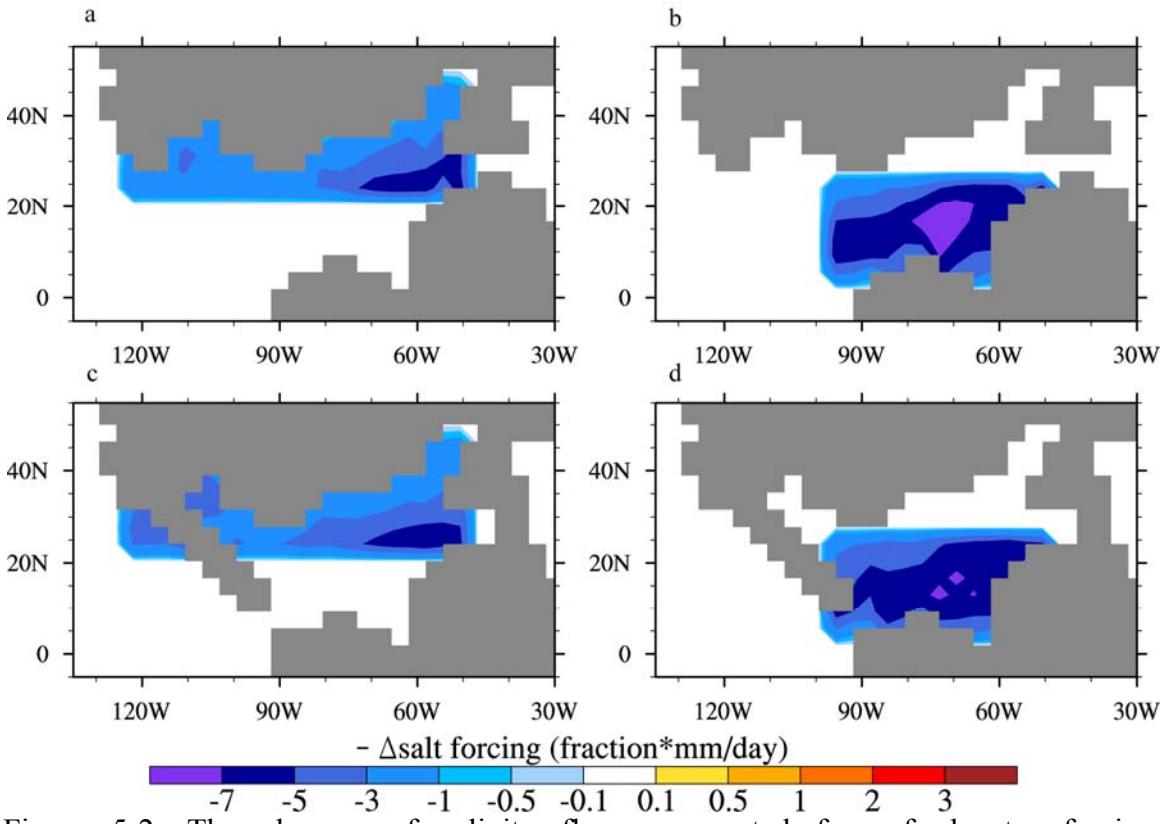

Figure 5-2. The changes of salinity fluxes converted from freshwater forcing (precipitation + runoff - evaporation) into the North Atlantic in the SaltNNA – 8x experiments (a); SaltTNA – 8x experiments (b); SaltNCS – SmallCS experiments (c); and SaltTCS - SmallCS experiments (d). Grey shading represents continents, purple and blue shading marks the region with reduced freshwater fluxes (positive salinity forcing), and yellow and red shading marks the region with enhanced freshwater fluxes (negative salinity forcing).

To test whether the influences of freshwater forcings vary with paleogeographic conditions, additional experiments were completed using with a narrow Carribean gateway (Table 5-1, SaltNCS, SaltTCS). All other surface meteorological forcings (temperature, wind stress) for MOM2 were taken directly from the 8x or SmallCS experiment. Each MOM2 experiment was run for 1500 years. All model results shown in this study represent the average of the final twenty years.

5.3. Results

5.3.1 Response of seawater temperatures and $\delta^{18}O_{sw}$

Increasing atmospheric pCO_2 from 2240 to 4480 ppmv leads to an increase in global mean annual temperature by ~4.0 °C (Table 5-1). Due to the snow-sea ice-albedo feedbacks, the warming is ~2.0 °C greater at high latitudes (Fig. 5-3a). Surface warming leads to reduced equilibrium fractionation of water oxygen isotopes especially at high latitudes. Consequently, precipitation $\delta^{18}O_p$ is enriched by ~1.0-2.0‰ at middle latitudes and up to 5.7‰ over the Arctic region (not shown). In contrast, the changes in seawater $\delta^{18}O_{sw}$ are largely negligible except at the northern high latitudes (Fig. 5-3b). This is because the patterns of global atmospheric and oceanic circulations, which control the large-scale distribution of seawater $\delta^{18}O_{sw}$ (Zhou et al., 2008), change little with atmospheric pCO_2 (Poulsen et al., 2001, 2007). Unlike the open oceans, however, seawater $\delta^{18}O_{sw}$ in the semi-closed Arctic Ocean mimics high-latitude precipitation $\delta^{18}O_p$, due to its limited connection with the open oceans (Poulsen et al., 2007; Zhou et al., 2008).

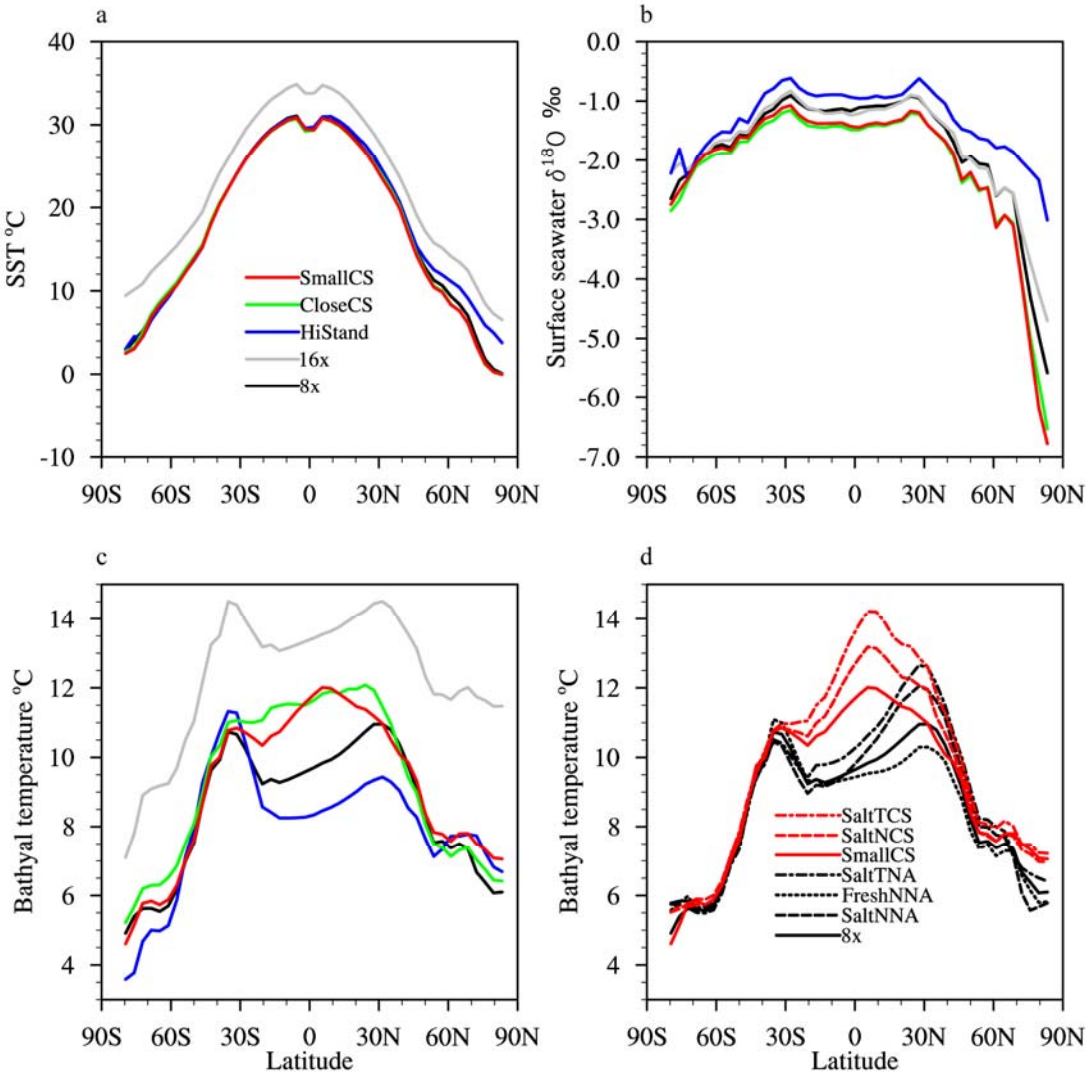

Figure 5-3. Mean-annual zonal average sea-surface temperature (SST) (°C) (a), surface seawater $\delta^{18}O_{sw}$ (‰) (b), bathyal seawater temperatures (at 1059 m) (°C) (c) for the 8x, 16x, HiStand, CloseCS and SmallCS GENMOM experiments, and bathyal seawater temperatures (at 1059 m) (°C) for the SaltNNA, FreshNNA, SaltTNA, SaltNCS and SaltTCS MOM2 experiments (d). The openings of WIS and SA as well as salinity forcing barely change mean-annual zonal surface seawater temperatures and seawater $\delta^{18}O_{sw}$ except at the Arctic latitudes and thus are not shown.

Unlike atmosphere pCO_2, changes in regional paleogeography and freshwater forcing alter global mean annual SSTs only slightly (≤ 0.2 °C) (Table 5-1). Nonetheless, changes in regional SSTs and subsurface seawater temperatures are remarkable. The flooding of the Western Interior Seaway, northwestern Europe, and European shelf in the HiStand experiment (Fig. 5-1b) enhance northward transport of the warm, $\delta^{18}O_{sw}$-enriched subtropical North Atlantic water. As a result, mean-annual zonal SSTs increase at the northern mid-to-high latitudes (Fig. 5-3a, blue line). Moreover, the thermocline seawater (~75-400 m) in the subtropical North Atlantic and European shelf-seas warms by ~2.0 °C. The slight warming (~0.5 °C) over the North Atlantic in the HiStand and OpenSA experiments (Table 5-1) is due to the opening of tropical South Atlantic (Fig. 5-1), which leads to a warming of ~2.0 °C in the tropical North Atlantic. While narrowing/closing the Caribbean Seaway (SmallCS/CloseCS) barely influences zonally averaged SSTs (Fig. 5-3a), it warms the tropical North Atlantic by ~1.5 °C and cools the subpolar northern Pacific by ~1.0 °C, corresponding to reduced westward flow from the tropical North Atlantic to the Pacific Ocean at shallow depth (not shown). The responses of bathyal seawater temperatures are more pronounced. Flooding (HiStand) and increasing the northern North Atlantic freshwater forcing (FreshNNA) both decrease bathyal (> 900 m) temperatures, whereas narrowing/closing the Caribbean Seaway (SmallCS/CloseCS) and reducing the North Atlantic freshwater forcing (SaltNNA, SaltTNA, SaltNCS and SaltTCS) increase zonal bathyal temperatures by up to 2.0 °C at low latitudes (Fig. 5-3 c,d). The changes in zonal bathyal temperatures originate from the North Atlantic and are caused by the variations in the North Atlantic meridional overturning circulation (NAMOC). In general, weakening of the NAMOC leads to

bathyal cooling and strengthening of the NAMOC leads to bathyal warming, regardless of the causes of NAMOC variations (Table 5-1). For example, with respect to the 8x experiment, NAMOC in the FreshNNA experiment weakens by 3.7 Sv (35.6%) and bathyal temperatures decrease by 0.2 °C globally and 1.0 °C in the North Atlantic. In contrast, NAMOC in the CloseCS experiment strengthens by 6.2 Sv (59.6%) and bathyal temperatures increase by 1.0 °C globally and 5.1 °C in the North Atlantic.

The degree of the North Atlantic restriction also substantially influences the distribution of surface seawater $\delta^{18}O_{sw}$ (Fig. 5-3b). As a result of the intensified exchanges among ocean basins in the HiStand experiment, mean-annual zonal surface $\delta^{18}O_{sw}$ increases by ~0.2 ‰ at low-to-mid latitudes and up to 2.6 ‰ at the northern high latitudes. On the contrary, due to the reduced westward flow, narrowing/closing the Caribbean Seaway (SmallCS/CloseCS) decreases the surface seawater $\delta^{18}O_{sw}$ by ~0.3 ‰ in the northern Pacific Ocean and up to ~1.0 ‰ in the Arctic Ocean, as manifested in the zonal mean-annual surface $\delta^{18}O_{sw}$. Variations in seawater $\delta^{18}O_{sw}$ largely disappear below ~1000 m except in the CloseCS experiment, in which an enrichment of ~0.3‰ penetrates to 2000 m over the North Atlantic (Table 5-1).

5.3.2 Response of the Atlantic carbonate $\delta^{18}O_c$

As most reported mid-Cretaceous marine carbonate $\delta^{18}O_c$ are from the Atlantic and its adjacent ocean basins, in this section we focus on the response of the Atlantic carbonate $\delta^{18}O_c$ to the prescribed regional and global forcing.

The response of the Atlantic $\delta^{18}O_c$ to atmospheric pCO_2, regional paleogeography and freshwater forcing varies remarkably in both magnitude and pattern as summarized below: (i) Doubling atmospheric pCO_2 (16x) leads to a relatively uniform depletion of

~0.8‰ in the North and South Atlantic carbonate $\delta^{18}O_c$ (Fig. 5-4a). (ii) The opening of the tropical South Atlantic (HiStand and OpenSA) facilitates exchanges between the warm, saline, $\delta^{18}O$-enriched tropical South Atlantic water and its adjacent tropical North Atlantic and subtropical South Atlantic waters and affects carbonate $\delta^{18}O_c$ in multiple ways (Fig. 5-4 b-c): a) the reduced zonal shallow seawater $\delta^{18}O_{sw}$ gradient at the low-to-mid latitudes causes a slight decrease (~0.3‰) at low latitudes and enrichment (~0.4-1.0‰) at middle latitudes in the South Atlantic; b) enhanced formation of tropical South Atlantic warm intermediate water leads to a decrease of up to 0.6 ‰ to a depth of > 1000 m; c) reduced formation of warm deepwater in the tropical South Atlantic leads to an increase of > 0.6‰ at depth; and d) slight warming of the tropical North Atlantic leads to a decrease of ~0.4‰. (iii) In the HiStand experiment, the NAMOC-induced cooling enhances the North Atlantic benthic $\delta^{18}O_c$ by ~0.3‰ and the subtropical thermocline warming decreases $\delta^{18}O_c$ by ~0.6‰ (Fig. 5-4b). (iv) The enhanced downwelling of warm, saline water in the tropical North Atlantic due to the narrowing/closing of Caribbean Seaway (SmallCS/CloseCS) leads to reduction in the North Atlantic benthic $\delta^{18}O_c$ comparable to CO_2-induced depletion (comparing Fig. 5-4 d-e with Fig. 5-4a). In addition, the depth of the maximum decrease increases by > 800 m with the fully closed seaway. Nonetheless, the responses of shallow $\delta^{18}O_c$ are negligible beyond 10 ºN. (v) Enhanced formation of warm intermediate water encouraged by decreasing freshwater forcing over the tropical (SaltTNA, SaltTCS) or northern North Atlantic (SaltNNA, SaltNCS) decreases benthic $\delta^{18}O_c$ by up to 1.0-1.5‰ (Fig. 5-4 f-h). In addition, while the patterns of $\delta^{18}O_c$ depletion induced by changes in the northern North Atlantic are similar, the depletion caused by changes in the tropical North Atlantic is more remarkable in both

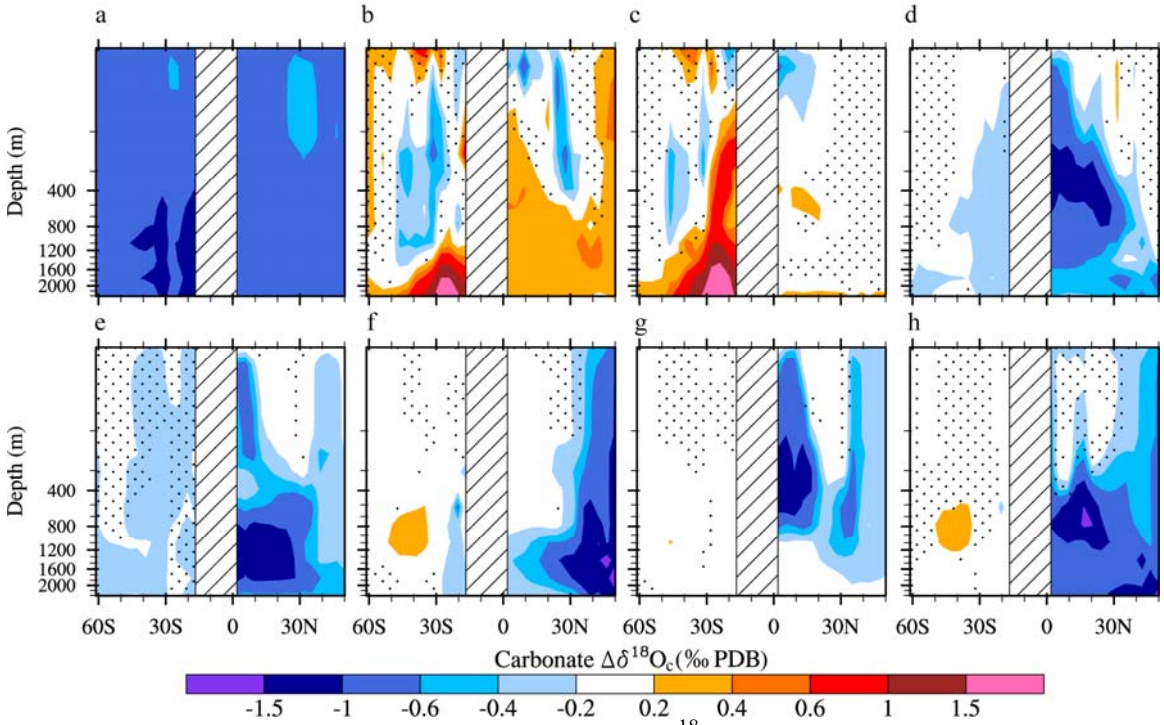

Figure 5-4. Mean-annual, zonal-average carbonate $\delta^{18}O_c$ (‰ in PDB) in North and South Atlantic Oceans for the 16x – 8x experiments (a), HiStand – 8x experiments (b), OpenSA – 8x experiments (c), SmallCS – 8x experiments (d), CloseCS – 8x experiments (e), SaltNNA – FreshNNA experiments (f), SaltTNA– 8x experiments (g), and SaltTCS – SmallCS experiments (h). Slashed white shading marks continents. Stippled regions show that > 50% variations in carbonate $\delta^{18}O_c$ are caused by changes in seawater $\delta^{18}O_{sw}$, and nonstippled regions show that > 50% variations in carbonate $\delta^{18}O_c$ are due to changes in seawater temperatures. $\delta^{18}O_c$ is calculated based on an equation for non-photosymbiotic planktic foraminiferal $\delta^{18}O_c$ (Bemis et al., 1998: T (°C) = 16.5 - 4.80($\delta^{18}O_c$ - $\delta^{18}O_{sw}$)) at the upper 150 m and an equation for benthic foraminiferal $\delta^{18}O_c$ (Shackleton, 1974: T (°C) = 16.9 - 4.0($\delta^{18}O_c$ - $\delta^{18}O_{sw}$)) below 150 m, using modeled temperatures and seawater $\delta^{18}O_{sw}$.

magnitude and extent as a result of a more restricted Caribbean Seaway (comparing Fig. 5-3g with Fig. 5-3h).

5.4. Discussion

Our model results indicate that changes in regional oceanography could contribute substantially to the depletion in marine carbonate $\delta^{18}O_c$ between Turonian and Albian, consistent with Poulsen et al. (2003). While Poulsen et al. (2003) did not exclude the possibility of a modest rise in atmospheric pCO_2, our model results do not support the hypothesis of CO_2-induced Turonian thermal maximum for three reasons.

First, model results show that increasing atmospheric pCO_2 leads to a relatively uniform decrease in marine carbonate $\delta^{18}O_c$ (warming) that is not observed in the marine isotope record. Observed $\delta^{18}O_c$ varies substantially with sampling sites and depths (Table 5-2). Furthermore, Thiede et al. (1981) report that the western Mid-Pacific Mountains moved equatorward from ~17 °S in Albian to ~11 °S in Turonian based on the rotation of the Pacific Plate. Similarly, Clarke and Jenkyns (1999) estimate that the Exmouth Plateau drifted from ~53 °S to 47 °S from Albian to Turonian. In addition, the Demerara Rise was located at ~15 °N in the Albian and ~5 °N in the Turonian (Smith et al., 1994; Suganuma and Ogg, 2005). After correcting for these latitudinally induced changes using model $\delta^{18}O_{sw}$ gradients, temporal changes in carbonate $\delta^{18}O_c$ becomes insignificant at the Exmouth Plateau and Mid-Pacific Mountains in the Southern Hemisphere and decrease by more than 50% at the tropical Demerara Rise.

Second, our model results show that enhanced formation of warm, saline intermediate water caused by the narrowing/closing of Caribbean Seaway can explain the

Table 5-2. Variations in observed carbonate $\delta^{18}O_c$ (Obv.$\Delta\delta^{18}O_c$) and paleo-latitudes of the sampling locations between Albian and Turonian, and adjusted $\Delta\delta^{18}O_c$ after removing the changes induced by equatorward drift of the sampling sites (Lat-adjust $\Delta\delta^{18}O_c$), and model-estimated $\Delta\delta^{18}O_c$ due to the closure of Caribbean Seaway (CloseCS $\Delta\delta^{18}O_c$).

Location	[1]Paleo-latitude	Obv. $\Delta\delta^{18}O_c$	[2]Lat-adjust $\Delta\delta^{18}O_c$	[3]CloseCS $\Delta\delta^{18}O_c$	Reference
Demerara Rise, NA	15 °N-5 °N	- 0.85	-0.20	0.04	Suganuma and Ogg (2005), Smith et al. (1994), Wilson et al. (2002), Bice et al. (2006)
Exmouth Plateau	53 °S-47 °S	-0.55	-0.07	-0.14	Clarke and Jenkyns (1999)
Mid-Pacific Mountains	17 °S-11 °S	-0.30	-0.09	-0.08	Thiede et al. (1981), Clarke (2001)
Falkland Plateau, SA	61 °S-59 °S	-2.00 -1.50[b]	-1.87 -1.25	-0.21 -0.20	Huber et al. (1995), Bice et al. (2003)
Southern England	38 °N-38 °N	-0.50	-0.50	-0.33	Jenkyns et al. (1994), Voigt et al. (2004)
Blake Nose, NA	25 °N-25 °N	0.72 -1.00[b]	0.72 -1.00	0.20 -1.09	Ogg and Bardot (2001), Huber et al. (2002)

"[1]" The estimated Albian paleo-latitude is shown in the upper rows and Turonian latitude is shown in the lower row at each site. "[2]" $\Delta\delta^{18}O_c$ due to paleo-latitudes changes is calculated using seawater temperatures and $\delta^{18}O_{sw}$ from the 8x experiments. "[3]" $\Delta\delta^{18}O_c$ due to the closure of CS is the $\delta^{18}O_c$ difference between the CloseCS and 8x experiments. "[b]" marks benthic $\delta^{18}O_c$, others are shallow $\delta^{18}O_c$.

Model-estimated carbonate $\delta^{18}O_c$ are derived by using modeled seawater temperature and $\delta^{18}O_{sw}$ and the equation given by Anderson and Arthur (1983), Bemis et al. (1998), for planktic and Shackleton (1974) for bulk carbonate, planktic and benthic foraminifera, respectively.

corrected $\Delta\delta^{18}O_c$ to a large extent (compare Lat-adjust $\Delta\delta^{18}O_c$ and CloseCS $\Delta\delta^{18}O_c$ in Table 5-2) in the absence of a global warming (Table 5-1). This enhanced formation of tropical North Atlantic intermediate water is supported by the low Nd isotope values (MacLeod et al., 2011). The opening of the South Atlantic and sea-level rise could also lead to a modest decrease in carbonate $\delta^{18}O_c$ at the Demerara Rise and European shelf-seas (Fig. 5-4b, c). Furthermore, model results reinforce previous claims that the large depletion in planktonic and benthic $\delta^{18}O_c$ at the Falkland Plateau could have been generated by local/regional changes such as freshwater dilution, mixing between warm water masses and the Southern Ocean cold water masses (Bice et al., 2003; Huber et al., 2002; Poulsen et al., 2003). Taken together, this model-data comparison suggests that the reported depletion in carbonate $\delta^{18}O_c$ from the Albian to the Turonian is likely due to regional changes rather than global warming.

Finally, terrestrial proxy data do not support a Turonian thermal maximum. Global warming should be recorded in terrestrial, as well as marine, and proxy data should be amplified at high latitudes. However, paleotemperatures derived from fossil flora at northern high latitudes (Herman and Spicer, 1996; Parrish and Spicer, 1988; Spicer et al., 2002) do not show increases coeval with $\Delta\delta^{18}O_c$.

The positive excursion in the low-resolution benthic $\delta^{18}O_c$ from the subtropical North Atlantic and its plausible coincidence with sea level fall and Milankovitch forcing have been used to suggest an orbital-driven mid-Cenomanian glaciation (Miller et al., 2003). However, this hypothesis has been challenged by the absence of coeval

enrichment in planktonic $\delta^{18}O_c$ (Moriya et al., 2007; Ando et al., 2009). Variability of the North Atlantic intermediate/deep water circulation has then been proposed as a potential cause for the benthic $\delta^{18}O_c$ enrichment (Ando et al., 2009; Friedrich et al., 2008; Voigt et al., 2004). Our model results provide quantitative support for this idea. Model results consistently demonstrate that benthic $\delta^{18}O_c$ is sensitive to the changes in NAMOC, though the response of shallow $\delta^{18}O_c$ is more variable (Table 5-1 and Fig. 5-4). Furthermore, model results show that the variations in benthic $\delta^{18}O_c$ mainly reflect changes in seawater temperatures rather than $\delta^{18}O_{sw}$. Thus, positive benthic $\delta^{18}O_c$ excursions on Milankovitch scale may manifest regional circulation-induced cooling rather than glaciation-induced enrichment in seawater $\delta^{18}O_{sw}$.

The timescale (sub-million year) of benthic $\delta^{18}O_c$ changes is difficult to explain in the absence of orbitally forced glaciation. We propose a possible link between orbital forcing and positive benthic $\delta^{18}O_c$ during mid-Cretaceous via the hydrological response (freshwater forcing). During times when boreal summer insolation (e.g. perihelion boreal summer with high eccentricity) is maximized, freshwater forcing over the North Atlantic would increase. This freshening would in turn diminish NAMOC, inducing a bathyal cooling and enrichment in benthic $\delta^{18}O_c$. The sea-level fall may facilitate/intensify this NAMOC response by further isolating the North Atlantic basin. Such freshwater-induced NAMOC variation has also been reported for the warm Eocene using a different climate model (Bice et al., 1997), indicating that the NAMOC response is not geography or model dependent. Therefore, the positive benthic $\delta^{18}O_c$ excursions from North

Atlantic/Europe during the mid-Cenomanian or mid-Turonian (Bornemann et al., 2008; Galeotti et al., 2009; Stoll and Schrag, 2000; Voigt et al., 2004) could be induced by reduction in regional MOC rather than glaciation. What caused the mid-Turonian positive excursion in planktonic $\delta^{18}O_c$ reported by Bornemann et al. (2008) in the absence of glaciation? Considering that the excursion is mainly recorded in the carbonate test of the opportunistic taxon *Hedbergella delrioensis*, whose habitat depth is suggested to change with upper ocean stratification (Ando et al., 2010), it seems plausible that this taxon shifted to a slightly deeper, cooler environment when freshwater forcing intensified over the North Atlantic.

In addition, model results confirm our previous conclusion that the degree of oceanic seaway/gateway restrictions could considerably influence surface seawater $\delta^{18}O_{sw}$ (Zhou et al., 2008). Results display that mean-annual zonal average surface seawater $\delta^{18}O_{sw}$ could vary by ~0.5 ‰ at low-to-middle latitude and >1.0‰ by changing sea level and the restriction of Caribbean Seaway (Fig. 5-3b). Additional, a fully closed Caribbean Seaway enriched the North Atlantic seawater $\delta^{18}O_{sw}$ by ~0.3‰ up to 200 m. Therefore, neglecting the variations in paleogeography and sea level could cause misinterpretation of the oxygen isotopic paleotemperatures by several degrees.

5.5. Conclusions

In conclusion, our model results suggest that variations in mid-Cretaceous marine carbonate $\delta^{18}O_c$ likely represent regional oceanographic changes rather than global

warming or glaciation. As the variations in simulated carbonate $\delta^{18}O_c$ are mostly due to changes in seawater temperature, our results are also applicable to other marine climate proxies such as TEX_{86} and Mg/Ca ratios. Our interpretation of the marine $\delta^{18}O_c$ data reconciles conflicting reports of continental glaciation during extreme warmth and rising surface temperatures during a fall in pCO_2.

Chapter VI

Conclusions

The nature of mid-Cretaceous climate has challenged our understanding of climate dynamics under extreme greenhouse conditions and questioned our prediction of future greenhouse climate. This thesis investigates several long-standing problems in mid-Cretaceous using state-of-the art coupled ocean-atmosphere GCMs. In summary, this study suggests that boundary conditions including paleogeography, sea level, and atmospheric pCO_2 can lead to remarkable changes in mid-Cretaceous climate system and distribution of marine stable oxygen isotope composition. This chapter summarizes the main findings in light of the questions asked in Chapter I, discusses the major contributions and limitations, and concludes with possible future directions for the mid-Cretaceous study based on this thesis.

6.1. Results summary

Chapter II: This chapter presents the first mid-Cretaceous simulations with fully dynamic interactions of ocean, atmosphere and vegetation. In review of the limitations of previous studies, we re-examine the mid-Cretaceous climate system under high atmospheric pCO_2 using CCSM3 with an optional dynamic vegetation component. Model results demonstrate that inclusion of vegetation and increase in atmospheric pCO_2 both lead to global warming, especially at high latitudes. With 16x pre-industrial levels

atmospheric pCO_2, CCSM3 could sustain the polar vegetation and warmth as indicated by proxies except in the Arctic region. Therefore, other mechanisms in addition to vegetation and high atmospheric pCO_2 are required to support the suggested polar warmth. Furthermore, inclusion of vegetation and increase in atmospheric pCO_2 both weaken the atmospheric Hadley circulation and oceanic horizontal/meridional circulation. Consequently, poleward heat transport via the atmosphere and ocean decreases.

Chapter III: Using the same model and experiments as in Chapter II, this chapter explores how transient climate variability varies with mean climate state. Time series analysis shows that unlike the modern experiment and mid-Cretaceous experiment with pre-industrial level atmospheric pCO_2, mid-Cretaceous experiment with 10x pre-industrial levels atmospheric pCO_2 experiences an abrupt and persistent Arctic warming. This warming is initiated by the natural variability of poleward oceanic heat transport and thus provides a new polar warming mechanism without modification of the existing model physics. The unforced Arctic warming induces an intensification of the oceanic meridional overturning circulation, suggesting that there may be multiple states of overturning and the onset/demise of ocean anoxia events could be induced by natural variability in the ocean-atmosphere system.

Chapter VI: In this chapter, we develop the first coupled ocean-atmosphere GCM (GENMOM) to simulate the mid-Cretaceous marine seawater $\delta^{18}O_{sw}$**.** This model is able to capture the large-scale distribution of modern precipitation and seawater $\delta^{18}O_{sw}$**.** A comparison between the modern simulation and the mid-Cretaceous simulation with 8x pCO_2 reveals that mid-Cretaceous surface seawater $\delta^{18}O_{sw}$ is more depleted by ~1.3‰ at

low-to-mid latitudes and > 2.0‰ at the northern high latitudes than modern. The difference in latitudinal seawater $\delta^{18}O_{sw}$ distribution between the modern and mid-Cretaceous are attributed to equilibrium fractionation during surface evaporation at lowThe unforced Arctic warming induces an intensification of the oceanic meridional overturning circulation, suggesting that there may be multiple states of overturning and the onset/demise of ocean anoxia events could be induced by natural variability in the ocean-atmosphere system. Chapter VI: In this chapter, we develop the first coupled ocean-atmosphere GCM (GENMOM) to simulate the mid-Cretaceous marine seawater $\delta^{18}O_{sw}$. This model is able to capture the large-scale distribution of modern precipitation and seawater $\delta^{18}O_{sw}$. A comparison between the modern simulation and the mid-Cretaceous simulation with 8x pCO_2 reveals that mid-Cretaceous surface seawater $\delta^{18}O_{sw}$ is more depleted by ~1.3‰ at low-to-mid latitudes and > 2.0‰ at the northern high latitudes than modern. The difference in latitudinal seawater $\delta^{18}O_{sw}$ distribution between the modern and mid-Cretaceous are attributed to equilibrium fractionation during surface evaporation at low latitudes, enhanced low-to-high latitude vapor transport, and an increased partitioning of ^{18}O from the surface into the deep ocean at high latitudes in the Cretaceous. Moreover, we also find that regional seawater $\delta^{18}O$ is significantly influenced by the paleobathymetry and the resolution of oceanic gateways, boundary conditions that are not well known for the past. Therefore, oxygen isotope paleothermometry using conventional assumptions of global mean seawater $\delta^{18}O_{sw}$ or global mean corrected by modern latitudinal gradient overestimates the mid-Cretaceous sea-surface temperatures, especially at high latitudes. As a result, the application of simulated seawater $\delta^{18}O_{sw}$ could reduce the model-data mismatch especially at mid-to-

high latitudes.

Chapter V: Based on the findings of Chapter VI, this chapter carries out a suite of sensitivity experiments to quantify the effects of pCO_2, eustatic sea level, regional paleogeography and freshwater forcing on marine seawater and carbonate $\delta^{18}O$. Results show that the distribution of surface seawater $\delta^{18}O_{sw}$ is sensitive to the restriction degree of the proto- North Atlantic. While increasing pCO_2 leads to a relatively uniform surface and subsurface depletion in carbonate $\delta^{18}O_c$. Changes in sea level, regional paleogeography and freshwater forcing have a substantial influence on carbonate $\delta^{18}O_c$ that varies with latitude and depth. And the changes largely signal temperature variations. By comparing model results with reported marine $\delta^{18}O_c$, we find that variations in mid-Cretaceous marine carbonate $\delta^{18}O_c$ likely represent regional oceanographic changes rather than global warming or glaciation.

6.2. Contribution and implication

The new findings in this dissertation not only increase our understanding of the mid-Cretaceous greenhouse climate, but also have important implications for the geological paleoclimate reconstruction and paleoclimate modeling. **First**, by turning on/off dynamic vegetation model and varying atmospheric pCO_2 in the fully coupled CCSM3, this dissertation reveals enhanced atmospheric pCO_2 and vegetation cover are both leads to a global warming and a weakening of Hadley Circulation, oceanic baratropic streamfunction and meridional overturning circulation. The dynamic effects of vegetation discovered here have not been generally recognized before. **Second**, our time series analysis indicates that there could be high-latitude tipping points/thresholds in a

warm climate first. **Third,** our novel model with water isotope tracking capabilities demonstrates that the distribution of seawater $\delta^{18}O_{sw}$ in the distant past could vary significantly from that of modern. Therefore, using modern latitudinal seawater $\delta^{18}O_{sw}$ or global mean value could bias oxygen isotope paleotemperatures by several degrees. The widely accepted notion of "equable climate" with low equator-to-pole thermal gradient may be at least partially due to the inappropriate assumptions of seawater $\delta^{18}O_{sw}$. **Fourth**, the extensive sensitivity experiments we have designed in this study reveal that local/regional oceanography changes could significantly depart from global climate changes. One should keep this in mind when attempting to link the limited geological proxy data to global climate changes. **Fifth**, the two GCMs used in this studies both perform best with the upper limit of the mid-Cretaceous pCO_2 estimates (16x pre-industrial levels), implying that either CO_2 sensitivity in GCMs is much lower than the true value, or most of the previous studies underestimate the mid-Cretaceous atmospheric pCO_2, or the concentrations of some other greenhouse gases (e.g. CH_4) were also high during the mid-Cretaceous.

6.3. Limitation

Generally speaking, in addition to uncertainty inheriting from model parameterization (e.g. cloud), the simulation of pre-Quaternary climate is subject to uncertainties associated with limited knowledge on boundary conditions (e.g., pCO_2, pCH_4, orbital parameters, paleogeography/topography/bathymetry etc.) and initial conditions. For a similar reason, due to our lack of understanding of past ecosystems,

paleo-vegetation modeling relies on a modern understanding of PFTs and their bioclimatic, physiological, and dynamic relationships that may not be entirely appropriate for the mid-Cretaceous. Furthermore, climate models used in this dissertation are too coarse to realistically capture the effects of local/regional forcings in the semi-isolated Arctic Ocean and Tethys Sea. The different spatial resolutions between models and geological proxy also complicate the comparison between model results with proxy data.

6.4. Recommendations for future research

The implication and limitations of this thesis suggest a few possible future directions for the mid-Cretaceous climate research**:**

1. Testing high-latitude climate stability with different models and climate conditions. In this dissertation, we find that there could be high-latitude thresholds in a warm climate for the first time. This high-latitude instability contributes significantly to changes in high latitude climate and global meridional overturning circulation, which has implications for the future. The robustness of this novel discovery needs to be test using different models under modern and past warm conditions.

2. The effects of Earth orbital parameters on climate and ocean circulation. In this dissertation, we hypothesize that variation in orbital configuration may contribute substantially to the oceanic reorganization in the Tethys Sea via freshwater flux. Implementing transient orbital configurations to the fully coupled ocean-atmosphere model with water isotope tracking capability would provide a more comprehensive view of the mid-Cretaceous climate change and water isotope evolution on orbital scale.

3. The effects of more realistic mid-Cretaceous vegetation on climate. In this

dissertation, we find that vegetation could not only change regional temperature and hydrological cycle, but also influence large-scale atmospheric and oceanic circulation. However, the vegetation model used here (DGVM) is based on modern understanding of dominant vegetation species and their bioclimatic, physiological and dynamic relationships. A good example would be the dominance of angiosperms. The modern angiosperm-dominated tropical forests may not have appeared until the Paleocene (Burnham and Johnson, 2004). Yet our simulations show extensive tropical forests resembling the modern distribution, an overestimation that may be linked to the inclusion of PFTs that represent modern angiosperm trees. Consequently, CLM-DVGM may overestimate the impact of low-latitude vegetation on mid-Cretaceous climate, because angiosperms have a much larger impact on hydrology relative to other plants due to their high transpiration capacity (Boyce and Lee, 2010; Boyce et al., 2010). Moreover, without an upper limit for CO_2 physiological effects, we also exclude CO_2 physiological effects as the model fails when with 10x physiological pCO_2. Therefore, a more realistic representation for mid-Cretaceous vegetation is desirable to further assess the vegetation-climate interaction during the warm mid-Cretaceous.

4. Reduce uncertainties and improve precision for paleo-reconstruction. Integrating proxy data and climate model results is probably the most powerful and effective approach to improve understanding of the Earth system processes (in the warm mid-Cretaceous). However, the large inconsistencies and uncertainties in proxy reconstruction of paleoclimate and boundary conditions (e.g., paleogeography, pCO_2) limit the implication of GCM results. More accurate reconstructions will benefit studies of both paleoclimate and climate modeling.

5. The effects of small-scale tectonic events on regional oceanography with high- resolution regional models. Sensitivity tests in this dissertation reveal that the opening/closing of some critical yet small seaways/gateways could contribute significantly to local/regional oceanographic changes. Due to the coarse resolutions of the GCMs used in this dissertation, we have to either neglect or exaggerate these seaways/gateways. Alternatively, high-resolution regional models taking boundary conditions from GCMs are capable to simulate a more realistic oceanic response to those small-scale tectonic changes.

6. The correlation between mid-Cretaceous climate change, biogeochemistry and marine events. The periodic Oceanic Anoxia Events (OAEs) during the Cretaceous, characterized by the black carbon-rich sediments, are among the best targets to explore the interactions among the physical, chemical, biological processes and climate change. Results from coupled ocean-atmosphere GCMs in this thesis offer plausible qualitative links between the climate change and the OAEs. We find that climate becomes warmer and wetter and the ocean becomes more stratified with increasing atmospheric pCO_2 and inclusion of vegetation. This warmer and wetter climate accelerates terrestrial weathering, which presumably enhances oceanic productivity by providing more nutrients into the ocean. A stratified ocean leads to reduced oxygen fugacity in the ocean. The combination of these two processes suggests that the high atmospheric pCO_2 and extensive vegetation cover during Cretaceous promotes oceanic anoxia events. This interpretation, however, is limited due to the absence of direct quantitative evidence in the general circulation models. Developing a biogeochemical module for the general circulation models is thus necessary to quantitatively understand the relationship between

climate change and marine biogeochemical events.

References

Abbot, D. S. and Tziperman, E.: A high-latitude convective cloud feedback and equable climates, Q. J. R. Meteorol. Soc., 134, 165–185, 2008.

Alley, R. B. et al. Abrupt climate change. Science 299, 2005-2010, 2003.

Alo, C. A. and Wang, G.: Potential future changes of the terrestrial ecosystem based on climate projections by eight general circulation models, Geophys. Res. Lett., 113, G01004, doi: 10.1029/2007JG000528, 2008.

Anderson, T. F., and Arthur, M. A., Stable isotopes of oxygen and carbon and their application to sedimentologic and paleoenvironmental problems, in Arthur, M. A., Anderson, T. F., Kaplan, I. R., Veizer, J., and Land, L. S., eds., Stable isotopes in sedimentary geology: Society of Economic Paleontologists and Mineralogists Short Course 10, p. 1.1–1.151, 1983.

Ando, A., Huber, B.T., MacLeod, K.G., Ohta, T., and Khim, B., Black Nose stable isotopic evidence against the mid-Cenomanian glaciations hypothesis: Geology, v. 37, p.451-454., doi: 10.1130/G25580A.1, 2009.

Ando, A., Huber, B.T. and MacLeod, K.G., Depth-habitat reorganization of planktonic foraminifera across the Albian/Cenomanian boundary: Paleobiology, v. 36, p. 357-373, DOI: 10.1666/09027.1, 2010.

Barron, E. J., A warm, equable Cretaceous: the nature of the problem: Earth-Science Reviews, 19, 305-338, 1983.

Barron, E. J. and Washington, W. M.: Warm Cretaceous climates: High atmospheric CO_2 as a plausible mechanism, in Sundquist, E.T., and Broecker, W.S. (Eds.): The carbon cycle and atmospheric CO2: Natural variations, Archean to present, American Geophysical Union Geophysical Monograph, 32, 546–553, 1985.

Barron, E.J., Global Cretaceous Paleogeography-International Geologic Correlation Program Project 191: Palaeogeography, Palaeoclimatology, Palaeoecology, v. 59, p. 207-214, 1987.

Barron, E.J.: Cretaceous plate tectonic reconstructions, Palaeogeography, Palaeoclimatology, Palaeoecology, 59, 3–29, 1987.

Barron, E. J., W. W. Hay, and S. Thompson, The hydrologic cycle: A major variable during Earth history, Palaeogeography, Palaeoclimatology, Palaeoecology, 75, 157-174, 1989.

Barron, E. J., Chill over the Cretaceous, Nature, 370, 415, 1994.

Barron, E. J., Fawcett, P. J., Peterson, W. H., Pollard, D. and Thompson, S. L.: A "simulation" of Mid-Cretaceous climate, Paleoceanography, 10, 953-962, 1995.

Beerling, D. J., Woodward, F. I. and Valdes, P. J.: Global terrestrial productivity in the mid-Cretaceous (100Ma): Model simulations and data, in Barrera, E. and Johnson, C. (Eds): Evolution of the Cretaceous ocean-climate system, Spec. Pap. Geol. Soc. Am., 332, 385-390, 1999.

Bemis, B.E., Spero, H.J., Bijma, J., and Lea, D.W., Reevaluation of the oxygen isotopic composition of planktonic foraminifera: Experimental results and revised paleotemperature equations: Paleoceanography, v. 13, p. 150-160, 1998.

Bengtsson, L., Semenov, V. and Johannessen, O. The early twentieth-century warming in the Arctic-a possible mechanism. J. Clim. 17, 4045-4057, 2004.

Betts, R. A.: Self-beneficial effects of vegetation on climate in an ocean-atmosphere general circulation model, Geophys. Res. Lett., 26, 1457-1460, 1999.

Bice, K. L., E. J. Barron and W. H. Peterson, Continental runoff and early Cenozoic bottom-water sources, Geology, 25, 951-954, 1997.

Bice, K. L. and Norris, R. D.: Possible atmospheric CO_2 extremes of the Middle Cretaceous (late Albian–Turonian), Paleoceanography, 17, 1070, doi:10.1029/2002PA000778, 2002.

Bice, K. L., B. T. Huber and R. D. Norris, Exetreme polar warmth during the Cretaceous greenhouse? Paradox of the late Turonian $\delta^{18}O$ record at Deep Sea Drilling Project Site 511, Paleoceanography, 18, 1031, doi:10.1029/2002PA000848, 2003.

Bice, K. L., Birgel, D., Meyers, P. A., Dahl, K. A., Hinrichs, K. and Norris, R. D.: A multiple proxy and model study of Cretaceous upper ocean temperatures and atmospheric CO_2 concentrations, Paleoceanography, 21, PA2002, doi:10.1029/2005PA001203, 2006.

Bonan, G. and Levis, S.: Evalulating aspects of the Community Land and Atmosphere Models (CLM3 and CAM3) using a dynamic global vegetation model, Journal of Climate, 19, 2290-2301, 2006.

Bonan, G. B., Levis, S., Sitch, S., Vertenstein, M. and Oleson, K.: A dynamic global vegetation model for use with climate models: concepts and description of

simulated vegetation dynamics, Global Change Biology, 9, 1543-1566, 2003.

Bonan, G. B.: Forests an climate change: forcings, feebacks , and the climate benefits of forests, Science, 320, 1444-1449, 2008.

Bornemann, A., Norris, R.D., Friedrich, O., Beckmann, B., Schouten, S., Damste, J.S.S., Vogel, J., Hofmann, P., and Wagner, T., Isotopic evidence for glaciations during the Cretaceous supergreenhouse: Science, v. 319, p. 189-192, doi: 10. 1126 / science. 11 48777, 2008.

Boyce, C. K. and Lee, J. E.: An exceptional role for flowering plant physiology in the expansion of tropical rainforests and biodiversity, Proc. Roy. Soc. Lond., Ser. B, Biol. Sci, 277, 3437-3443, 2010.

Boyce, C. K., Lee, J. E., Field, T. S., Brodribb, T. J., and Zwieniecki, A. Z. : Angiosperms helped put the rain in the rainforests: the impact of plant physiological evolution on tropical biodiversity, Annals of the Missouri Botanical Garden, 94, 527-540, 2010.

Bralower, T. and Thierstein, H. R. Low productivity and slow deep-water circulation in mid-Cretaceous oceans. Geology 12, 614-618, 1984.

Branstetter, M. L.: Development of a parallel river transport algorithm and applications to climate studies, Ph.D. thesis, University of Texas at Austin, 119 pp, 2001.

Briegleb, B.P., et al., Scientific description of the sea ice component in the Community Climate System Model, Version Three. Tech. Rep. NCAR/TN-463+STR, National Center for Atmospheric Research, Boulder, CO, 78 pp., 2004.

Brovkin, V.: Climate-vegetation interaction, J. Phys. IV FRANCE, 12, 10-57, 2002.

Brovkin, V., Raddatz, T., Reich, C. H., Claussen, M. and Gayler, V.: Global biogeophysical interactions between forest and climate, Geophys. Res. Lett., 36, L07405, doi:10.1029/2009GL037543, 2009.

Burnham, R. J. and Johnson, K. R.: South American palaeobotany and the origins of neotropical rainforests, Phil. Trans. R. Soc. Lond. B, 359, 1595-1610, 2004.

Cantrill, D., The occurrence of the fern Hausmannia Dunker in the Cretaceous of Alexander Island, Antarctica: An Australasian Journal of Palaeontology, v. 19, p. 243-254.

Cerling, T. E., Wang, Y. and Quade, J.: Expansion of C4 ecosystems as an indicator of global ecological change in late Miocene, Nature 361, 344-345, 1993.

Clarke, L.J., and Jenkyns, H.C., New oxygen isotope evidence for long-term Cretaceous

climatic change in the Southern Hemisphere: Geology, v. 27, p. 699–702, 1999.

Clarke, L.J., Stable-isotopic evidence for mid- to Late Cretaceous oceanographic and climatic change [Ph.D. thesis]: Oxford, UK, University of Oxford, 287 p, 2001.

Collins, W. D., Bitz, C. M., Blackmon, M. L., Bonan, G. B., Bretherton, C. S., Carton, J. A., Chang, P., Doney, S. C., Hack, J. J., Henderson, T. B., Kiehl, J. T., Large, W. G., McKenna, D. S., Santer, B. D. and Smith, R. D.: The Community Climate System Model Version 3 (CCSM3), J. Clim., 19, 2122-2143, 2006.

Covey, C. and Barron, E.: The role of ocean heat transport in climatic change. Earth-Science Reviews, 21, 429-445, 1988.

Cramer, W., Bondeau, A., Woodward, F. I., Prentice, I. C., Betts, R. A., Brovkin, V., Cox, P., Fisher, V., Foley, J. A., Friend, A. D., Kucharik, C., Lomas, M., Ramankutty, N., Sitch, S., Smith, B., White, A. and Young-Molling, C.: Global response of terrestrial ecosystem structure and function to CO2 and climate change: results from six dynamic global vegetation models, Global Change Biology, 7, 357-373, 2001.

Crowley, T.J., and Berner, R.A., CO2 and climate change: Science, v. 292, p. 870-872, 2001.

Davies, A., Kemp, A. E. and Pike, J. Late Cretaceous seasonal ocean variability from the Arctic. Nature 460, 254-258, 2009.

DeConto, R. M., Brady, E. C., Bergengren, J., Hay, H. H.: Late Cretaceous Climate, Vegetation, and Ocean Interactions, in Huber, B., MacLeod, K. G and Wing, S. L (Eds.): Warm Climates in Earth History, Cambridge University Press, 275-297, 2000.

DeConto, R.M., and Pollard, D., Rapid Cenozoic glaciations of Antarctica induced by declining atmospheric CO_2: Nature, v. 421, p. 245-249, 2003.

Dickinson, R.E., et al., The Community Land Model and its climate statistics as a component of the Community Climate System Model. J. Clim. 19, 2302-2324, 2006.

Dino, R., Pocknall, D. T. and Dettmann, M. E.: Morphology and ultrastructure of elater-bearing pollen from the Albian to Cenomanian of Brazil and Ecuador: implications for botanical affinity, Review of palaeobotany and palynology 105, 201-235, 1999.

Donnadieu, Y., Pierrehumbert, R., Jacob, R. and Fluteau, F.: Modelling the primary control of paleogeography on Cretaceous climate, Earth and Planetary Science Letters, 248, 426-437, 2006.

Donnadieu, Y., Godderis, Y. and Bouttes, N.: Exploring the climatic impact of the continental vegetation on the Mesozoic atmospheric CO_2 and climate history, Clim. Past, 5, 85-96, 2009.

Erez, J. and B. Luz, Experimental paleotemperature equation for planktonic foraminifera, Geochimica et Cosmochimica Acta, 47, 1025–1031, 1983.

Falcon-Lang, H. J., Cantrill, D. J. and Nichols, G. J.: Biodiversity and terrestrial ecology of a mid-Cretaceous, high-latitude floodplain, Alexander Island, Antarctica, Journal of the Geological Society, 158, 709-724, 2001.

Farrel, G. F.: Equable climate dynamics, J. Atmos. Sci., 47, 2986-2995, 1990.

Forster, A., Schouten, S., Baas, M., and Damste, J.S.S., Mid-Cretaceous (Albian-Santonian) sea surface temperature record of the tropical Atlantic Ocean: Geology, v. 35, p. 919-922, doi: 10.1130/G23874A.1, 2007.

Francis, J.E., and Poole, I., Cretaceous and early Tertiary climates of Antarctica: evidence from fossil wood: Palaeogeography, Palaeoclimatology, Palaeoecology, v. 182, p. 47-64, 2008.

Frew, R. D., K. J. Heywood and P. F. Dennis, Oxygen isotope study of water masses in the Princess Elizabeth Trough, Antarctica, Marine Chemistry, 49, 141-153, 1995.

Friedrich, O., Erbacher, J., Moriya, K., Wilson, P.A., and Kuhnert, H., Warm saline intermediate waters in the Cretaceous tropical Atlantic Ocean: Nature Geoscience, v. 1, p. 453-457, doi: 10.1038/ngeo217, 2008.

Galeotti, S., Rusciadelli, G., Sprovieri, M., Lanci, L., Gaudio, A., and Pekar, S., Sea-level control on facies architecture in the Cenomanian-Coniacian Apulian margin (Western Tethys): A record of glacio-eustatic fluctuations during the Cretaceous greenhouse?: Palaeogeography, Palaeoclimatology, Palaeoecology, v. 276, p. 196-205, 2009.

Ganachaud, A. and Wunsch, C. Improved estimates of global ocean circulation, heat transport and mixing from hydrographic data. Nature 408, 453-457, 2000.

Ganopolski, A., Kubatzki, C., Claussen, M., Brovkin, V. and Petoukhov, V.: The influence of vegetation-atmosphere-ocean interaction on climate during the mid-Holocene. Science, 280, 1916-1919, 1998.

Gough, D.O., Solar interior structure and luminosity variations: Sol. Phys., v. 74, p. 21-34, 1981.

Haq, B., Hardenbol, J., Vail, P., Chronology of fluctuating sea levels since the Triassic:

Science, v. 23, p. 1156–1167, 1987.

Haworth, M., Hesselbo, S. P., McElwain, J. C., Robinson, S. A. & Brunt, J. W. Mid-Cretaceous pCO2 based on stomata of the extinct conifer Pseudofrenelopsis (Cheirolepidiaceae). Geology 33, 749-752, 2005.

Herman, A. B. and Spicer, R. A.: Palaeobotanical evidence for a warm Cretaceous Arctic Ocean, Nature, 380, 330-333, 1996.

Horton, D.E., and Poulsen, C.J., Paradox of late Paleozoic glacioeustasy: Geology, v. 37, p. 715-718, doi:10.1130/G30016A.1, 2009.

Huber, B.T., Hodell, D.A., and Hamilton, C.P., Middle-Late Cretaceous climate of the southern high latitudes: Stable isotopic evidence for minimal equator-to-pole thermal gradients: Geological Society of America Bulletin, v. 107, p. 1164–1191, 1995.

Huber, B. T., Tropical paradise at the Cretaceous poles, Science, 282, 2199-2200, 1998.

Huber, B.T., Norris, R.D., and MacLeod, K.G., 2002, Deep-sea paleotemperature record of extreme warmth during the Cretaceous: Geology, v. 30, p. 123-126, 2002.

Iturralde-Vinent, M. A., A brief account of the evolution of the Caribbean Seaway: Jurassic to present, in Prothero, D.R., Ivany, L.C., Nesbitt, E.A., eds., From Greenhouse to Icehouse. The marine Eocene-Oligocene transition. Columbia University Press: New York. p.386–396, 2003.

Jacobs, B. F., Kingston, J. D. and Jacobs, L. L.: The origin of grass-dominanted ecosystems, Ann. Missouri Bot. GARD., 86, 590-643, 1999.

Jenkyns, H.C., Gale, A.S., and Corfield, R.M., Carbon- and oxygen-isotope stratigraphy of the English Chalk and the Italian Scaglia and its palaeoclimatic significance: Geological Magazine, v. 131, p. 1–34, 1994.

Jenkyns, H. C., Forster, A., Schouten, S. and Damsté, J. S. S.: High temperatures in the Late Cretaceous Arctic Ocean, Nature, 432, 888-892, 2004.

Johannessen, O. et al. Arctic climate change-observed and modeled temperature and sea-ice variability. Tellus 56A, 328-341, 2004.

Joussaume, S., and Jouzel, J. (1993), Paleoclimatic tracers: An investigation using an atmospheric general circulation model under ice age conditions, 2, water isotopes: *Journal of Geophysical Research*, *98,* 2807–2830, 1993.

Jouzel, J., D. Koster, R. J. Suozzo, and G.L. Russell, Stable isotope behavior during the last glacial maximum. A general circulation model analysis: Journal of Geophysical Research, *99,* 25,791–25,801, doi: 10.1029/94JD01819, 1994.

Kiehl, J. T., J. J. Hack, G. B. Bonan, B. A. Boville, D. L. Williamson and P. J. Rasch, The National Center for Atmospheric Research Community Climate Model: CCM3, J. Climate, 11, 1131-1149, 1998.

Kolodny, Y., B. Luz and O. Navon, Oxygen isotope variations in phosphate of biogenic apatites. I. Fish bone apatite -- rechecking the rules of the game, Earth Planet. Sci. Lett., 64, 398-404, 1983.

Korty, R. L., Emanuel, K. A. and Scott, A. J.: Tropical cyclone-induced upper-ocean mixing and climate: application to equable climate, J. Clim., 21, 638-654, 2008.

Kump, L. R. and Pollard, D.: Amplification of Cretaceous warmth by biological cloud feedbacks, Science, 320, 195, 2008.

Larson, R.L., Geological consequences of superplumes: Geology, v. 19, p. 963–966, 1991.

LeGrande, A. N. and G. A. Schmidt, Global gridded data set of the oxygen isotopic composition in seawater, Geophysical Research Letters, 33, L12604, doi: 10.1029/2006GL026011, 2006.

Levis, S.G., Bonan, G. B., Vertenstein, M. and Oleson, K. W.: The Community Land Model's Dynamic Global Vegetation Model (CLM-DGVM): Technical Description and User's Guide, NCAR Tech. Note TN-459+IA, National Center for Atmospheric Research, Boulder, CO, 50 pp, 2004.

Little, S. A., Kembel, S. W. and Wilf, P.: Paleotemperature proxies from leaf fossils reinterpreted in light of evolutionary history: Plos One, 5, e15161 . doi : 10. 1371 /journal.pone.0015161, 2010.

Lohmann, G., Butzin, M., Micheels, A., Bickert, T. and Mosbrugger, V.: Effect of vegetation on the Late Miocene ocean circulation, Clim. Past Discuss., 2, 605-631, 2006.

MacLeod, K.G., Huber, B.T., and Ducharme, M.L., Paleontological and geochemical constraints on changes in the deep ocean during the Cretaceous greenhouse interval, in Huber, B. T., MacLeod, K. G., and Wing, S. L., eds., Warm Climates in Earth History: Cambridge, Cambridge University Press, p. 241-274, 2000.

MacLeod, K.G., Londoño, C.I., Martin, E.E., Berrocoso, Á.J., and Basak, C., Changes in North Atlantic circulation at the end of the Cretaceous greenhouse interval: Nature Geoscience, v. 4, p. 780-782, DOI: 10.1038/NGEO1284, 2011.

Marotzke, J., Influence of convective adjustment on the stability of the thermohaline circulation, Journal of Physical Oceanography, 21, 903-907, 1991.

Mathieu, R.D., Pollard, D., Cole, J.E., White, J.W.C.,Webb, R.S., and Thompson, S.L., Simulation of stable water isotope variations by the GENESIS GCM for modern conditions: Journal of Geophysical Research, v. 107, p. 2-1 - 2-18, 2002.

Miller, K.G., Kominz, M.A., Browning, J.V., Wright, J.D., Mountain, G.S., Katz, M.E., Sugarman, P.J., Cramer, B.S., Christie-Blick, N., and Pekar, S.F., The Phanerozoic record of global sea-level change: Science, v. 310, p. 1293-1298, doi: 10.1126/science.1116412, 2005.

Miller, K.G., Broken greenhouse windows: News & Views: Nature Geoscience, v. 2, p. 465-466, 2009.

Moriya, K., Wilson, P.A., Friedrich, O., Erbacher, J., and Kawahata, H., Testing for ice sheets during the mid-Cretaceous greenhouse using glassy foraminiferal calcite from the mid-Cenomanian tropics on Demerara Rise: Geology, v. 35, p. 615-618, doi: 10.1130/G23589A.1, 2007.

Nathorst, A. G. Ueber die Reste eines Brotfruchtbaums ARTOCARPUS DICKSONI N. SP., aus den cenomanen Kreideablagerungen Gro¨nlands. Kongl. Svenska Vetenskaps-Akad. Hand 24, 2–9, 1890.

Nathorst, A. G., On the value of fossil floras of the Arctic regions as evidence of geological climate, Geological Magazine, 8, 217-225, 1911.

Norris, R. D., K. L. Bice, E. A. Magno and P. A. Wilson, Jiggling the tropical thermostat in the Cretaceous hothouse, Geology, 30, 299-302, 2002.

Ogg, J.G., and Bardot, L., Aptian through Eocene magnetostratigraphic correlation of the Blake Nose Transect (Leg 171B), Florida continental margin, in Kroon, D., et al., Proceedings of the Ocean Drilling Program, Scientific results, Volume 171B: College Station, Texas, Ocean Drilling Program, doi: 10.2973 / odp .proc. sr.171B. 104.2001, 2001.

Otto-Bliesner, B. L. and Upchurch Jr, G. R.: Vegetation-induced warming of high-latitude regions during the Late Cretaceous period, Nature, 385, 804-807, 1997.

Otto-Bliesner, B. L., Brady, E. C. and Shields, C.: Late Cretaceous ocean: Coupled simulations with the National Center for Atmospheric Research Climate System Model, J. Geophys. Res., 107, doi:10.1029/2001JD000821, 2002.

Overpeck, J. T. and Cole, J. E. Abrupt change in Earth's climate system. Annu. Rev. Environ. Resour. 31, 1-31, 2006.

Overland, J. E., Wang, M. and Salo, S. The recent Arctic warm period. Tellus 60A, 589-597, 2008.

Pacanowski, R.C., MOM2 documentation, user's guide and reference manual, Version 1.0: GFDL Ocean Group Technical Report No.3, GFDL/NOAA, Princeton University, Princeton, 1995.

Parrish, J. T. and R. A. Spicer, Late Cretaceous terrestrial vegetation: A near-polar temperature curve, Geology, 16, 22-25, 1988.

Peng, C. H.: From static biogeographical model to dynamic global vegetation model: a global perspective on modeling vegetation dynamics, Ecological Modelling, 135, 33-54, 2000.

Peppe, D. J., Royer, D. L., Wilf, P., and Kowalski, E. A.: Quantification of large uncertainties in fossil leaf paleoaltimetry, Tectonics, 29, doi:10.1029/2009TC002549, 2010

Peppe, D. J., Royer, D. L., et al., Sensitivity of leaf size and shape to climate: global patterns and paleoclimatic applications, New Phytologist, 190, 724-739, 2011.

Petrizzo, M. R., B. T. Huber, P. A. Wilson, and K. G. MacLeod, Late Albian paleoceanography of the western subtropical North Atlantic, Paleoceanography, 23, PA1213, doi:10.1029/2007PA001517, 2008.

Polyakov, I. V. & Johnson, M. A. Arctic decadal and interdecadal variability. Geophys. Res. Lett. 27, 4097-4100, 2000.

Poulsen, C. J., E. J. Barron, C. Johnson, and P. Fawcett, Links between major climatic factors and regional oceanic circulation in the mid-Cretaceous, in Evolution of the Cretaceous ocean-climate system: Geological Society of America Special Paper 332, edited by Barrera, E., and C.C. Johnson, pp. 73–90, GSA, Boulder, Colorado, 1999a.

Poulsen, C. J., E. J. Barron, W. H. Peterson, and P. A. Wilson, A reinterpretation of mid-Cretaceous shallow marine temperatures through model-data comparison, Paleoceanography, 14, 679-697, 1999b.

Poulsen, C. J., E. J. Barron, M. A. Arthur, and W. H. Peterson, Response of the mid-Cretaceous ocean circulation to tectonic and CO2 forcing, Paleoceanography, 16, 576-592, 2001.

Poulsen, C.J., Gendaszek, A.S., and Jacob, R.L., Did the rifting of the Atlantic Ocean cause the Cretaceous thermal maximum?: Geology, v. 31, p. 115-118, 2003.

Poulsen, C. J.: A balmy Arctic, Nature, 432, 814-815, 2004.

Poulsen, C. J., D. Pollard, I. S. Montanez, and D. Rowley, Late Paleozoic tropical climate

response to Gondwanan deglaciation, Geology, 35, 771-774, 2007a.

Poulsen, C. J., Pollard, D. and White, T. S.: General circulation model simulation of the $\delta^{18}O$ content of continental precipitation in the middle Cretaceous: A model-proxy comparison, Geology, 35, 199-202, 2007.

Poulsen, C.J., Ehlers. T., and Insel, N., Onset of convective rainfall during gradual late Miocene rise of the central Andes: Sciences, v. 328, p. 490-493, doi:10.1126/science.1185078, 2010.

Price, G. D., Valdes, P. J. and Sellwood, B. W.: Quantitative palaeoclimate GCM validation: Late Jurassic and mid-Cretaceous case studies, Journal of the Geological Society, 154, 769-772, 1997.

Price, G.D., Sellwood, B.W., Corfield, R.M., Clarke, L., and Cartlidge, J.E., Isotopic evidence for palaeotemperatures and depth stratification of Middle Cretaceous planktonic foraminifera from the Pacific Ocean: Geol.Mag, v. 135, p.183-191, 1998.

Price, G. D., The evidence and implications of polar ice during the Mesozoic, Earth-Science Reviews, 48, 183-210, 1999.

Pucéat, E., C. Lécuyer, Y. Donnadieu, P. Naveau, H. Cappetta, G. Ramstein, B. T. Huber and J. Kriwet, Fish tooth $\delta^{18}O$ revising Late Cretaceous meridional upper ocean water temperature gradients, Geology, 35, 107-110, 2007.

Rahmstorf, S., A fast and complete convection scheme for ocean models, Ocean Model, 101, 9–11, 1993.

Redi, M. H. (1982), Oceanic isopycnal mixing by coordinate rotation, Journal of Physical Oceanography, 12, 1154-1158, 1982.

Retallack, G. A 300-million-year record of atmospheric carbon dioxide from fossil plant cuticles. Nature 411, 287-290, 2001.

Roche, D. M., Y. Donnadieu, E. Pucéat and D. Paillard, Effect of changes in $\delta^{18}O$ content of the surface ocean on estimated sea surface temperature in past warm climate. Paleoceanography, 21, PA2023, doi:10.1029/2005PA001220, 2006.

Rozanski, K., L. Araguds-Araguds and R. Gonfiantini, Isotopic patterns in modem global precipitation, in Climate Change in Continental Isotopic Records - Geophysical Monograph 78, edited by P.K. Swart, K.C. Lohman, J. McKenzie and S. Savin, pp. 1-36, AGU, Washington, D.C, 1993.

Schlesinger, W. H.: Biogeochemistry: An analysis of global change 2nd end, Academic Press, San Diego, 1997.

Schmidt, G. A., G. R. Bigg and E. J. Rohling, Global Seawater Oxygen-18 Database, http://data.giss.nasa.gov/o18data/, 1999.

Schmidt, G. A., A. N. LeGrande and G. Hoffmann, Water isotope expressions of intrinsic and forced variability in a coupled ocean-atmosphere model, J. Geophys. Res., 112, D10103, doi: 10.1029/2006JD007781, 2007.

Schouten, S. et al. Extremely high sea-surface temperatures at low latitudes during the middle Cretaceous as revealed by archaeal membrane lipids. Geology 31, 10699-1072, 2003.

Schouten, S., Hopmans, E.C., Forster, A., Breugel, Y.V., Kuypers, M.M.M., and Damste, J.S.S., Extremely high sea-surface temperatures at low latitudes during the middle Cretaceous as revealed by archaeal membrane lipids, Geology, v. 31, p. 1069-1072, 2003.

Scotese, C.R.: Times of global plate tectonic reorganization and their causes [abs]: Earth system processes, Programmes with Abstracts: London, Geological Society of London and Geological Society of America, p. 102, 2001.

Sellwood, B.W., Price, G.D. and Valdes, P.J.: Cooler estimates of Cretaceous temperatures: Nature, v. 370, p. 453-455.

Shackleton, N., Attainment of isotopic equilibrium between ocean water and the benthonic foraminifera genus Uvigerina: Isotopic changes in the ocean during the last glacial, in Les méthodes quantitatives d'étude des variation du climat au cours du pléistocène, edited by J. Labeyrie, pp. 203-209, CNRS, Paris, 1974.

Shackleton, N.J., and Kennett, J., Paleotemperature history of the Cenozoic and the initiation of Antarctic glaciation: Oxygen and carbon isotope analyses in DSDP Sites 277, 279 and 281, Initial Rep. Deep Sea Drill. Proj., v. 29, p. 743–755, 1975.

Sloan, L. C. and Pollard, D.: Polar Stratospheric clouds: A high latitude warming mechanism in an ancient greenhouse world, Geophys. Res. Lett., 25, 3517–3520, 1998.

Smith, A.G., Smith, D.G., and Funnell, B.M., Atlas of Mesozoic and Cenozoic coastlines: Cambridge, Cambridge University Press, p. 99, 1994.

Smith, R.D., P.R. Gent, Reference manual for the Parallel Ocean Program (POP), ocean component of the Community Climate System Model (CCSM2.0 and 3.0). Tech. Rep. LA-UR-02-2484, Los Alamos National Laboratory, 2002.

Spicer, R. A. and J. T. Parrish, Paleobotanical evidence for cool north polar climates in middle Cretaceous (Albian-Cenomanian) time, Geology, 14, 703-706, 1986.

Spicer, R. A. and Chapman, J. L.: Climate change and the evolution of high-latitude terrestrial vegetation and floras. TREE, 5, 279-284, 1990.

Spicer, R.A., and Corfield, R.M., A review of terrestrial and marine climates in Cretaceous with implication for modeling the 'Greenhouse Earth': Geological Magazine, v. 129, p. 169-180, 1992.

Spicer, R. A., Rees, P. M. and Chapman, J. L.: Cretaceous phytogeography and climate signals, Phil. Trans. R. Soc. Lond. B, 341, 277-286, 1993.

Spicer, R. A., Ahlberg, A., Herman, A. B., Hofmann, C., Raikevich, M., Valdes, P. J. and Markwich, P., J.: The Late Cretaceous continental interior of Siberia: a challenge for climate models, Earth and Planetary Science Letters, 267, 228-235, 2008.

Spicer, R. A., Ahlberg, A., Herman, A. B., Kelley, S. P., Raikevich, M. I. and Rees, P. M.: Palaeoenvironment and ecology of the middle Cretaceous Grebenka flora of northeastern Asia, Palaeogeography, Palaeoclimatology, Palaeoecology, 184, 65-105, 2002.

Stoll, H.M., and Schrag, D.P., High-resolution stable isotope records from the Upper Cretaceous rocks of Italy and Spain: Glacial episodes in a greenhouse planet?: GSA Bulletin, v. 112, p. 308-319, 2000.

Suganuma, Y., and Ogg, J.G., Campanian through Eocene Magnetostratigraphy of Sites 1257-1261, ODP Leg 207, Demerara Rise (Western equatorial Atlantic): Proc. Ocean Drill. Progr. Sci. Results 207, doi:10.2973/odp.proc.sr.207.102.2006, 2005.

Tarduno, J. A., D. B. Brinkman, P. R. Renne, R. D. Cottrell, H. Scher and P. Castillo, Evidence for extreme climatic warmth from late Cretaceous Arctic vertebrates, Science, 282, 2241-2244, 1998.

Thiede, J. and Vallier, T.L. et al., Site 463, western Mid-Pacific Mountains, J. Thiede, T.L. Vallier, Editors Initial Reports of the Deep Sea Drilling Project, v. 62, U.S. Government Printing Office, Washington, D.C, 1981.

Thomas, D. J., Zachos, J. C., Bralower, T. J., Thomas, E. & Bohaty, S. Warming the fuel for the fire: Evidence for the thermal dissociation of methane hydrate during the Paleocene-Eocene thermal maximum. Geology 30, 1067-1070, 2002.

Thompson, S.L., and Pollard, D., Greenland and Antarctic mass balances for present and doubled CO2 from the GENESIS version-2 global climate model: J. Climate, v. 10, p. 871-900, 1997.

Upchurch Jr, G. R., Otto-Bliesner, B. L. and Scotese, C.: Vegetation-atmosphere interactions and their role in global warming during the latest Cretaceous, Phil. Trans. R. Soc. Lond., 353, 97-112, 1998.

Viogt, S., Wilmsen, M., Mortimore, R.N., and Voigt, T., Cenomanian palaeotemperatures derived from the oxygen isotopic composition of brachiopods and belemnites: evaluation of Cretaceous palaeotemperature proxies: Int. J. Earth Sci, v. 92, p. 285-299, 2003.

Voigt, S., Gale, A.S., and Flogel, S., Midlatitude shelf seas in the Cenomanian-Turonian greenhouse world: Temperature evolution and North Atlantic circulation: Paleoceanography, v. 19, PA4020, doi: 10.1029/2004PA001015, 2004.

Wilson, P.A., Norris, R.D., and Cooper, M.J., Testing the Cretaceous greenhouse hypothesis using ‘‘glassy’’ foraminiferal calcite from the core of the Turonian tropics on Demerara Rise: Geology, v. 30, p. 607–610, 2002.

Wolf, J.A., and Upchurch, G.R., North American nonmarine climates and vegetation during the late Cretaceous. Palaeogeography, Palaeoclimatology, Palaeoecology, v. 61, p. 33-77.

Woo, K., Anderson, T.F., Railsback, L.B., and Sandberg, P.A., Oxygen isotope evidence for high-salinity surface seawater in the mid-Cretaceous gulf of Mexico: implications for warm, saline deepwater formation: Paleoceanography, v. 7, p. 673-685.

Zachos, J. C., L. D. Stott and K. C. Lohmann, Evolution of early Cenozoic marine temperatures, Paleoceanography, 9, 353-387, 1994.

Zhou, J., Poulsen, C.J., Pollard, D., and White, T.S., Simulation of modern and middle Cretaceous marine $\delta^{18}O$ with an ocean-atmosphere general circulation model: Paleoceanography, v. 23, PA3223, doi: 10.1029/2008PA001596, 2008. (Chapter IV)

Zhou, J., and Poulsen, C. J., No climate extremes in mid-Cretaceous: Geology (in review, 2011) (Chapter V)

Zhou, J., Poulsen, C. J., Rosenbloom, N., Shields, C. and Briegleb, B.: vegetation-climate interactions in the warm mid-Cretaceous, Climate of the Past (in review, 2011) (Chapter II)

Ziegler, A. M., Eshel, G., Rees, P. M., Rothfus, T. A., Rowley, D. B. and Sunderlin, D.: Tracing the tropics across land and sea: Permian to present, Lethaia, 36, 227-254, 2003.